

Estimation of the sensitivity of *Picea abies* and *Fagus sylvatica* to the effects of abiotic stresses

Laboratory of Tandetron

Pavel Coufalík

Proposal ID

267

Report regarding proposal “Estimation of the sensitivity of *Picea abies* and *Fagus sylvatica* to the effects of abiotic stresses”

P. Coufalík, Institute of Analytical Chemistry of the CAS, Brno, Czech Republic

K. Večeřová, Global Change Research Institute of the CAS, Brno, Czech Republic

V. Havránek, Nuclear Physics Institute of the CAS, Řež, Czech Republic

The trees of *Picea abies* and *Fagus sylvatica* were exposed to CdO nanoparticles (NPs) generated in thermal reactor [1]. The experiment was performed as one and two week's exposure in chambers at two concentration levels of NPs. The number of NPs at the size between 7 and 60 nm was approximately 2×10^5 particles/cm³, and 4.4×10^6 particles/cm³ at the maximum concentration. The eight cuts of *Picea abies* needles (the thickness of 10 and 20 µm, cross sections and longitudinal cuts), and four cuts of *Fagus sylvatica* leaves (10 and 20 µm, cross and surface sections) were prepared on the cryotome.

The samples were subjected to the PIXE (stoma on the Fig. 1.) and STIM during four days (31.5.–1.6. and 12.–13.10.) from the allocated beamdays. The resolution was approximately 1 µm at E = 2.9 MeV. The limit of detection of cadmium was 2 µg/g. The presence of cadmium on the surface of samples was confirmed by scattered beam, however, no cadmium was detected inside the stomata.

The total contents of cadmium in samples at the highest NPs concentrations were 2.3 and 2.1 µg/g for *Picea abies* and *Fagus sylvatica*, respectively. The phytotoxicity of CdO NPs has already been observed at lower concentration levels (e.g. a decrease of photosynthetic pigments). A serious damage of plants occurred after the first week of the experiment at high concentrations of NPs. Therefore, tested concentrations are critical to the carrying out of the experiment, and cannot be further increased. Thus, the use of PIXE for the imaging of NPs in leaf interiors appears to be problematic due to an insufficient limit of quantification of the method.

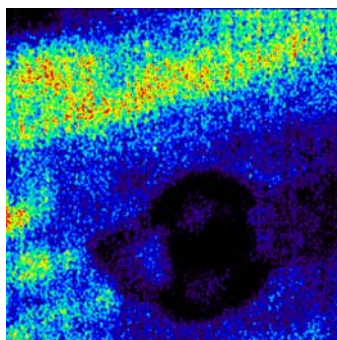


Fig. 1. Stoma of *Picea abies* needle imaged by the absence of calcium (100 x 100 µm)

Reference

1. L. Bláhová, J. Kohoutek, J. Lebedová, L. Bláha, Z. Večeřa, M. Buchtová, I. Míšek, K. Hilscherová, Anal. Bioanal. Chem. 406 (2014) 5867.

Calibration of dosimeters and particle trackers for atmosphere and space radiation research

Laboratory of Cyclotron and Fast Neutron Generators

Carlos Granja

Proposal ID

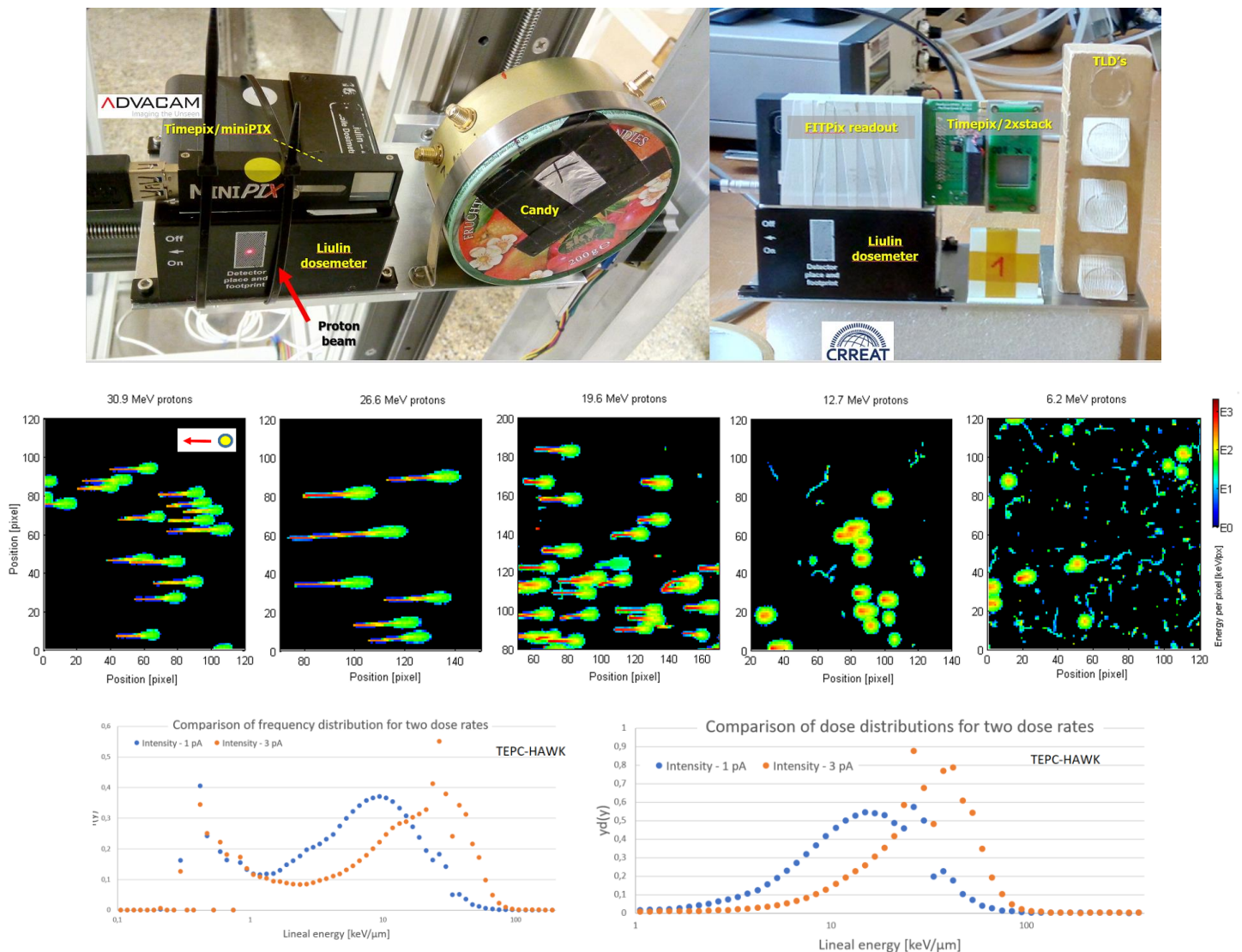
331

Report for experimental proposal “Calibration of dosimeters and particle trackers for atmosphere and space radiation research”

C. Granja, M. Sommer, M. Kakona, V. Stepan, I. Ambrozova, et al., ODZ-UJF/CRREAT*

V. Zach, T. Matlocha, J. Stursa, et al., OU-UJF/CANAM

Summary: Measurements were carried out using proton beams from the UJF-CANAM Cyclotron on various types of radiation detectors selected for studies of radiation phenomena in the atmosphere in frame of the running OP3V project CRREAT. Performed tasks consisted of testing and calibration of detection response as well as intercomparison of different detector technologies (see Fig. top row) including passive devices such as TLDs and track detectors, and active devices such as single diode devices (LIULIN dosimeter, single pad diode CANDY) as well as position-sensitive imaging devices semiconductor pixel detectors. Timepix’ resolving power and track visualization of single particles to a given radiation component (protons) of varying energy is shown (see Fig. middle row). Work included measurements on customized instrumentation for air-crew and space radiation dosimetry such as TEPC (Tissue Equivalent Proportional Counters – see Fig. bottom row). Data is presently under evaluation. Results will be subject of presentation/contribution at 1-2 conferences and 1-2 scientific journal articles.



(*) Research performed in frame of the CRREAT project (Research Centre of Cosmic Rays and Radiation Events in the Atmosphere) supported by European Regional Development Fund-Project CZ.02.1.01/0.0/0.0/15_003/0000481.

Identification of microscopic uranium particles using fission tracks in solid detectors

Neutron Physics Laboratory - Nuclear analytical methods with neutrons

Jan Lorincik

Proposal ID

332

Report regarding proposal “ Identification of microscopic uranium particles using fission tracks in solid detectors”

J. Lorinčík, K. Sihelská, K. Řezanková, F. Sus, Vl. Strunga, J. Kučera

The goals of this project were (A) the study of the number of fission tracks as a function of enrichment and size of U-particles, (B) the optimization of the fission track (FT) procedure for higher reproducibility, robustness, and accuracy.

A quantitative relation between the U-particle enrichment, size, and the number of FTs was used in the following form [1]: $N_T = N_{235} \cdot \sigma_f \cdot \varepsilon \cdot t \cdot \phi_{therm} \dots (1)$, where N_T denotes the number of fission tracks; N_{235} , the number of ^{235}U atoms in a particle; σ_f , the fission cross section for ^{235}U [586 b]; ε , the registration efficiency (0,4); t , the irradiation time [120 s]; ϕ_{therm} , the flux of thermal neutrons [$3,2 \times 10^{13} \text{ cm}^{-2}\text{s}^{-1}$]. Then, N_{235} can be obtained from $N_{235} = 3 \cdot (\rho_{U3O8} \cdot V_p) / M_{U3O8} \cdot N_A \cdot A_{235} / 100 \dots (2)$, where ρ_{U3O8} is U_3O_8 particle density [8,3 g/cm³], V_p volume of the particle [cm³], M_{U3O8} the molar mass of U_3O_8 [842,1 g/mol], N_A the Avogadro's constant, A_{235} the enrichment [%]. Constant 3 in eq. (2) corresponds to the number of U atoms in U_3O_8 molecule. Since SEM images can provide only areas of 2D projections (characterized by equivalent circle diameter – d_{ECD}) of 3D shapes of particles, the geometry models, e.g. sphere, cylinder, cube must be used for V_p estimation.

For experimental work, standard reference materials of U_3O_8 were used: CRM 129-A (NU), CRM 010 (1% ^{235}U enriched), CRM 030-A (3% ^{235}U enriched). Then FT sample assemblies (see more detail in reports of project CANAM:ID241) were prepared and irradiated in the reactor LVR-15 with irradiation parameters specified above. After etching of the Lexan detectors, optical images were made (see Fig. 1 a-c) and the FTs manually counted. The comparison of theoretical estimates and experimental data (lines vs. data points) is in Fig. 1 d.

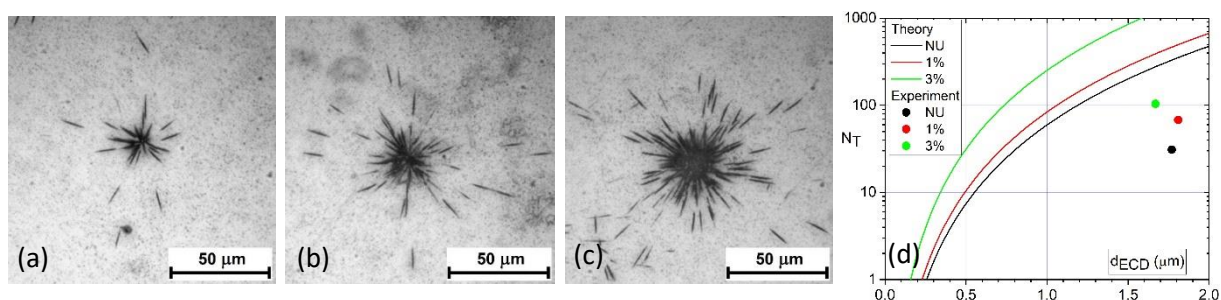


Figure 1. Optical images of FTs corresponding to U_3O_8 particles of NU (a), 1 %U (b), and 3%U (c) [2]. Number of registered FTs in the images (a)-(c) for NU, 1%U, 3%U is 31, 68, 104, resp. (d) Comparison of experimental values (circle symbols) and theoretical estimates (full lines) based on equations (1) and (2) for spherical geometry model ($V_p = \pi/6 \cdot d_{ECD}^3$).

In parallel to the above study, large effort has been spent on improvement of the FT procedure. This goal has been achieved by (i) reconfiguration of the fiducial marks for better particle position precision, (ii) addition of sticky collodion for better particle adhesion, (iii) redesigning of the FT sample assembly for simpler and more reliable manipulation, (iv) employing new optical microscope with motorized stage for automated creation of compound photos of large areas of the Lexan detector, and (v) implementing efficient coordinate transformation algorithm for transfer of particle coordinates between instruments.

In summary, the dependence of the number of FTs on the particle enrichment and size has been investigated both theoretically and experimentally. There is a discrepancy between the theoretically predicted numbers of FTs and the counts of FTs obtained from the experiment. A combined effect of overestimated values of neutron fluences, material density, and FT registration efficiency could have been responsible for that. More experiments are needed to support that explanation and to provide more accurate data for theoretical predictions.

The main outcome of this project is substantial improvement of the FT procedure, which achieved the readiness level that allowed for the proficiency testing for nuclear safeguards.

[1] O. Stetzer, et al., Nucl. Instr. Meth. Phys. Res. A525 (2004), pp. 582-592.

[2] S. Konegger-Kappel, et al <https://www.iaea.org/sites/default/files/19/07/cn-267-book-of-abstracts.pdf>, CN267-226, pp.228.

Keyway broach residual stress measurement

Neutron Physics Laboratory - Neutron diffraction

David Hradil

Proposal ID

335

Report regarding proposal „Keyway broach residual stress measurement“

D. Hradil, J. Hodek, M. Duchek, COMTES FHT, Dobruška, Czech Republic
Ch. Hervoches, Nucl. Physics Inst., Rez, Czech Republic

The samples in shape of bar with rectangular cross-section with cutting part (teeth) typical for keyway broaches is made of high speed steel 1.3343. These samples were chemically heat treated including quenching, cryo treatment, tempering and nitriding. Influence of residual stresses wasn't investigated yet on this type of tools (keyway broaches). Microstructure of the samples will be due to quenching fully martensitic with some amount of carbides, this is one of the advantages for the FEM model because there will be not many phase transformations. Nitriding in this process only increase the surface hardness and wear resistance, there is no effect on microstructure inside the tool. Main reason for these investigations was to calculate residual stresses after chemical heat treatment. On Fig. 1 you can see real keyway broach and simplify version of this tool – that was investigated.



Fig. 1 Keyway broach - real tool (left) and simplify tool (right)

In total there were 3 samples with different chemical heat treatment + 1 sample with no internal stresses. The biggest differences we can see in these two measurements (Fig. 2). Left sample were quenched with pressure 1.5 bars, right sample were quenched with pressure 6 bars. This is main reason why the values of internal stresses are so different. For better understanding of whole chemical heat treatment is necessary to use same quenching parameters. Effect of cryo treatment is not visible.

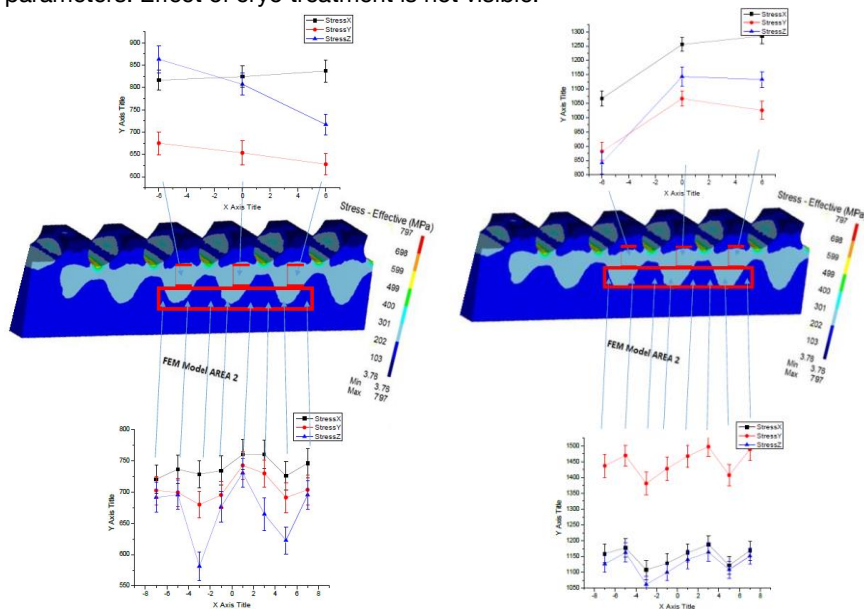


Fig. 2 Results of residual stresses by neutron diffraction (low quenching pressure - left), (high quenching pressure - right)

For comparing the results we used Contour method – experimental-computational method (3D surface measurement and FEM calculations). The results of this method are not relevant, because of very small geometry of the samples. Contour method is not usable for this small measurement area. v04 – sample with highest range of internal stresses correspond with result by neutron diffraction – high quenching pressure.

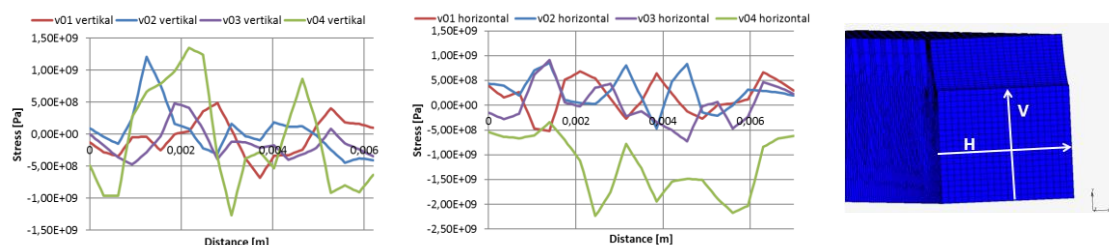


Fig. 3 Contour method measurement - same samples, vertical and horizontal direction of measuring

For better understanding of influence by different chemical heat treatment processes, we need use same quenching pressure. For contour method is recommend larger area of investigation. Keyway broach with small area of investigation is not applicable for contour method.

ACKNOWLEDGMENT

"Measurements were carried out at the CANAM infrastructure of the NPI CAS Rez supported through MEYS project No. LM2011019."

Thermal and concentration evolution of nuclear and magnetic structures of $\text{PbFe}_{2/3}\text{W}_{1/3}\text{O}_3$ doped by S

Neutron Physics Laboratory - Neutron diffraction

Roland Tellgren

Proposal ID

338

Effect of Sc doping on structural and magnetic properties of $\text{Pb}(\text{Fe}_{2/3}\text{W}_{1/3})\text{O}_3$ multiferroic.

S. A. Ivanov^a, P. Beran^b, R. Tellgren^c

a -Department of Engineering, Box 534, Uppsala University, SE-751 21 Uppsala, Sweden

b-Nuclear Physics Institute, ASCR, CZ - 250 68 Řež, Czech Republic

c- Department of Chemistry, Uppsala University, Box 538, SE-751 21 Uppsala, Sweden

The purpose of this study was to investigate the nuclear and magnetic structure when Sc cation is substituted at the B-site in $\text{Pb}(\text{Fe}_{2/3}\text{W}_{1/3})\text{O}_3$. It is well known that the physical properties of this perovskite multiferroic are strongly correlated with some structural factors, among them the order–disorder phenomena between the octahedral site atoms. The most important structural features that affect the long-range order of the B-cations are various and well known, such as the charge and ionic radius difference between the B-site atoms and its electronic configuration, and the size ratio between A and B atoms.

The new double perovskites $\text{Pb}[(\text{Fe}_{1-x}\text{Sc}_x)_{2/3}\text{W}_{1/3}]\text{O}_3$ solid solutions ($0 < x < 0.4$) were synthesized by standard ceramic procedures.

From XRPD data the oxygen location cannot be determined accurately in the presence of heavy atoms such as Pb, thus an NPD study was essential to investigate the structural features of these perovskites, neutrons being more sensitive to the oxygen positions. The scattering factors of Sc, W and Fe are also very contrasting for neutrons, which is important to assess the long range ordering between these atoms. NPD data were collected at different temperatures on diffractometer MEREDIT (Řež, Czech Republic) with the wavelength of 1.46 Å. Data were collected between 4 and 148° in 2θ with a step length of 0.08° (Fig.1)

The structural refinements of NPD data were performed in the $Fm\bar{3}m$ space group (No. 225). In this model, Sc, Fe and W atoms were distributed at the 4a and 4b crystallographic Wyckoff sites, O atoms at the 24e sites and finally the Pb atoms occupy the 32f (x,x,x) sites, presenting an off-centre displacement along the [111] direction. Because three metal cations are distributed over two sites, the refinements of occupation factors the use of several restraint functions was required (Fig.2)

To determine the possible magnetic moment arrangements compatible with the symmetry of the crystal structure of $\text{Pb}[(\text{Fe}_{1-x}\text{Sc}_x)_{2/3}\text{W}_{1/3}]\text{O}_3$ the representation analysis has been performed using the BasIreps program, included in the FullProf Suite package [1]. Owing to non-equivalent distribution of Fe spin between two B-site positions the magnetic structure is ferrimagnetic below T_N , which remarkably decreases with Sc concentration.

The temperature evolution of magnetic moment for different Sc concentrations is presented in Figure 3.

[1] Rodriguez-Carvajal, J. (1993). Physica B, 192, 55.

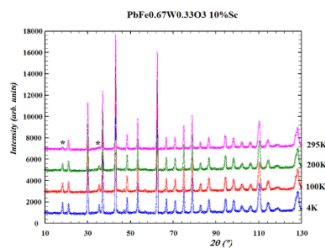


Fig 1

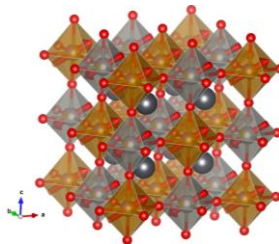


Fig 2

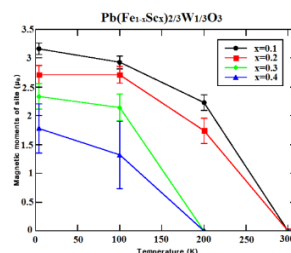


Fig3

Neutron activation analysis screening of hazardous elements in dump soils

Neutron Physics Laboratory - Nuclear analytical methods with neutrons

Ivana Krausová

Proposal ID

339

Neutron activation analysis screening of hazardous elements in dump soils

As we expected, the instrumental neutron activation analysis determined some hazardous elements (As, Cd, Co, Cr, Cu, Mo, Ni and Zn) in dump soils in the Kladno-Buštěhrad, Central Bohemia. Content of hazardous elements increased in several times compared with maximum permissible limits confirms its anthropogenic origin, probably from the operation of former coal mines the Poldi Steelworks. The standard reference materials were used to accuracy procedure at the investigated matrix with satisfied agreement. Most of hazardous elements are included in the group of extraneous substances that can significantly contribute to contamination of agricultural soils. A potential risk was expected in the long term because of this area was not fenced. Especially new inhabitants do not know what lies inside of this area and therefore they are under risk.

The results of our investigation will be published in an impacted paper and student's diploma thesis.

Measurements were carried out at the CANAM infrastructure of the NPI CAS Řez supported through MEYS project No. LM2011019.

Residual stress measurement extension for contour cut method

Neutron Physics Laboratory - Neutron diffraction

Josef Hodek

Proposal ID

340

Final report 'Residual stress measurement extension for contour cut method'

J. Hodek, A. Prantl, COMTES FHT a.s., Dobruany, Czech Republic

Residual stress is hard to obtain for bulk objects. The contour method can determine residual stress distribution for bulk objects. The neutron diffraction measurement was done to obtain measurement that can be comparable to the contour method computation and the finite element method computation of the heat treatment. The sample is a cylinder of 316L material D30/60mm. The residual strains were measured along three radial lines (distant 120° from each other) in three directions (Radial, Hoop, Axial) using a 3x3mm slit, from ~3mm below the surface to maximal possible depth, with a step size of 3mm. The residual stress was computed from measured strains [1]. The computed stresses were compared for FEM computed stresses see Fig. 2-Fig. 10 (where FEM means computation in R - radial, H - hoop and A - axial direction and N means stress computed from neutron stress measurement in 1, 2, 3 measurement direction). The FEM model and contour method stresses were examined and analysed.

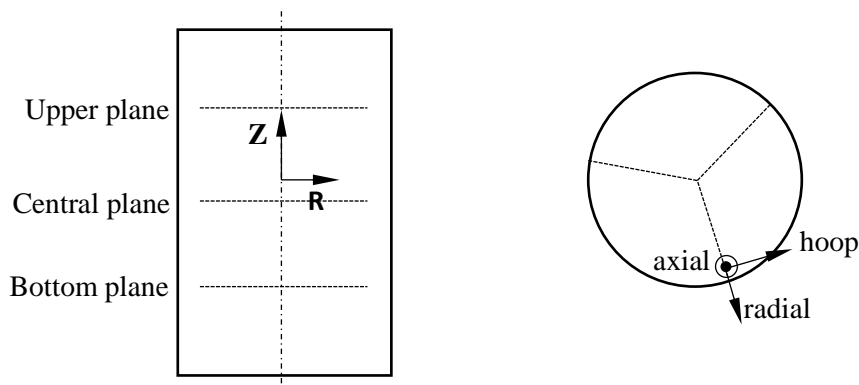


Fig. 1 Schematic of planes and directions of measurement and measured deformation directions

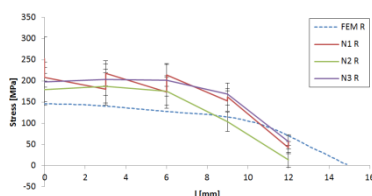


Fig. 2 Stress radial - central plane

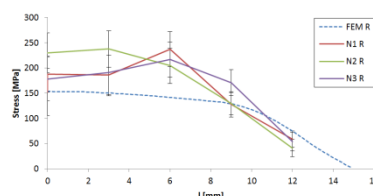


Fig. 3 Stress radial - bottom plane

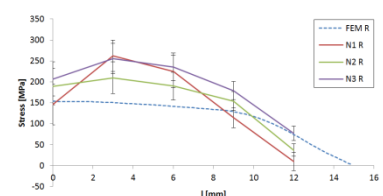


Fig. 4 Stress radial - upper plane

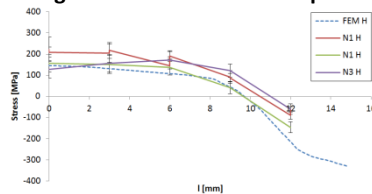


Fig. 5 Stress hoop - central plane

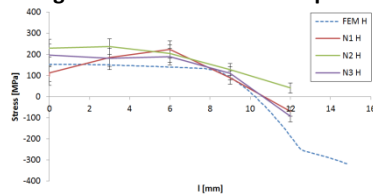


Fig. 6 Stress hoop - bottom plane

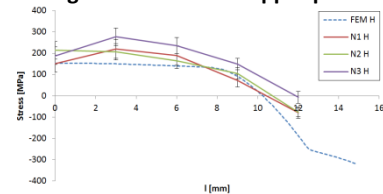


Fig. 7 Stress hoop - upper plane

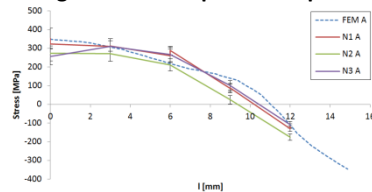


Fig. 8 Stress axial - central plane

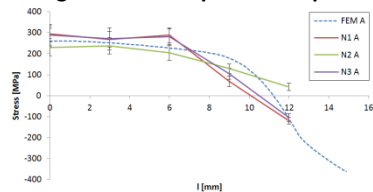


Fig. 9 Stress axial - bottom plane

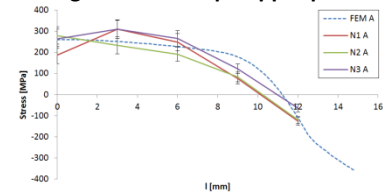


Fig. 10 Stress axial - upper plane

[1] HUTCHINGS, Michael T., et al. *Introduction to the characterization of residual stress by neutron diffraction*. CRC press, 2005.

Cross-section measurements of the $^{16}\text{O}(\text{n,tot})$ reaction in the neutron energy range 20-35 MeV

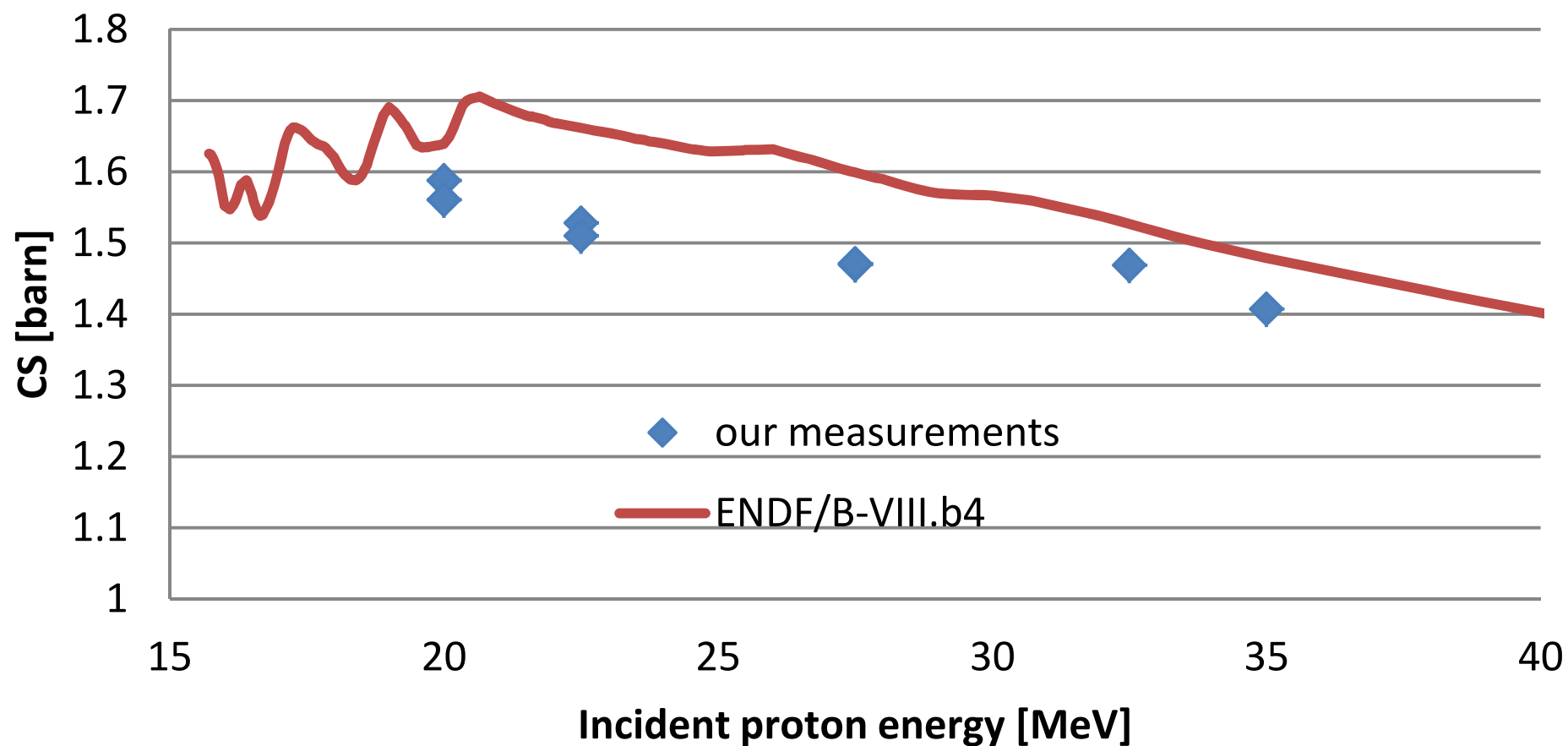
Laboratory of Cyclotron and Fast Neutron Generators

Mitja Majerle

Proposal ID

279

O-16 (n,tot) reaction CS



Bright fluorescent nanodiamonds with controlled shape

Laboratory of Cyclotron and Fast Neutron Generators

Petr Cígler

Proposal ID

152

Report regarding project “Bright fluorescent nanodiamonds with controlled shape”

Proposer: Petr Cígler, Institute of Organic Chemistry and Biochemistry of the CAS

Registered co-proposer: Jan Štursa, Institute of Nuclear Physics of the CAS

In this project we focused on shaping of nanodiamond (ND) particles to become pseudospherical and on generation of fluorescence defects in these NDs. First, the NDs were chemically processed to round their crystalline interface. We used molten potassium nitrate which caused a controllable etching of crystal edges and vertexes. Using this material, we performed the irradiation experiments in cyclotron to generate vacancies according to the planned scheme, including control particles without etched surface. The resulting irradiated NDs were annealed to generate fluorescent NV centers. In this way we successfully produced both pseudospheric and angular fluorescent NDs. We evaluated their spectral properties and characterized them with various physico-chemical methods (such as zeta potential measurements, dynamic light scattering, transmission electron microscopy, Raman spectroscopy). Using the prepared fluorescent NDs we have performed 7 studies [1-7] which all have been published in high impact journals. We also wrote one chapter for *Methods in Pharmacology and Toxicology* series. Another manuscript has been recently submitted.

References dedicated to the project:

- 1) Petrakova V., Rehor I., Štursa J., Ledvina M., Nesladek M., Cígler P.: Charge-sensitive fluorescent nanosensors created from nanodiamonds. *Nanoscale*, **2015**, 7, 12307-12311.
- 2) Slegerova J., Hajek M., Rehor I., Sedlak F., Štursa J., Hruby M. and Cígler P. Designing the nanobiointerface of fluorescent nanodiamonds: highly selective targeting of glioma cancer cells. *Nanoscale*, **2015**, 7, 415-420.
- 3) Havlik J., Raabova H., Gulka M., Petrakova V., Krecmarova M., Masek V., Lousa P., Štursa J., Boyen H.-G., Nesladek M., Cígler P.: Benchtop Fluorination of Fluorescent Nanodiamonds on a Preparative Scale: Toward Unusually Hydrophilic Bright Particles. *Adv. Funct. Mater.*, **2016**, 26, 4134–4142.
- 4) Štursa J., Havlik J., Petrakova V., Gulka M., Ralis J., Zach V., Pulec Z., Stepan V., Zargaleh S. A., Ledvina M., Nesladek M., Treussart F., Cígler P.: Mass production of fluorescent nanodiamonds with a narrow emission intensity distribution. *Carbon*, **2016**, 96, 812-818.
- 5) Petrakova V., Benson V., Buncek M., Fiserova A., Ledvina M., Štursa J., Cígler P. and Nesladek M.: Imaging of transfection and intracellular release of intact, non-labeled DNA using fluorescent nanodiamonds. *Nanoscale*, **2016**, 8, 12002–12012.
- 6) Vavra J., Rehor I., Rendler T., Jani M., Bednar J., Baksh M. M., Zappe A., Wrachtrup J., Cígler P.: Supported lipid bilayers on fluorescent nanodiamonds: a structurally defined and versatile coating for bioapplications. *Adv. Funct. Mater.* **2018**, 1803406.
- 7) Havlik J., Petrakova V., Kucka J., Raabova H., Panek D., Stepan V., Zlamalova Cilova Z., Reineck P., Štursa J., Kucera J., Hruby M., Cígler P.: Extremely rapid isotropic irradiation of nanoparticles with ions generated in situ by a nuclear reaction. *Nature Comm.* **2018**, DOI: 10.1038/s41467-018-06789-8.

Book Chapter:

Neburkova J., Hajek M., Rehor I., Schimer J., Sedlak F., Štursa J., Hruby M., and Cígler P.: Targeting Glioma Cancer Cells with Fluorescent Nanodiamonds via Integrin Receptors. In *Methods in Pharmacology and Toxicology*, E. Patsenker (ed.). pp. 169-189, Humana Press, New York, NY 2018.

Distribution of cellulosic particles

Neutron Physics Laboratory - Neutron diffraction

Pavel Strunz

Proposal ID

344

Measurements at double-bent-crystals SANS instrument MAUD

(<http://neutron.ujf.cas.cz/en/instruments/lvr15/5-hk8a>) of the Neutron Physics Lab

(<http://neutron.ujf.cas.cz>). July 20-21 2017.

Samples were measured in quartz Hellma[™] cells with flight path of 1 mm. Three instrumental setups were used in order to cover wide Q-range ($3 \cdot 10^{-4} \div 2 \cdot 10^{-2} \text{ \AA}^{-1}$). The raw data were treated with subtraction of scattering from buffer sample (D_2O in 1 mm cell) and cadmium as background.

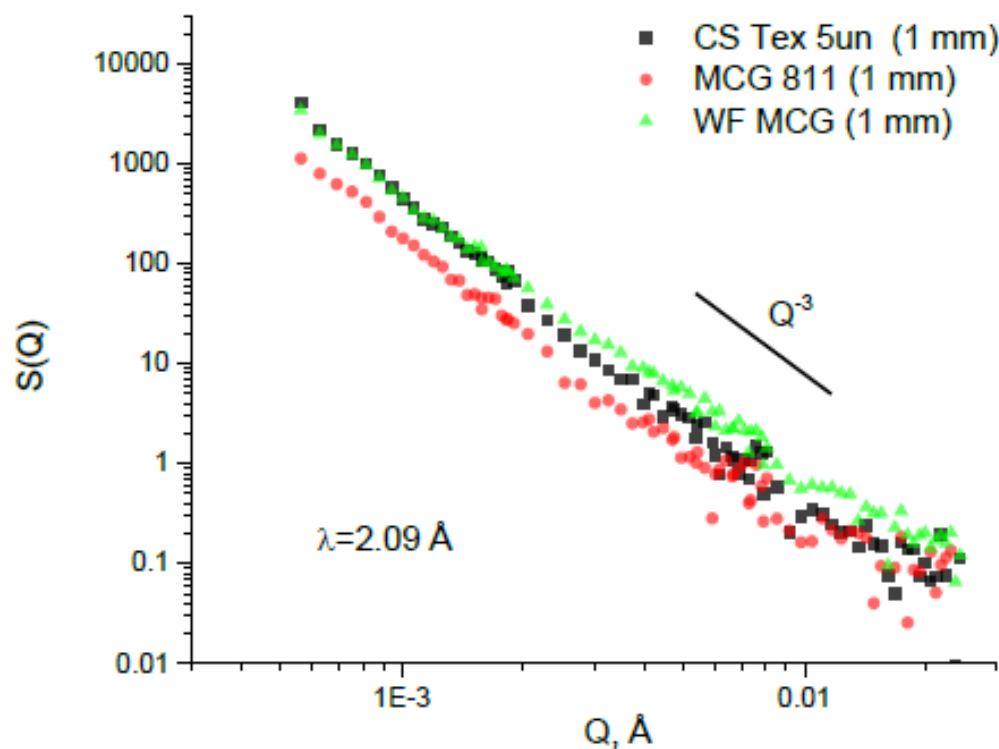


Fig. 1. SANS functions of BC samples.

Interaction of detonation nanodiamond clusters in thixotropic aqueous suspensions

Neutron Physics Laboratory - Neutron diffraction

Oleksandr Tomchuk

Proposal ID

280

Report regarding proposal “Interaction of detonation nanodiamond clusters in thixotropic aqueous suspensions”

O.V. Tomchuk, M.V. Avdeev, FLNP JINR, Russia

A.T. Dideikin, A.E. Alexenskii, A.Ya. Vul, Ioffe Physical-Technical Institute, Russia

V. Ryukhtin, Nucl. Physics Inst., Rez, Czech Republic

Detonation nanodiamond (DND) aqueous suspensions are of current interest in view of their developing technical and, especially, biomedical applications. Despite the electrostatic stabilization, there is a tendency in DND suspensions toward the aggregation. Nevertheless, DND suspensions remain stable as a whole showing a cluster-cluster interaction which can lead to rheological effects such as thixotropy. SANS study ($q_{\min} \approx 0.1 \text{ nm}^{-1}$) found no differences between the cases of positively and negatively stabilized DND particles, i.e. on the nanoscale two type of suspensions are absolutely identical [1]. Thus, special interest is the study of the interaction of diamond clusters on submicron-micron structural level, because this may be the cause of mentioned thixotropic effect, and VSANS experiment was required.

Neutron VSANS experiments were performed on DND suspensions with concentrations 5.05 wt.% and 2.25 wt.% using the MAUD instrument. The motivation for the experiments was to determine details of the structure and interaction in aqueous suspensions with positive charge stabilization produced by annealing detonation nanodiamonds (DND) in hydrogen atmosphere on a submicron scale to explain the macroscopic rheological properties.

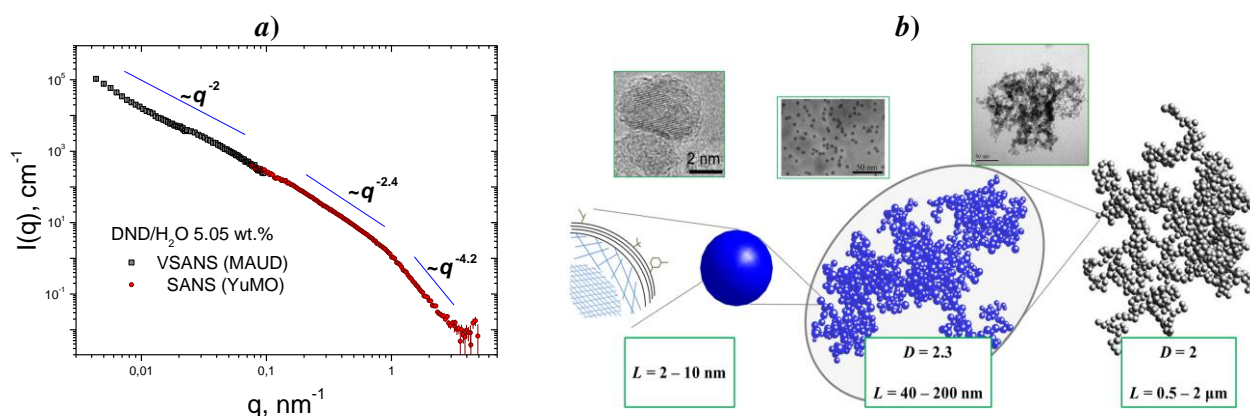


Fig. 1. *a)* Example VSANS/SANS data for DND/water system. Straight lines indicate the ranges of power-law scattering characteristic for scattering by a diffuse surface of detonation diamond nanoparticles (large q), the fractal structure of clusters (intermediate q), and the fractal structure of secondary associates (smallest q), respectively. *b)* The proposed schematic view of the multilevel structure of the aqueous suspension of detonation nanodiamonds with positive charge stabilization based on scattering data.

The investigation of the DND-water suspension on the MAUD diffractometer allowed us to detect the structural level of the secondary association of nanodiamond fractal clusters on a submicron scale, which is responsible for the rheological properties of the system, and more specifically for thixotropy. The data significantly expand the range of scattering vectors available to standard small-angle neutron instruments, and at the same time are well matched in the crossover range. Mentioned structural level is a gaussian-like fractal network connecting the primary fractal clusters of nanodiamonds. It is unstable, because it can be destroyed by a small mechanical shock (shaking), but it is restored during the day. This effect is an exceptional feature of systems with positive charge stabilization and is not observed in previously investigated systems with negative charge stabilization.

Elemental Composition of High Entropy Alloy Sample

Neutron Physics Laboratory - Nuclear analytical methods with neutrons

Kateina Dragounová

Proposal ID

282

Report on instrumental neutron activation analysis of HEA sample

A flat piece of a High Entropy Alloy (HEA) of approximately rectangular shape (3 x 8 mm, ~ 1 mm thick) was available for analysis. It was broken in a clamp with its jaws covered with phenol formaldehyde resin bonded paper (FR-2 material) to avoid contamination into six pieces with masses in the range of 45 – 137 mg. To make sure that no contamination occurred, the broken pieces were shortly boiled in 0.1 M HNO₃ prepared from sub-boiled HNO₃ diluted with deionized water, so that about 0.5 % of the original sample mass was dissolved. The cleaned samples were washed with ethylalcohol and air dried. The samples were heat sealed into pre-cleaned polyethylene (PE) disk shaped capsules made by sealing PE foils of 0.2 mm thickness with 25 mm and 20 mm diameter for irradiation with thermal and epithermal neutrons, respectively. For quality control purposes, 75 – 100 mg aliquots of NIST standard reference material (SRM) 1633b Constituent Elements in Coal Fly Ash were prepared for irradiation as the HEA samples.

Three modes of INAA based on irradiation in the experimental reactor LVR-15 of the Research Centre Řež were used with minor modifications. Short-time irradiation for 30 s with the whole reactor neutron spectrum (S-INAA) was carried out in an irradiation channel located at the outskirts of the active core behind a beryllium reflector, in which fluence rates of thermal, epithermal and fast neutrons were 3.2×10^{13} , 1.1×10^{13} , and 1.1×10^{13} cm⁻² s⁻¹, respectively. Short-time irradiation for 45 s with epithermal and fast neutrons (S-ENAA) was carried out in the same channel. Thermal neutrons were shielded off by placing the samples into a disk shaped Cd box with 1-mm thick walls. Both short-time irradiation modes were carried out using a pneumatic facility with transport time of 3.5 s. The samples, MES calibrators, blank PE capsules and quality control samples were irradiated individually together with neutron flux monitors (5-mg disks of 0.1% Au–Al foil, IRMM, Belgium, Nuclear reference material IRMM-530a, 0.1mm thickness) to check the neutron fluence rate stability in time. Long-time irradiation for 2 h with the whole reactor neutron spectrum (L-INAA) was performed in a channel located in the Be reflector, in which fluence rates of thermal, epithermal and fast neutrons were 3.6×10^{13} , 8.4×10^{12} , and 8.6×10^{12} cm⁻² s⁻¹, respectively. In this case, the samples, MES calibrators, blank PE capsules and quality control samples were stacked together to form a column that was inserted into an aluminium irradiation can. Iron monitors (50-mg disks) were inserted between each set of 5 samples and/or calibrators to determine the axial neutron flux gradient. The sample masses for S-INAA and S-ENAA were in the range of 45 – 88 mg, those for L-INAA spanned from 116 mg to 137 mg. Gamma-ray spectrometry measurements were performed using two coaxial HPGe detectors. Both HPGe detectors were interfaced to a Canberra Genie 2000 computer controlled gamma-spectrometry analyzer through a chain of associated linear electronics, which included a Canberra 599 Loss Free Counting module to correct the variable count-rate and dead time. Canberra Genie 2000 software was used for evaluation of gamma-ray spectra.

A proxy analysis using X-ray fluorescence analysis was also carried out to assay Pb, which cannot be determined by INAA. The analysis performed at two 0.25x0.25 mm spots yielded Pb concentrations of 1.075% and 1.200 %. The results obtained may be biased ± 20 % rel., because no matrix matched calibration material was available.

Conclusion

The INAA measurement provided the required elemental composition of the tested HEA sample. Concentration of Pb amounting ca 1.1 %wt. was determined from the X-ray fluorescence analysis. The obtained INAA results were presented, together with other characterizations of the sample, at the 18th International Conference on Texture of Materials (ICOTOM-18) in St. George, Utah, USA, and the related paper submitted to IOP Journal of Physics C.

Ex-situ & In-situ investigation of CP Titanium grade 2 prepared by CONFORM ECAP and rotary swaging

Neutron Physics Laboratory - Neutron diffraction

Gergely Németh

Proposal ID

347

Report regarding proposal “Ex-situ & In-situ investigation of CP Titanium grade 2 prepared by CONFORM ECAP and rotary swaging” Gergely Németh, Charles University, Czech Republic

Neutron diffraction experiments were performed on commercially pure titanium grade 2 specimens in the following 9 conditions: without mechanical treatment (initial state), after 1x, 2x and 3x passes through CONFORM ECAP machine and these same conditions were applied on other samples before they underwent an additional mechanical treatment using the rotary swaging method. Finally, one sample was heat treated (HT). Samples were in the form of cylindrical rods with diameter 10 mm (only CONFORM ECAP samples) and 4,68 mm (rotary swaged samples).

101 and 002 reflections were measured for a few hours on each sample. The gauge volume was placed in the center of specimens. Residual strains were calculated from the position of diffraction peaks relative to the position of diffraction peaks of material in the initial state. FWHM were determined from diffraction peaks too. The results are on *fig.1 a, b, c, d*.

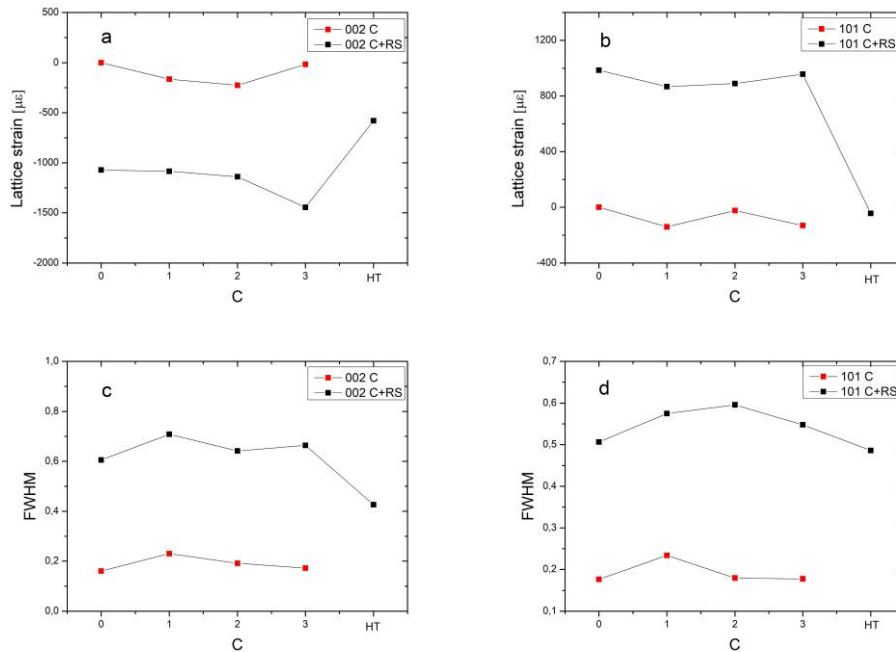


Fig.1-a, b) Calculated residual strains c, d) Determined FWHM as the function of number of passes through CONFORM ECAP (C-CONFORM ECAP, C+RS-CONFORM ECAP + rotary swaging; HT-Heat treated)

From *fig. 1-a* and *b* we can deduce that rotary swaging generated an additional residual macro-strain with tensile character in the case of reflection 002 and residual macro-strain with compression character in the case of 101 reflection. The CONFORM ECAP treatment has the effect of residual macro-strain with tensile character. On *fig. 1-c* and *d* it is seen that rotary swaging increased three times the value of FWHM parameter which may be caused by increased crystallographic defects in the material after the cold working process. In case of the samples treated only with CONFORM ECAP, after the first pass, FWHM is increased slightly but after the second and third pass FWHM was almost recovered to the initial state.

In-situ neutron diffraction during heat treatment was carried out on samples in conditions: passed 1x CONFORM ECAP machine and 1x CONFORM ECAP + rotary swaged. Heat treatment was stepwise. Temperature steps were 20 K and the holding time was 1 hour. During this time neutron diffraction data were collected. The temperature range was 100 °C – 600 °C. The measured reflection was the 002 reflection. The results are on *fig. 2-a* and *b*.

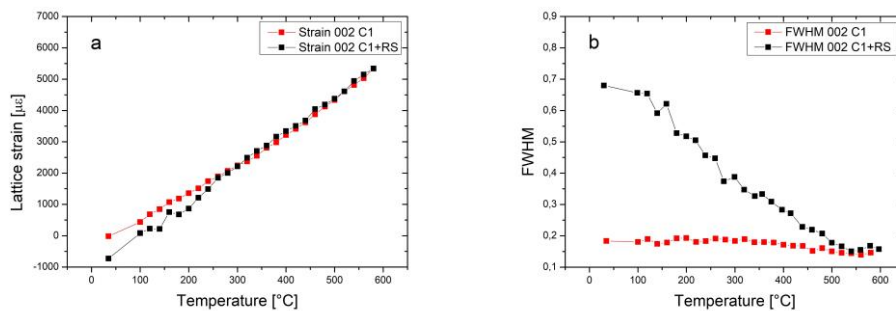


Fig.2 a) Calculated strain, b) Determined FWHM, as the function of temperature

On *fig. 2-a* it is seen that the difference in residual macro-strains between two samples vanished above 350 °C. However, in the case of rotary swaged sample the FWHM parameter is decreasing continuously until it reaches the value of FWHM parameter of the sample treated only with CONFORM ECAP method.

The correlation of the gained results with results from other experimental methods is still in progress.

Comparative study of performance of Silicon and Silicon Carbide detectors during RBS and ERDA.

Laboratory of Tandetron

Lorenzo Torrisi

Proposal ID

348

Comparative study of performance of Silicon and Silicon Carbide detectors during RBS and ERDA

L. Torrisi¹, V. Havranek², M. Cutroneo², A. Mackova² and A. Torrisi²

¹Dipartimento di Scienze Fisiche MIFT, Università di Messina, Italy

²Nuclear Physics Institute, AS CR, Rez, Czech Republic

SiC are able to detect radiation at low and high energy, due to the controllable active region depth using adapt inverse bias of the Schottky barrier in presence of a thin surface metallization of contact. We have demonstrated that it is possible to use SiC diodes to detect helium ions with energy in the range of about 0.1–6.0 MeV with a sufficient energy resolution, similar to that of silicon detectors, capable to be employed for qualitative and quantitative RBS analyses. The experiment was performed using a prototype diode with a surface metalized semiconductor, 200 nm thickness in Ni₂Si alloy, with up to 80 μ m active region depth, using a bias of –200 V at which this active region is reduced to about 20 μ m active region. Such devices permit to distinguish ions of different energy, i.e. atomic numbers of different targets using RBS analysis and ion currents. Results demonstrated that the SiC energy resolution is comparable to that of Si, although worse. Si-barrier detector show higher energy resolution that permits to acquire significant RBS spectra using 1–6 MeV helium beam and SiC can be tailored designed to have a similar energy resolution. In this way, the surface metallization thickness must be reduced in order to reduce the ion energy loss and straggling in this passive absorber. The detection electronic line has been optimized to improve the impedance matching of the devices with the preamplifier, in order to improve the signal-to-noise ratio.

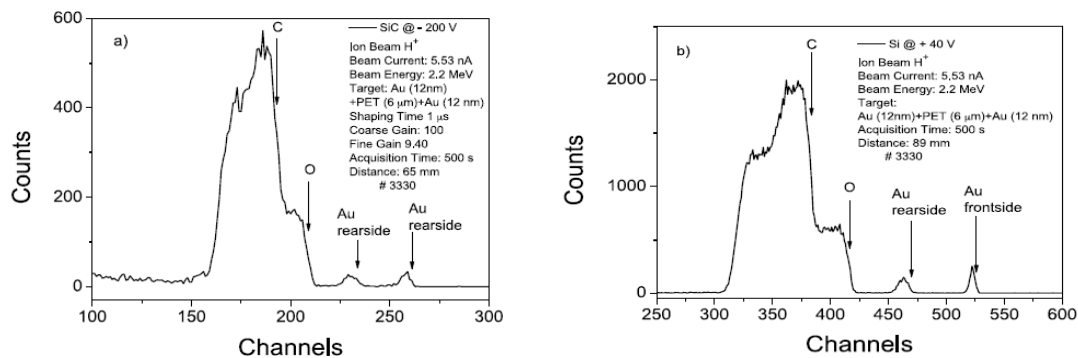


Fig.1: RBS comparison analysis obtained using 2.2 MeV proton energy, 5.5 nA current, with 500 s acquisition time, irradiating a thin polymeric (PET) film with 6 μ m thickness, covered in front and back by 12 nm Au gold film acquired using SiC (a) and Si (b) detectors.

It is important to remind that SiC is superior to Si for some advantages, such as the higher energy gap that permits to be transparent to visible radiation and to be used to detect ions also in presence of high visible radiation, such as in plasmas ion emission or during ion irradiations of insulators, such as oxides and ceramics, emitting high fluorescent light intensity. SiC shows a lower reverse current, of about 10 pA at room temperature, two order magnitude lower with respect to Si, conferring higher sensitivity to the device. SiC is radiation resistant due to the higher bonding energy Si-C with respect to Si-Si, making it possible to use even in harsh conditions, such as plasmas and high temperatures, giving rise to a damage threshold due to absorbed doses much higher than that in silicon. Thus, SiC can be employed also to monitor on-line ion beams and lasers interacting with solids, to detect the radiations emitted from low and high temperature plasmas and to observe ion scattering processes from many materials. Their use can be optimized not only at low ion energy but also at high ion energy, increasing the active depth of the sensible detector region. Moreover their optimization can be performed also to detect UV, soft and hard X-rays and electrons generated by different sources, such as pulsed plasmas and particle beams.

References:

- 1) L. Torrisi, V. Havranek, M. Cutroneo, A. Mackova, L. Calcagno, A. Cannavò and A. Torrisi, “SiC detector for high helium energy spectroscopy”, *NIM A* 903 (2018) 309–316.
- 2) A. Sciuto, G. D’Arrigo, S. Di Franco, M. Mazzillo, G. Franzò, L. Torrisi, and L. Calcagno, “4H-SiC Detector in High Photons and Ions Irradiation Regime”, *IEEE Trans. on Electron Devices* 65(2), 2018, 599-604.
- 3) A. Torrisi, P.W. Wachulak, H. Fiedorowicz, and L. Torrisi, “SiC detectors for evaluation of laser-plasma dynamics employing gas-puff targets”, *Nucl. Instr. and Meth. A*, 922 (2019) 250–256.

Investigation of residual strains of commercially pure Titanium grade 2 prepared by CONFORM ECAP

Neutron Physics Laboratory - Neutron diffraction

Gergely Németh

Proposal ID

349

Report regarding proposal “Investigation of residual strains of commercially pure Titanium grade 2
prepared by CONFORM ECAP”
Gergely Németh, Charles University, Czech Republic

Neutron diffraction experiments were performed on commercially pure titanium grade 2 specimens in the following 4 conditions: without mechanical treatment (initial state), after 1x, 2x and 3x passes through CONFORM ECAP machine. The samples were in cylindrical shape with diameter ~ 10 mm and length 80 mm. The samples were placed on the xyz stage which allowed samples to move in any direction. The sample gauge volume was $\sim 32,5$ mm³. Three scans were performed along the same line on each sample according to diffraction vector orientation in the sample's coordinate system: a scan, where diffraction vector was parallel to - axial direction \vec{q}_A , radial direction \vec{q}_R and hoop direction \vec{q}_H . The measured 2θ angles of reflection (10 $\bar{1}$ 1) in initial state sample between points -2 and 2 served as the strain free reference for further calculation of residual strains, because they did not show any gradient (Fig. 1. a). The calculated lattice strains in three directions (axial, radial, hoop) for each sample are shown in Fig. 1. b, c and d.

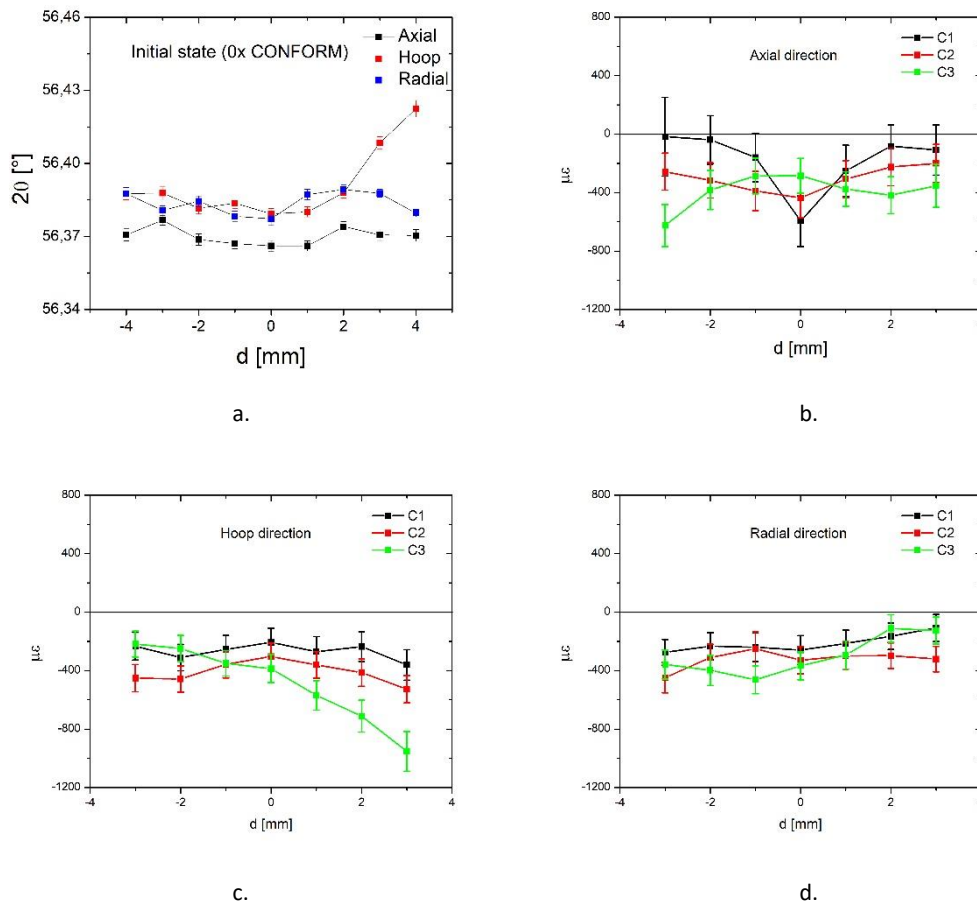


Fig.1.-Measured 2θ angles of (a) initial state sample and the lattice strain distribution relative to the centre of the samples ($d=0$ mm) in b. axial, c. hoop, d. radial direction after 1, 2 and 3 passes of CONFORM ECAP treatment

On the Fig. 1.b. it is seen that the sample after 1x CONFORM ECAP treatment (C1) exhibits large lattice strain gradient towards the edges in the axial direction. Between points -3 and 3 mm there is a symmetric distribution of the strains around the centre. However, the lattice strain in the hoop (c) and in the radial (d) direction shows relatively homogeneous distribution. Concerning the sample after 2x CONFORM ECAP treatment (C2), the large gradient of the lattice strain after the first pass in the axial direction was removed and the sample exhibits a symmetrical distribution for axial (b) and hoop (c) directions between points -3 and 3 mm. The lattice strain distribution in the sample after 3x CONFORM ECAP treatment (C3) does not show any symmetry and there are relatively big differences in the values in all three directions except points between -2 and 0. In general, residual strains with compression character prevail in all samples.

The gained results indicate that further investigations are needed to clarify the reasons of the differences between the samples.

Structural modifications of metallic glasses by neutron irradiation

Laboratory of Cyclotron and Fast Neutron Generators

Marcel Miglierini

Proposal ID

286

Report regarding the experiment ID-286 “Structural modifications of metallic glasses by neutron irradiation”

Marcel Miglierini, Milan Štefánik and Martin Cesnek

Samples of Fe-based metallic glasses were prepared in a form of ribbons about 1-6 mm wide and about 23 microns thick. The following compositions were produced: $\text{Fe}_{76}\text{Mo}_8\text{Cu}_1\text{B}_{15}$, $\text{Fe}_{79}\text{Mo}_8\text{Cu}_1\text{B}_{12}$, $\text{Fe}_{79}\text{Nb}_7\text{Cu}_1\text{B}_{13}$, and $\text{Fe}_{78}\text{Si}_9\text{B}_{13}$. They were exposed to irradiation with neutrons obtained at the fast neutron facility based on the U-120M isochronous cyclotron of the NPI CAS in Rez.

Irradiation experiments were accomplished during two runs (10.6. and 26.8.2016) to obtain higher total neutron fluences. In both experiments, the p(35)+Be accelerator-driven neutron source with broad spectrum up to 33 MeV was used. The estimated total neutron fluences of $2.7 \times 10^{16} \text{ n/cm}^2$ at the position of the investigated samples were obtained. After each run, gamma as well as Mössbauer spectra were acquired. The first one served as test for production of radioactive nuclides. The latter spectra were used for assessment of radiation induced effects in the amorphous samples.

As an example, Mössbauer spectra recorded before and after one irradiation cycle are shown in Fig. 1 (left). For $\text{Fe}_{78}\text{Si}_9\text{B}_{13}$ metallic glass, obvious deviations in the intensities of the second and the fifth spectral lines are clearly seen. After irradiation, intensities of these lines have increased which indicates rearrangement of magnetic moments of the resonant atoms. They tend to rotate towards the plane of the ribbon. Such repositioning is caused by internal stresses due to topological modifications of the constituent atoms. So even though the samples are amorphous, we could reveal subtle modifications via magnetic moments.

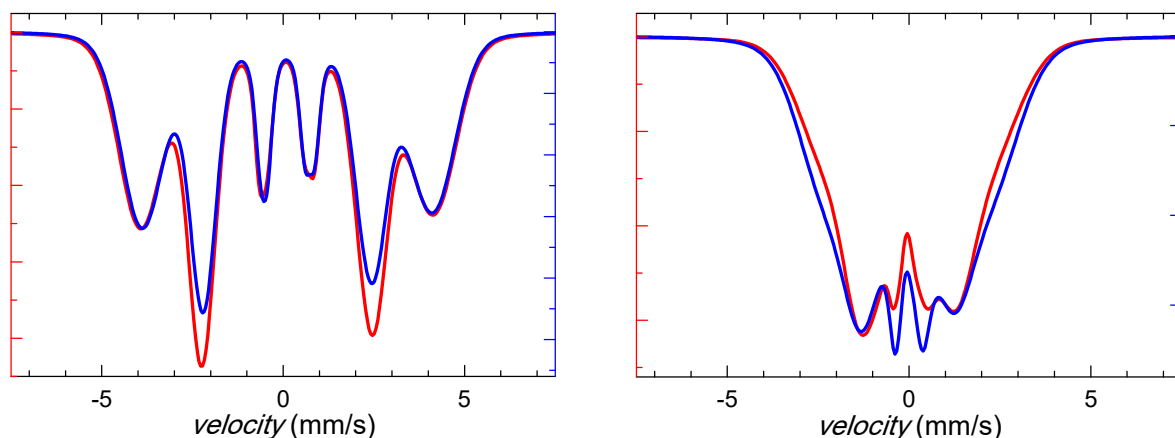


Fig. 1. Mössbauer spectra of as-quenched (blue) and neutron irradiated (red) $\text{Fe}_{78}\text{Si}_9\text{B}_{13}$ (left-hand panel) and $\text{Fe}_{79}\text{Nb}_7\text{Cu}_1\text{B}_{13}$ (right-hand panel) metallic glasses.

While the Fe-Si-B metallic glass is ferromagnetic at room temperature, another irradiated amorphous samples are only weakly magnetic. Right-hand panel of Fig. 1 exhibits the case of the $\text{Fe}_{79}\text{Nb}_7\text{Cu}_1\text{B}_{13}$ metallic glass. Here, opposite tendency of the moment rotation is observed. In addition, subtle decrease of hyperfine magnetic fields is demonstrated by narrowing of the spectral signal.

We have irradiated also samples of corrosion-resistant steel. As this material features crystalline structure, non-significant deviations were observed in the corresponding Mössbauer spectra.

Fabrication of ion implanted integrated optical elements

Laboratory of Tandetron

István Bányász

Proposal ID

351

Report on project “Fabrication ion implanted integrated optical elements”

I. Bányász, Wigner Research Centre for Physics, Budapest, Hungary

I. Rajta, G.U.L. Nagy, Atomki, Institute for Nuclear Research, Debrecen, Hungary

V. Vosecek, V. Havránek, Nucl. Physics Inst., Řež, Czech Republic

1.

2. Channel waveguides and Mach-Zehnder microinterferometers

We planned to fabricate the channel waveguides and Mach-Zehnder interferometers with tapering, coupling gratings and with improved lateral confinement.

Experiments completed

The following structures have been fabricated:

1. Single channel waveguides in a KTP crystal, 5 MeV N^{3+} microbeam, fluence = $5 \cdot 10^{14}$ - $8 \cdot 10^{15}$ ions/cm².
2. Mach-Zehnder microinterferometers in a KTP crystal, 5 MeV N^{3+} microbeam, fluence = $5 \cdot 10^{14}$ - $8 \cdot 10^{15}$ ions/cm².
3. Single channel waveguides in a RTP crystal, 5 MeV N^{3+} microbeam, fluence = $5 \cdot 10^{14}$ - $8 \cdot 10^{15}$ ions/cm².
4. Mach-Zehnder microinterferometers in a RTP crystal, 5 MeV N^{3+} microbeam, fluence = $5 \cdot 10^{14}$ - $8 \cdot 10^{15}$ ions/cm².
5. Single channel waveguides in an Yb: KYW crystal, 5 MeV N^{3+} microbeam, fluence = $5 \cdot 10^{14}$ - $8 \cdot 10^{15}$ ions/cm².
6. Mach-Zehnder microinterferometers with grating couplers at both ends in an Yb: KYW crystal, 5 MeV N^{3+} microbeam, fluence = $5 \cdot 10^{14}$ - $8 \cdot 10^{15}$ ions/cm².
7. Single channel waveguides in a KTP crystal, 5 MeV N^{3+} microbeam, fluence = $5 \cdot 10^{14}$ - $8 \cdot 10^{15}$ ions/cm².
8. Single channel waveguides in a KTP crystal, 10.5 MeV N^{4+} microbeam, fluence = $1.25 \cdot 10^{14}$ - $4 \cdot 10^{15}$ ions/cm². Side-walled channel waveguides were also fabricated.
9. Mach-Zehnder microinterferometers in a KTP crystal, 10.5 MeV N^{4+} microbeam, fluence = $6.25 \cdot 10^{13}$ - $4 \cdot 10^{15}$ ions/cm². Side-walled Mach-Zehnder microinterferometers were also fabricated.
10. Single channel waveguides in a RTP crystal, 10.5 MeV N^{4+} microbeam, fluence = $2.5 \cdot 10^{14}$ - $4 \cdot 10^{15}$ ions/cm². Side-walled channel waveguides were also fabricated.
11. Mach-Zehnder microinterferometers in a RTP crystal, 10.5 MeV N^{4+} microbeam, fluence = $1.25 \cdot 10^{14}$ - $2 \cdot 10^{15}$ ions/cm². Side-walled Mach-Zehnder microinterferometers were also fabricated.
12. Single channel waveguides in an Yb: KYW crystal, 10.5 MeV N^{3+} microbeam, fluence = $2 \cdot 10^{14}$ - $4 \cdot 10^{15}$ ions/cm². Side-walled channel waveguides and side-walled channel waveguides were also fabricated.

Tests completed

1. All the structures were measured with a confocal microscope to determine the profiles of the surface relief structures created.
2. Micro-Raman measurements, performed at the polished edges of the channel waveguides, revealed their depth profile.
3. Measurements showed that some of the as implanted single channel waveguides and Mach-Zehnder microinterferometers written in an Yb: KYW crystal had low propagation losses at a wavelength of 1450 nm.

3. Microwells

We tried to fabricate microwell arrays for biochemical sensors in a polymer (Zeonor) and a special glass (Gold Seal).

Experiments completed

1. Zeonor Polymer

Microwells were written in a Zeonor sample with 10.5 MeV N^{3+} microbeam, at fluences = $1 \cdot 10^{13}$ - $1 \cdot 10^{14}$ ions/cm².

2. Gold Seal Glass

Microwells were written in a Gold Seal sample with 10.5 MeV N^{3+} microbeam, at fluences = $1 \cdot 10^{14}$ - $4 \cdot 10^{14}$ ions/cm².

Tests completed

Preliminary AFM tests showed that some microwell groups in the Zeonor sample are good for use in sensors. The experiment has to be repeated with the same materials so that optimum geometrical parameters and fluences could be determined.

4. Planar waveguides implanted with Ag ions

Experiments completed

Planar optical waveguides were implanted in KTP and RTP crystals, using 11 MeV Ag^{3+} ions. Eight waveguides were fabricated in the two samples, with the fluences from $3 \cdot 10^{15}$ ions/cm² to $1 \cdot 10^{14}$ ions/cm².

Tests completed

Spectral ellipsometric tests of all the planar waveguides were performed. Even the raw ellipsometric spectra showed that the refractive index modulation induced in the samples by the Ag^{3+} ion implantation was rather low. Consequently, we plan to repeat this experiment with higher fluences up to $5 \cdot 10^{16}$ ions/cm².

Ion beam modification of carbon allotropes

Laboratory of Tandetron

Petr Malinsky

Proposal ID

352

Report regarding proposal “Ion beam modification of carbon allotropes”

P. Malinský, A. Macková, M. Cutroneo, V. Hnatowicz, K. Szökölóvá, M. Boháčová,
R. Böttger, J. Luxa, Z. Sofer

The proposal was denoted to the study of light and heavy ion irradiation of graphene oxide (GO) with the aim of GO reducing to the graphene like structure and simultaneously change its electrical properties. The GO is a carbon allotrope that is highly studied due to its excellent properties and potential in the field of nano-composites, solar cells, super-capacitors, micro- and nano-electronic [1–3]. GO is the single mono-molecular layer of graphene with various oxygen containing functionalities at edges and basal planes, due to the carbon atoms in the GO structure having a mixture of sp^2 and sp^3 hybridization. [2,4] Non-modified GO is an insulator due to the disruption in the sp^2 bonded graphitic structures and can be converted to semi- conductivity or conductivity state by changing the sp^2/sp^3 ratio. [5,6].

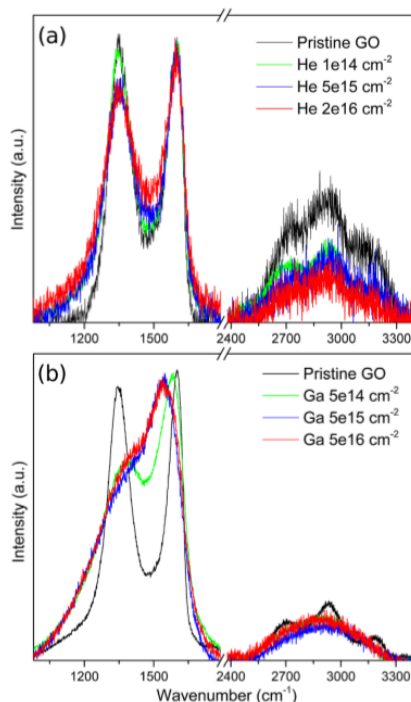


Figure 1: Raman spectra of GO film irradiated using various fluencies of 500 keV He ions (up) and Ga ions (down) compared to pristine GO film.

The GO foils were irradiated using He, H, Au and Ga ions with energies in the range from 500 keV to 5.1 MeV to the different fluencies and subsequently analyzed by ERDA, RBS, XPS, SEM and Raman spectroscopy to characterize the elemental composition, elemental depth profiles, subsurface chemical bonds and chemical composition modification as well as the surface morphology. The electrical properties of pristine and irradiated GO foils were measured by the standard two points method.

It can be concluded that the irradiation using heavy ions (Au, Ga) leads to strong changes in GO film structure and to the significant elemental composition modification, deoxygenation and dehydrogenation, which are connected to significant energy transfer from the heavy ions to the atoms in irradiated material via mostly non-elastic nuclear stopping. The irradiation using heavier ions causes the GO amorphization connected with disruption of the carbon bonds, with atom displacements, and also creation of new non-benzene carbon structures and vacancy types of defects. Contrary, irradiation using light ions (He, H), with dominant elastic electronic stopping, results in lower degree of GO deoxygenation and less pronounced structural changes when comparing with ions with higher mass. Moreover, the light ions irradiation leads to the formation of sp^2 graphene domains.

The irradiation with heavy as well as light ion species reduces the oxygen chemical bonds, generates new carbon bonds and causes the conductivity enhancement that is in accordance with observed compositional and structural modifications. The recovery of electrical conductivity is more pronounced for the light ions due the restoration of graphene like structure and can be concluded that GO irradiation using light ions provides relatively simple method of producing reduced graphene oxide with enhanced electrical conductivity.

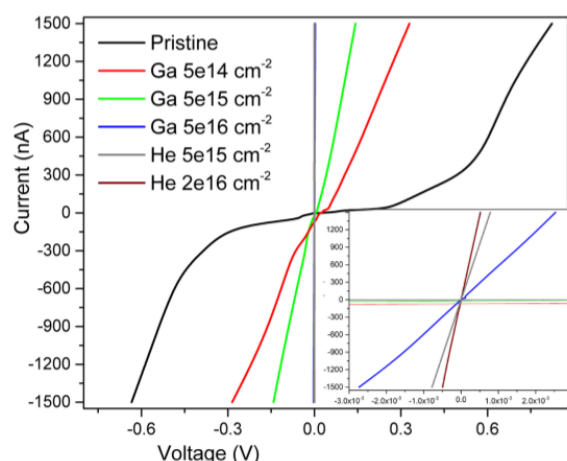


Figure 2: The I-V characteristic curves of pristine GO film and GO film irradiated with 500 keV He and Ga ions at various fluencies. The detailed I-V characteristic for voltage range from 3.0×10^{-3} to 3.0×10^{-3} V is shown in inset figure

- [1] P. Gulia, et al., AIP Conf. Proc. 2017, 1832, 140023.
- [2] D. R. Dreyer, et al., Chem. Soc. Rev. 2010, 39, 228.
- [3] V. Mazánek, et al., Nanoscale 2015, 7, 13646.
- [4] O. C. Compton, Small 2010, 6, 11.
- [5] S. Park, Carbon 2009, 50, 217.
- [6] Ch. Punckt, et al., Appl. Phys. Lett. 2013, 102, 023114.

Residual stress measurement in rotary swaged composites

Neutron Physics Laboratory - Neutron diffraction

Lenka Kuncicka

Proposal ID

353

Final report to the proposal „Residual stress measurement in rotary swaged composites “

L. Kunčická, Regional Materials Science and Technology Centre, VŠB TU Ostrava, CZ

P. Strunz, Ch. Hervoches Nuclear Physics Institute, ASCR, Řež 130, Husinec, CZ

The aim of this project was to investigate possible presence of residual stress in composite materials rotary swaged under various processing conditions.

In order to determine residual stresses, the strains were calculated according to peak positions in three measured directions, hoop (x), radial (y), and axial (z). The peak position changes in the axial direction were rather smooth within the whole measured range for both the samples. However, the hoop and radial directions peak positions changed significantly in several locations throughout the scanned area. These changes point to the presence of residual stresses in the vicinity of the Al-Cu interfaces.

Calculations of strains according to Eq. (1) [1] showed lattice expansion through the majority of sample cross section in the axial direction, and lattice shrinkage through the majority of sample cross section in the radial and hoop directions for both.

$$\varepsilon_{hkl} = \frac{d_{hkl} - d_{0,hkl}}{d_{0,hkl}} = \frac{\Delta d_{hkl}}{d_{0,hkl}} \quad (1)$$

The final residual stress values calculated according to Eq. (2) [1] are depicted in the dependence in Fig. 1. As can be seen in the Figure, the values of the residual stress for the 10 mm sample oscillated from approx. 150 MPa to -150 MPa along its cross-section. The lowest variations (variation range of 43) were measured in the axial direction, which was perpendicular to the axis of the swaged composite. On the other hand, the step changes in the values in the radial and hoop directions (variation ranges of 65 and 76, respectively) point to residual stress at the Al/Cu interfaces.

$$\sigma_x = \frac{E_{hkl}}{(1-2\nu_{hkl})(1+\nu_{hkl})} [(1 + \nu_{hkl})\varepsilon_x^{hkl} + \nu_{hkl}(\varepsilon_y^{hkl} + \varepsilon_z^{hkl})] \quad (2)$$

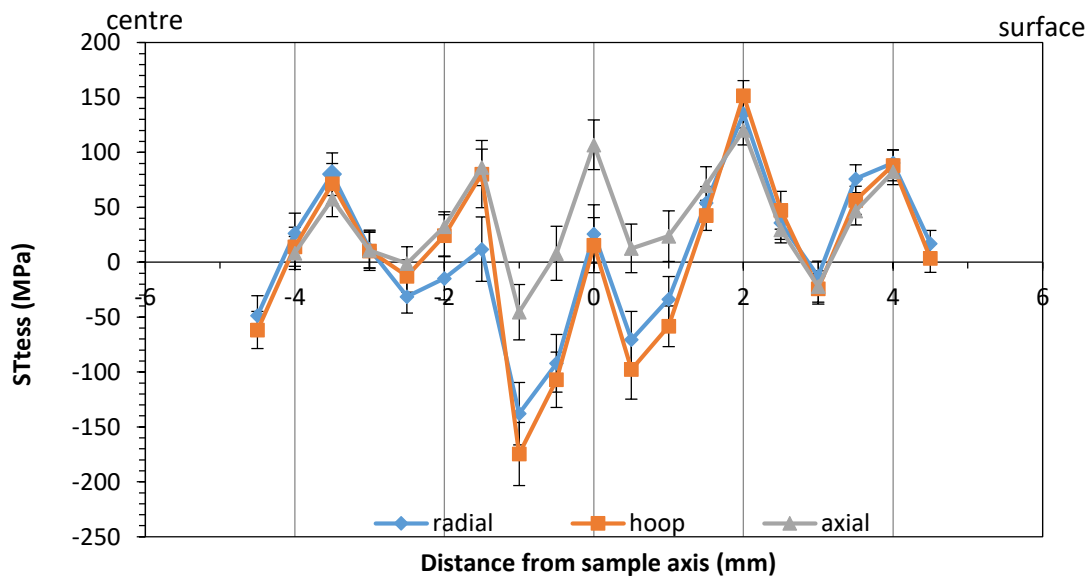


Figure 1. Residual stress within rotary swaged Al-Cu composite, 10 mm diameter.

References

[1] M.T. Hutchings, Introduction to the characterization of residual stress by neutron diffraction, Taylor & Francis, 2005.

Determination the boron distribution in the boron-doped nanocrystalline diamond layers

Neutron Physics Laboratory - Nuclear analytical methods with neutrons

Petr Ashcheulov

Proposal ID

290

Determination of the boron distribution in the boron-doped nanocrystalline diamond layers

Petr Ashcheulov

Institute of Physics, Academy of Sciences of the Czech Republic, v.v.i, Na Slovance 2, 182 21 Prague, Czech Republic

Microwave plasma enhanced chemical vapour deposition system with linear antenna delivery (MW-LA-PECVD) is a novel technique for the preparation of a large area (currently 30cm²) diamond coatings. MW-LA-PECVD technique allows deposition of nanocrystalline diamond (NCD) layer on a variety of substrates due to its capability of low temperature diamond growth (down to 250°C). It is possible to obtain electrically conductive NCD films by introducing a boron precursor during the growth process. However, the conductivity values of the NCD films obtained in the MW-LA-PECVD reactor are much lower compared to NCD layers obtained by classical MW PECVD technique [1,2]. This effect is partially attributed to the incorporation of boron atoms into the diamond grains within the NCD film and precipitation of boron between diamond grains. Thus, to realize a full potential of coatings obtained by the MW-LA-PECVD technique boron incorporation into the NCD films must be studied in details.

Here, we have investigated the boron concentration profile in the NCD films by the NDP technique to access the boron doping efficiency. Recently, it has been reported that the addition of CO₂ is crucial to suppress the concurrent formation of SiC during NCD growth process [3]. NCD layers were grown in the optimized gas mixture (boron-to-carbon ratio of 15000 ppm) of H₂/CH₄/TMB with added CO₂ gas and results were compared to layers obtained with H₂/CH₄/TMB gas admixture with no CO₂ addition (Figure 1).

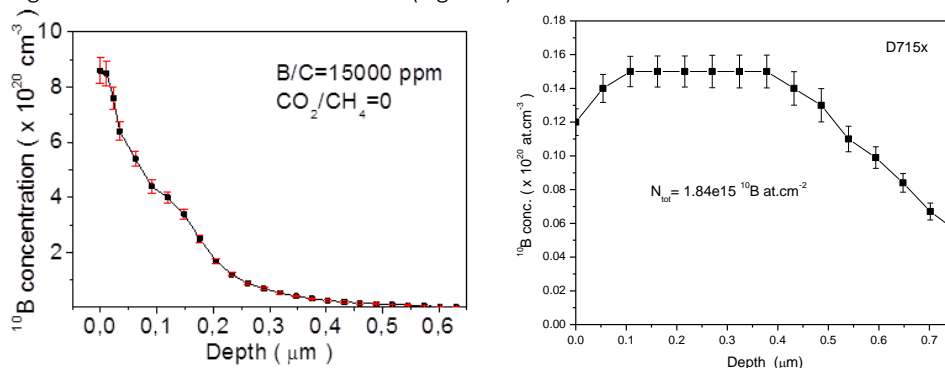


Figure 1. NDP results of samples prepared at 15000 ppm B/C ratio without CO₂ (left) and with CO₂ addition sufficient to suppress SiC formation(right)

As it seen from Figure 1, the measured boron concentration in the layers obtained without CO₂ addition is much higher than in the layer prepared with CO₂ added, $\sim 4 \times 10^{20}$ at/cm³ (at 100 nm depth) and $\sim 1.5 \times 10^{19}$ at/cm³ (at 150 nm depth), respectively. Obtained results suggest that the incorporation of boron atoms inside the NCD film has been suppressed by the addition of CO₂. Therefore, further optimization of the boron-doping process parameters (CO₂/CH₄, B/O and B/C ratios, deposition temperature) if the MW-LA-PECVD system is necessary to tune the boron incorporation in the films ensuring the suppression of the concurrent SiC formation.

References:

- [1] A. Taylor, L. Fekete, P. Hubík, A. Jäger, P. Janíček, V. Mortet, J. Mistřík, and J. Vacík, *Diam. Relat. Mater.*, **47**, 27 (2014)
- [2] P. Ashcheulov, J. Šebera, A. Kovalenko, V. Petrák, F. Fendrych, M. Nesládek, A. Taylor, Z. Vlčková Živcová, O. Frank, L. Kavan, M. Dračinský, P. Hubík, Jiří Vacík, I. Kraus, and I. Kratochvílová, "Conductivity of boron-doped polycrystalline diamond films: influence of specific boron defects", *The European Physical Journal B*, (2013) 86:443
- [3] A. Taylor, P. Ashcheulov, M. Čada, L. Fekete, P. Hubík, L. Klimša, J. Olejníček, Z. Remeš, I. Jirka, P. Janíček, E. Bedel-Pereira, J. Kopeček, J. Mistřík, V. Mortet, Effect of plasma composition on nanocrystalline diamond layers deposited by a microwave linear antenna plasma-enhanced chemical vapour deposition system, *phys. status solidi a* **212** (2015) 2418 - 2423.

Magnetism in mixed Fe-Mn oxyborates

Neutron Physics Laboratory - Neutron diffraction

Christine Martin

Proposal ID

292

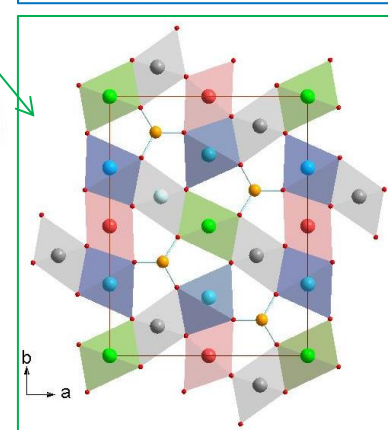
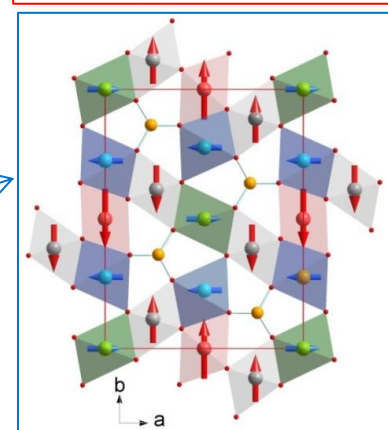
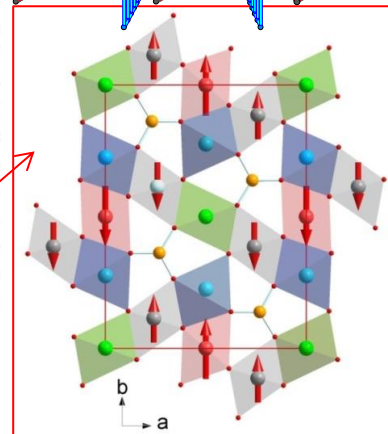
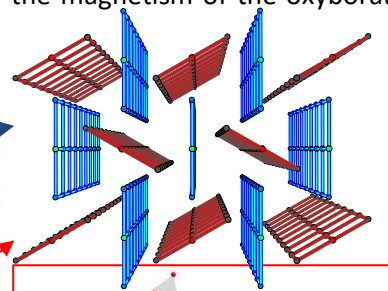
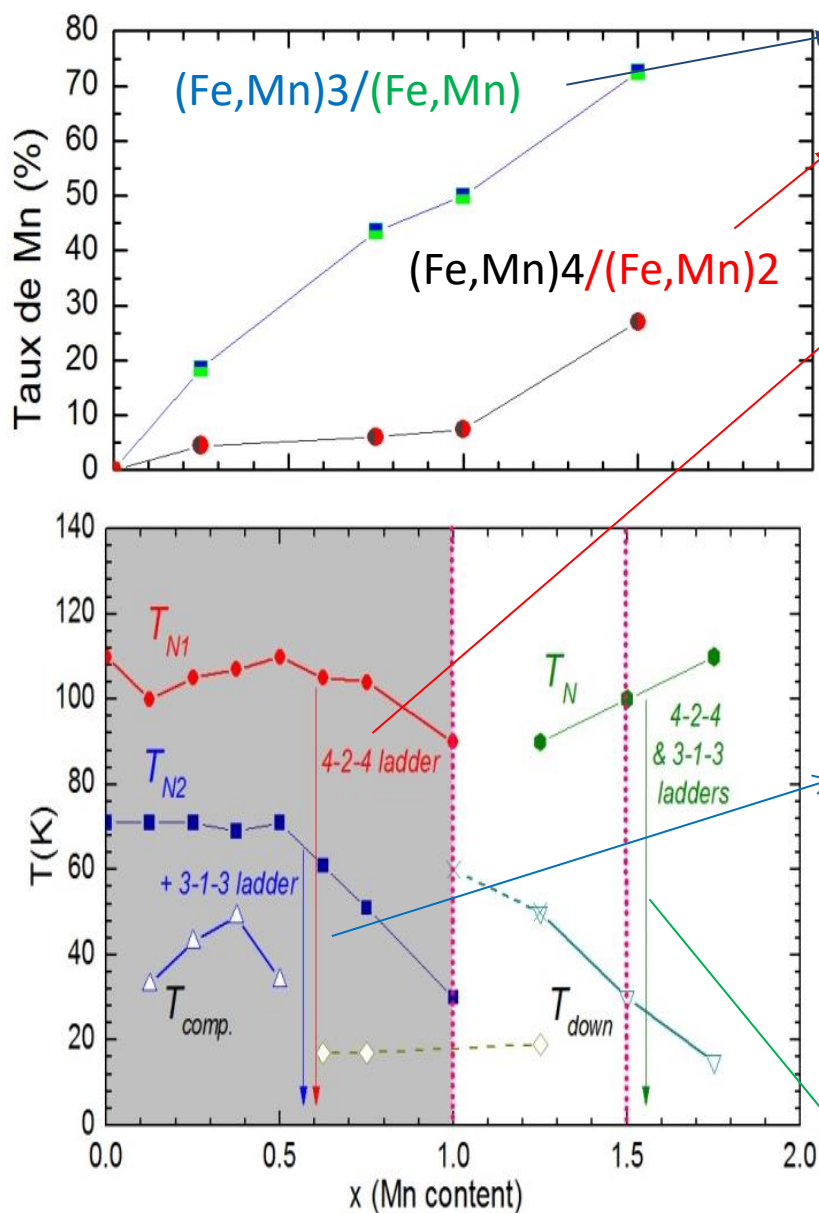
Magnetism in mixed Fe-Mn oxyborates

C. Martin, CRISMAT, Caen, France

F. Damay, LLB-Saclay, Gif-sur-Yvette, France

P. Beran, Nuc. Physics Inst., Rez, Czech Republic

Two samples belonging to the $\text{Fe}_{3-x}\text{Mn}_x\text{BO}_5$ series ($x=1$ and 1.5) were first studied on Meredit at RT and 10K. The new meredit-NPD data deals with two other compositions ($x=0.25$ and 0.75) at several temperatures. The refinement of the structures (including determination of Mn/Fe distribution) coupled with the study of magnetic behaviours (magnetic structures and evolution vs temperature) allow the establishment of a $a(T,x)$ magnetic phase diagram. As summarized in the following figures, the amount of Mn does not influence the structure itself but the iron and manganese species distribution on the cationic sub-lattice has a strong impact on the magnetism of the oxyborates. A publication is in preparation.



$^{197\text{(m)}}\text{Hg}$ production via the $^{197}\text{Au}(\text{d},2\text{n})^{197}\text{Hg}$ reaction

Laboratory of Cyclotron and Fast Neutron Generators

Martin Walther

Proposal ID

293

Report regarding proposal “ $^{197\text{m}}\text{Hg}$ production via the $^{197}\text{Au}(\text{d},2\text{n})$ reaction”

M. Walther, Helmholtz-Zentrum Dresden-Rossendorf, Institute of Radiopharmaceutical Cancer Research, Germany

O. Lebeda, Nuclear Physics Institute of the CAS, Řež, Czech Republic

The significant larger cross-sections reported for $^{197}\text{Au}(\text{d},2\text{n})^{197\text{m}}\text{Hg}$ reaction [1] compared to the proton induced $^{197}\text{Au}(\text{p},\text{n})^{197\text{m}}\text{Hg}$ reaction could be unambiguously confirmed. With a deuteron beam energy of 16 MeV more than four times higher yields of the metastable no-carrier-added $^{197\text{m}}\text{Hg}$ radionuclide were accessible using comparable beam intensity. Thus it is shown clearly that the limiting factor of the low yield proton based reaction can be overcome using this alternative nuclear reaction. The additional advantage of the higher ratio of the preferable short-lived $^{197\text{m}}\text{Hg}$ radionuclide (ratio $^{197\text{m}}\text{Hg}/^{197}\text{Hg}$: $\sim 1.7/1$) compared to the proton accessible product ($\sim 1/1$) [2] also increases the attractiveness of this production route for potential theranostic application.

TABLE 1. Hg and Au isotopes after proton or **deuteron** irradiation of gold in the target solution and product solution after separation using LN resin

	E particle	t _{irr}	I _T	m _{Au}	A _{EOB} [MBq] in target solution				A _{EOB} [MBq] in product				yield
No	[min]	[μA]	[mg]		^{197}Hg	$^{197\text{m}}\text{Hg}$	^{196}Au	^{198}Au	^{197}Hg	$^{197\text{m}}\text{Hg}$	^{196}Au	^{198}Au	
1	10 MeV p	120	25	185	81	89	0.004	0.099	75	83	<0.001	<0.001	93%
2	12 MeV p	145	20	186	145	160	0.021	0.184	136	150	<0.001	0.002	94%
3	16 MeV d	120	11	186	272	462	7	156	248	420	<0.003	<0.003	91%
4	16 MeV d	150	10	186	332	574	9	193	315	545	<0.006	<0.003	95%

Beside the higher product yield during deuteron irradiation, also the significant formation of gold isotopes as undesired side products must be considered in the workup procedure. Therefore, according to the high requirements, a new resin based Hg/Au separation method was developed. So called LN resin (LaNthanides)^{3,4}, was successfully tested for this application. The obtained promising results in radionuclide production together with results of labeling - and biological experiments will be published as soon as possible in the current year in peer-reviewed international journals.

References

- [1] F. Tárkányi, F. Ditrói, A. Hermanne, S. Takács, B. Király, H. Yamazaki, M. Baba, A. Mohammadi, A.V. Ignatyuk, Nucl. Instrum. Methods Phys. Res., Sect. B 269, pp. 1389–1400, 2011.
- [2] M. Walther, S. Preusche, S. Bartel, G. Wunderlich, R. Freudenberg, J. Steinbach, H.-J. Pietzsch: Appl. Radiat. Isot. 97, pp. 177–181, 2015
- [3] E. P. Horwitz, C. A. Bloomquist, Journal of Inorganic Nuclear Chemistry, 37, pp. 425–434 1975.
- [4] D. McAlister, E. P. Horwitz, Solvent Extraction and Ion Exchange, 25, (6), pp. 757–769 2007.

Structural and optical properties in yttria-stabilized zirconia modified by Si-implanted ions

Laboratory of Tandetron

Romana Mikšová

Proposal ID

357

Report regarding proposal “Structural and optical properties in yttria-stabilized zirconia modified by Si-implanted ions.”

R. Mikšová, A. Macková, A. Jagerová, P. Malinský, Nucl. Physics Inst., Rez, Czech Republic
 Z. Sofer, Department of Inorganic Chemistry, Institute of Chemical Technology, Prague, Czech Republic
 V. Holý, Department of Condensed Matter, Faculty of Mathematics and Physics, Prague, Czech Republic
 CEITEC at Masaryk University, Brno, Czech Republic

In our results, we observed Zr signal increase in the appropriate depth of Si implanted in yttria-stabilized zirconia (YSZ) with the enhanced ion fluence in Figure 1a simultaneously with the shift of the damaged region closer to the surface. YSZ implanted with medium-energy heavy ions exhibits the accumulation of damage with the increasing ion implantation fluence (see Figure 1b). The multi-damage step was shown.

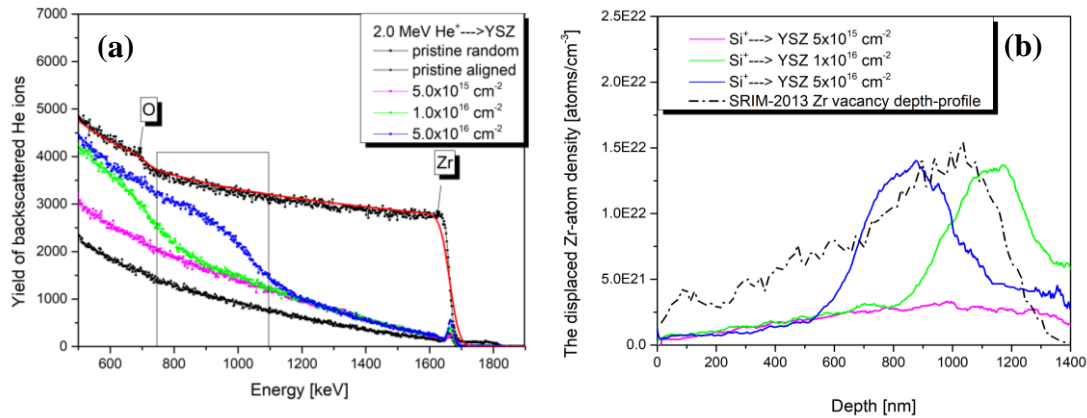


Figure 1. The RBS-C measurement of random and aligned spectra of pristine and implanted YSZ at ion fluence of 5×10^{15} - $5 \times 10^{16} \text{ cm}^{-2}$ measured by energy 2.0 MeV (a) using He⁺ ions. The depth profile of the displaced Zr-atom density in YSZ implanted by 2.0 MeV Si⁺ ions at ion fluences of 5×10^{15} - $5 \times 10^{16} \text{ cm}^{-2}$ extracted from the RBS-C spectra (b).

The XRD measurement indicates specific features as the positive vertical strain which is induced by the interstitial-type defects during ion implantation; the damaged layer is vertically expanded (Figure 2b). These facts agree with the RBS-C measurement where the axial-channel narrowing as a function of the increased ion-implantation fluence was observed. The axial-channel narrowing is a consequence of the gradually enhanced vertical expansion in YSZ (Figure 2a). The Raman spectroscopy confirms changes in the Raman spectra (peak broadening and peak shift) connected with the presence of the strain.

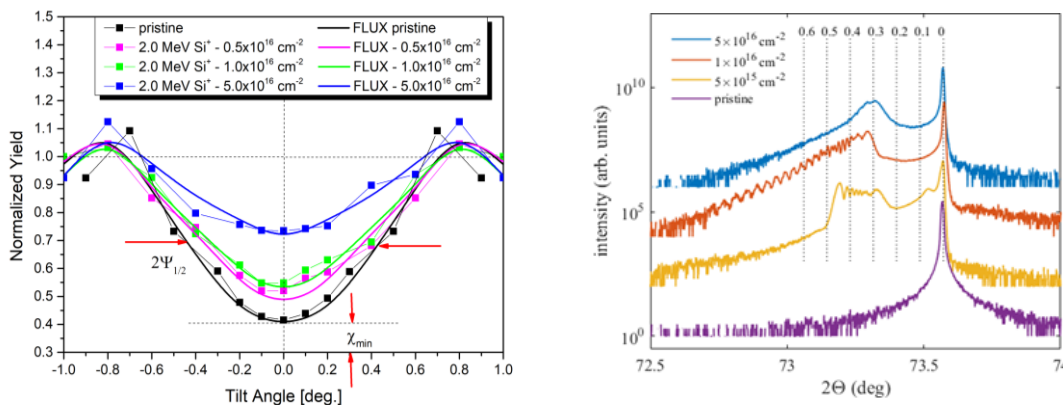


Figure 2. The angular (Zr sublattice) scans using 2.0 MeV He⁺ ions penetrating (100) YSZ implanted with 2 MeV Si⁺ ions at the fluences of 5×10^{15} - $5 \times 10^{16} \text{ cm}^{-2}$. Measured symmetric $2\Theta/\Omega$ scans of a pristine sample and samples implanted with various doses (parameter of the curves).

The results were sent into NIMB.

INTERNAL: RBS analysis of rough samples

Laboratory of Tandetron

Petr Malinsky

Proposal ID

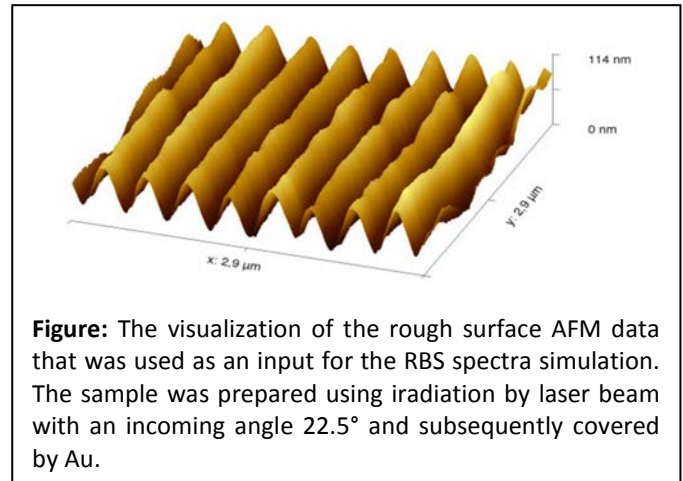
166

Report regarding proposal “RBS analysis of rough samples”

Petr Malinský, Jakub Siegel, Vladimir Hnatowicz, Anna Macková, Václav Švorčík

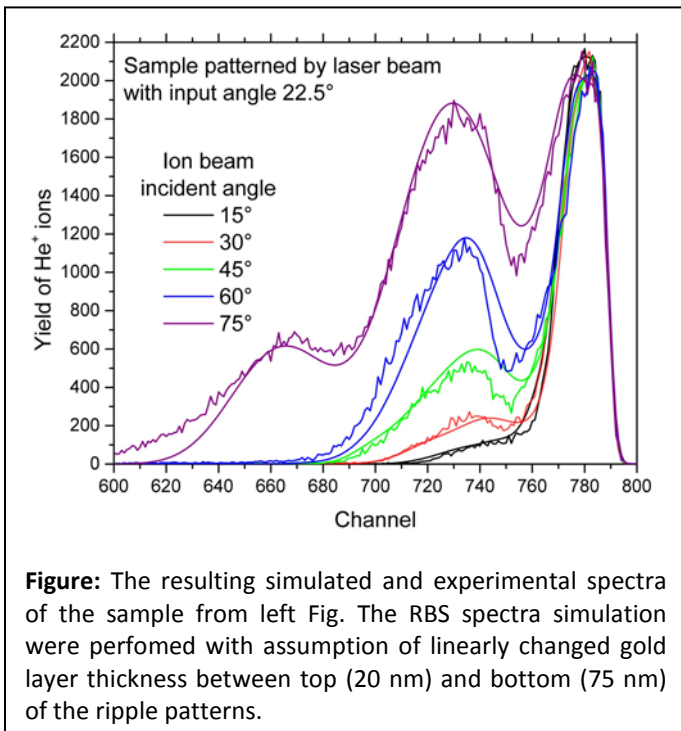
The proposal was devoted to the study of surface roughness implementation to the analysis of Rutherford Backscattering Spectroscopy (RBS) energy spectra. The surface roughness of analysed samples deteriorates the RBS spectra and can make their interpretation more difficult, ambiguous and in some cases non-evaluable.

A code for the simulation of common RBS spectra implementing surface roughness effects has been written and the feasibility of the code has been demonstrated on real samples with regular roughness, which was determined by AFM method. The spectra, simulated for different ion beam incidence angles, were compared to the experimental ones measured with 2.0 MeV He^+ ions in the Tandetrón CANAM laboratory of NPI of ASCR, v.v.i. The resulting RBS spectrum was calculated as a sum of the many particular spectra obtained for randomly chosen particle trajectories over sample 3D landscape. The used samples were prepared by the sputtering of a 35-nm-thick gold layer on the surface of the periodically patterned PET substrate.



The RBS spectra measured at glancing angles exhibited a more complex gold signal comprising the main peak and low-energy components corresponding to ion scattering from gold layers on the neighbouring ripples. The relative

intensity of the low-energy components was an increasing function of the ion-beam incidence angle. For lower ion beam incident angles the measured gold signal was well reproduced by computer simulation but for larger incident angles the evolution of the gold signal was reproduced just qualitatively. Therefore, the effects of varying gold layer thickness and gold layer inhomogeneity on simulated spectra were examined and it was shown that the simulation with assumption of linearly varying gold layer thickness reproduced the experimental RBS spectra fairly. The next result of the experiment was that required simulated spectrum can be obtained already after summing of about 300 randomly generated particular spectra. Finally we can say that the data of surface roughness obtained from AFM analysis can be used for the



simulation of RBS spectra and that the RBS measurements accomplished at glancing angle may indicate the presence of a periodic structure on the sample surface.

References

- [1] P. Malinský, V. Hnatowicz, A. Macková, Nucl. Instrum. Meth. B 371 (2016) 101-105
- [2] M. Mayer, P. Malinský, F. Schiettekatte, Z. Zolnai, Nucl. Instrum. Meth. B 385 (2016) 65-73
- [3] P. Malinský, J. Siegel, V. Hnatowicz, A. Macková, V. Švorčík, will be published in Nucl. Instrum. Meth. B

Neutron scattering studies of nanostructured cemented carbides

Neutron Physics Laboratory - Neutron diffraction

Ahmet Bahadir Yildiz

Proposal ID

358

Experimental report

Proposal: Neutron scattering studies of nanostructured cemented carbides (ID: 358)

Ahmet Bahadir Yildiz, Peter Hedström: KTH Royal Institute of Technology, Stockholm

Vasyl Ryukhtin: Nuclear Physics Institute, Rez

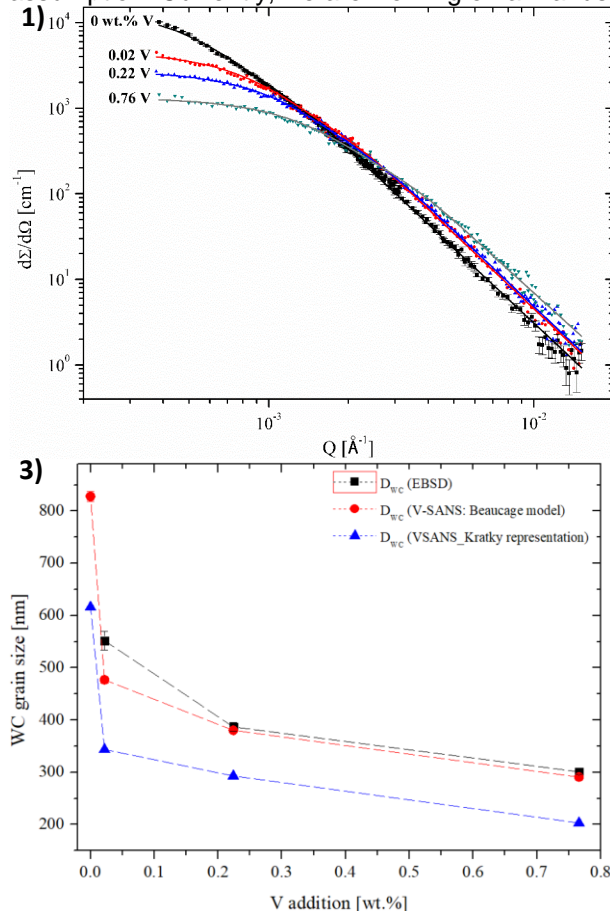
Fine-grained cemented carbides are demanded in cutting applications requiring higher hardness. During our beamtime on the MAUD, we performed ex-situ V-SANS experiments for the investigation of WC grain growth in WC-Co-V_x system as a function of V addition.

V-SANS data were acquired at three different instrumental resolutions. To eliminate the magnetic scattering contribution, specimens were placed between two Neodymium magnets perpendicular to the neutron beam. The measured V-SANS data were corrected for electronic noise background using Cd, normalized by the transmission and scaled to absolute units $d\Sigma/d\Omega$ [cm⁻¹].

Fig. 1 shows the evolution of nuclear V-SANS intensities as a function of V addition. Upon V addition, the scattering intensity decreased at low-Q region, and increased at high-Q region. This development trend in scattering curves gave initial insight to the refinement in WC grain size. In order to calculate radius of gyration, R_g , we used Beaucage model [1] (solid lines in Fig. 1) and Kratky representation [2] (**Fig. 2**), i.e. $d\Sigma/d\Omega \times Q^2$ versus Q plots. Assuming spherical WC grains, the size of WC grains, D_{WC} , can be calculated

$$\text{by: } D_{WC} = 2 * \sqrt{\frac{5}{3}} R_g$$

Fig. 3 shows the size evolution of WC grains together with the average grain size measured by EBSD. Consistency in the evolution trend was found in the grain size values determined by V-SANS and EBSD. Kratky plots gave significantly smaller D_{WC} than that of Beaucage model fit. Good agreement was found between D_{WC} values calculated by EBSD and V-SANS using Beaucage model and spherical grain assumption. Currently, we are working on a manuscript.



Figures The evolution of V-SANS curves log-log scale (1) and Kratky plots (2) as a function of V addition in liquid-phase sintered WC-Co-V_x (x=0 to 0.765 wt.% V) cemented carbides. The solid lines in Fig. 1 correspond to Beaucage model fit. The average WC grain size calculated for spherical WC grains plotted together with EBSD results (3).

References

- [1] G. Beaucage, J. Appl. Crystallogr. 28 (n.d.) 717–728.
- [2] A. Deschamps, F. De Geuser, J. Appl. Crystallogr. 44 (2011) 343–352.

Optical devices by focused MeV ions

Laboratory of Tandetron

István Rajta

Proposal ID

231

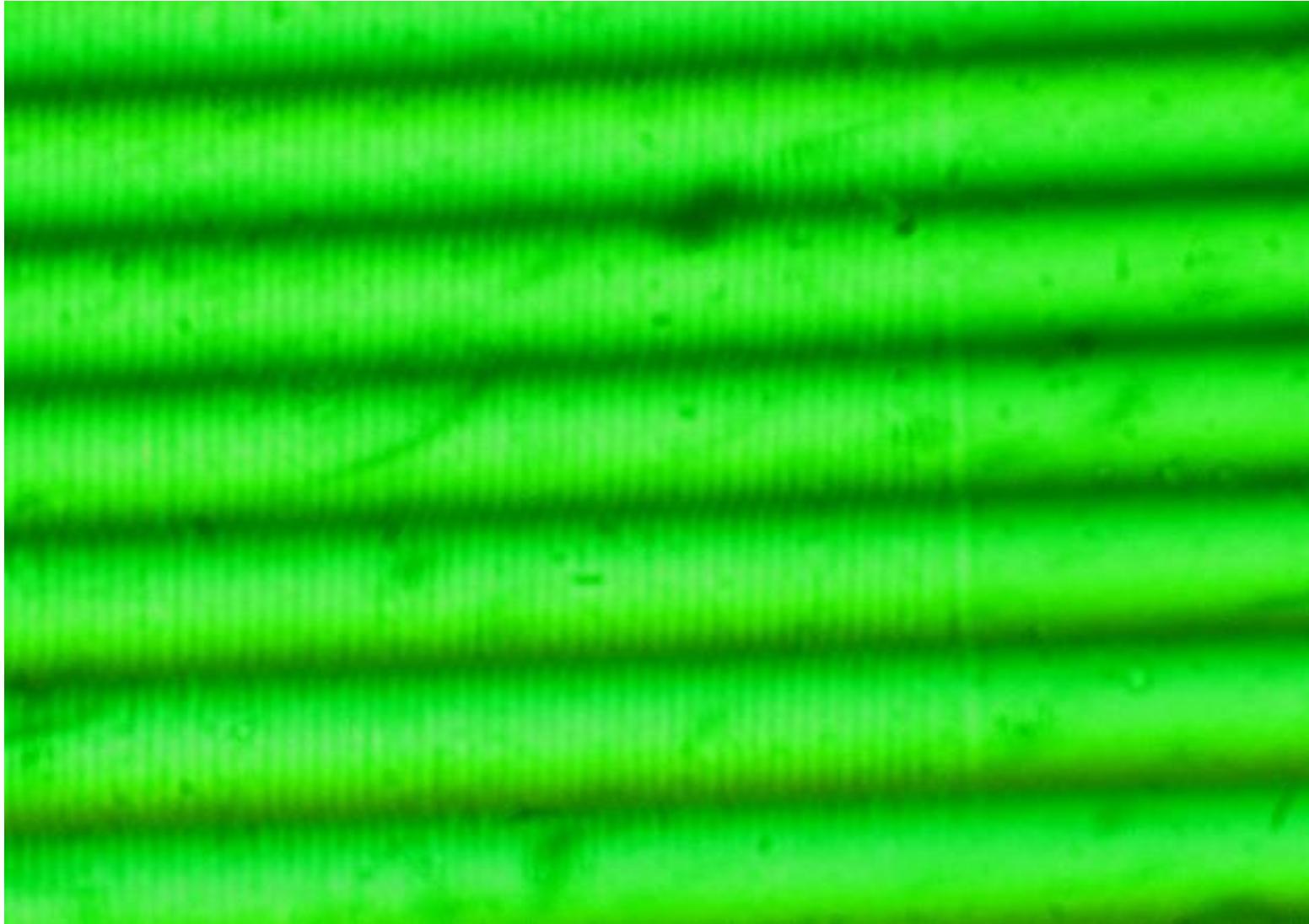


Figure 1. Transmission interference microscopic image of a grating with $\Lambda = 8 \mu\text{m}$, written by a $5 \text{ MeV } \text{N}^{4+}$ microbeam at a fluence of $5 \times 10^{15} \text{ ions/cm}^2$ in an Er:LiNbO_3 crystal.

Simulation of alpha radiation-induced alterations in uraniferous fossil organic matter.

Laboratory of Tandetron

Vladimir Strunga

Proposal ID

360

Report regarding proposal "Simulation of alpha radiation-induced alterations in uraniferous fossil organic matter"

V. Strunga, V. Havránek, J. Mizera, Nucl. Physics Inst., Rez, Czech Republic

V. Goliáš, Inst. of Geochem., Mineral. and Min. Res., Charles University, Prague.

Polished sections of Baltic amber were prepared in two series of three samples each. Irradiation was carried on Tandetron accelerator at Nuclear Physics Institute, ASCR, Řež using a 4.8 MeV alpha-particle beam at three various doses, 5E13, 2E14, and 8E14 α/cm^2 , respectively. Samples were subjected to IR microspectroscopy (ATR-FTIR) afterward.

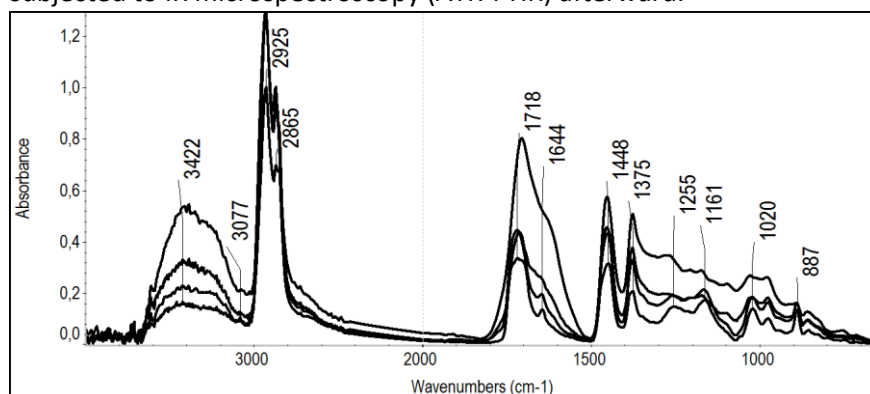


Fig. 1 Infrared spectra of analyzed ambers including non-irradiated sample (analysis by Vladimír Machovič).

Spectra exhibit broadening of O-H band at 3422 cm^{-1} as well as a decrease in double bond band intensities at 3100-3000, 1644 and 887 cm^{-1} . There is also distinguishable vanishing of the Baltic amber characteristic feature, so-called 'Baltic shoulder' assigned to the absorption of succinic acid ester bonds of polyester-like structures between 1255 and 1161 cm^{-1} .

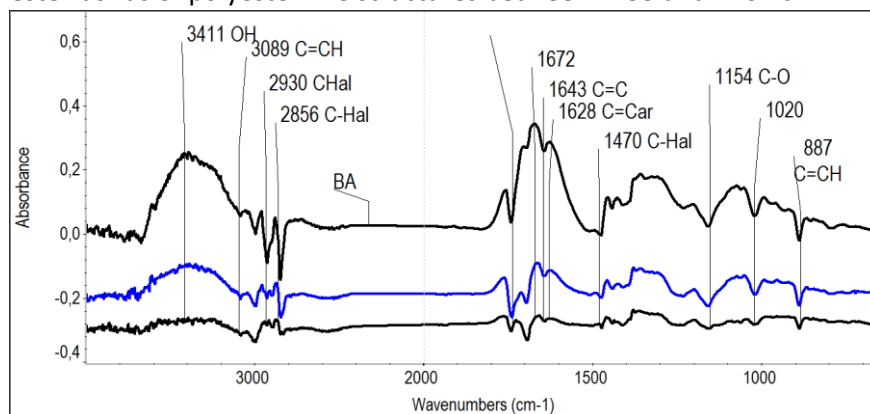


Fig. 2 Differential spectra obtained by subtraction of non-irradiated sample spectral values from irradiated ones (analysis by Vladimír Machovič).

Differential spectra reveal a considerable decrease of C-H band intensities at 2930, 2856, 1470 cm^{-1} , O-H band intensity increase at 3411 cm^{-1} , 1705 cm^{-1} , COOH band at 1672 cm^{-1} , highly conjugated C=O and aromatic C=C band at 1628 cm^{-1} .

Reference

Havelcová, M., Machovič, V., Linhartová, M. Lapčák, L., Přichystal, A., Dvořák, Z. (2016)

Vibrational spectroscopy with chromatographic methods in molecular analyses of Moravian amber samples (Czech Republic). *Microchemical Journal*, 128, 153-160.

Radiation hardness investigation of APD for PSD detector readout at CBM

Laboratory of Cyclotron and Fast Neutron Generators

Vasily Mikhaylov

Proposal ID

169

Report regarding proposal "Radiation hardness investigation of APD for PSD detector readout at CBM"

V. Mikhaylov, V. Kushpil, O. Svoboda, A. Kugler, Nucl. Physics Inst., Rez, Czech Republic

Radiation hardness is a key requirement for the Avalanche PhotoDiodes (APDs) for the future FAIR CBM Projectile Spectator Detector (PSD). APDs will be used for the light readout from the detector scintillators. APDs will be located at the end of the PSD and are required to withstand the total neutron fluence up to $3\text{E}12 \text{ n/cm}^2$ for the one year of the experiment operation according to FLUKA simulation.

During the proposed experiments we have studied the behavior of APDs produced by Hamamatsu, Ketek, Sensl and Zecotek after the irradiation. On figure 1 one can see example of huge increase in dark currents after the irradiation for Ketek PM-3350 and Hamamatsu S12572-010P APDs [1]. It imposes the requirement for the APDs electronics to be able to supply currents up to 1mA.

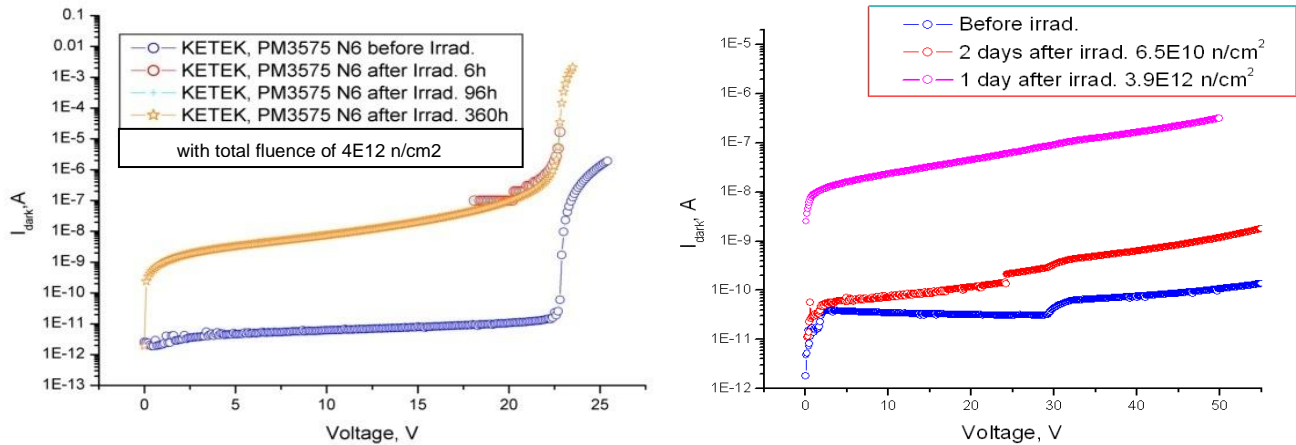


Fig. 1. Dependences of dark current on the reverse voltage for various APDs before and after irradiation with total neutron fluence indicated. Left: Ketek, right: Hamamatsu.

Using developed dedicated setup in our lab, we also studied the internal characteristics of the APDs. With help of Capacitance-Voltage profiling we have analyzed the profile of impurities produced in the APD depletion region as shown on figure 2 [2]. The achieved data is still under evaluation, in future it can be useful for development of readout electronics and improvement of detector technology.

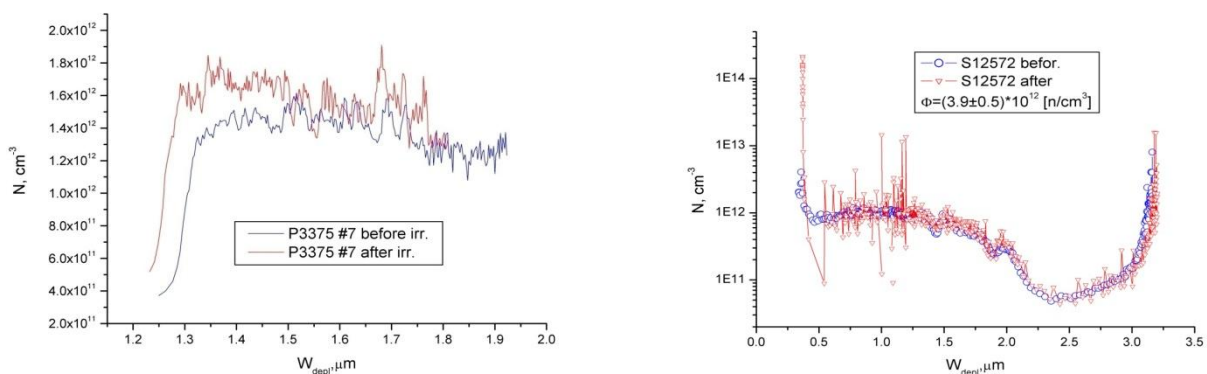


Fig. 2. Distribution of impurities produced in the depletion region on the depletion region width before and after irradiation with total neutron fluence of about $4\text{E}12 \text{ n/cm}^2$. Left: Ketek, right: Hamamatsu.

Own references

1. V. Mikhaylov et al., PoS, http://pos.sissa.it/archive/conferences/234/282/EPS-HEP2015_282.pdf.
2. V. Kushpil et al., NIM A, In Press, 2016, <http://dx.doi.org/10.1016/j.nima.2016.06.101>.

SEE study of Sol radiation detection ASICs

Laboratory of Tandetron

Maria Marcisovska

Proposal ID

362

Report regarding proposal “SEE study of SoI radiation detection ASICs”

M. Marcisovska, A. Kabatova, L. Tomasek, M. Marcisovsky, V. Kafka, Czech Technical University in Prague

The measurements were focused on the study of single-event effect (SEE) response of microelectronic structures to highly ionizing radiation, which simulates the space environment. Radiation testing was focused mainly on the soft SEE, specifically on bit-flips. Bit-flip is the change of binary information in a memory cell, caused by charged particles impinging on this component. Our goal was to measure the cross section of bit-flips depending on the particle LET.

The highest probability of bit-flip occurrence is given by particles which deposit most of their energy in the chip's shift registers, which consist of D flip-flops. For the measurement purposes, a data pattern (0xAAAA) was periodically written into the shift register, which was followed by data readout (once per second) and comparison with the entering data pattern.

The ASIC under study was irradiated on air by a 1-MeV proton beam. The particle energy was determined by Geant4 and SRIM simulations. During the irradiation, an integral flux of 10^{12} protons/mm² was reached with no SEE being observed. Other used ions were ⁴He with the energy of 3,7 MeV and ¹²C with the energy of 17,5 MeV. This experiment was focused on the specific area of the detection chip containing the shift registers. This increased the probability of the SEE occurrence. An integral flux of 10^{12} ions/mm² was reached. The upper limit of the SEU cross section was inferred from the measurement as a function of particle LET.

In the following experiment, the detection chip was placed in the vacuum chamber and irradiated by carbon and oxygen ions. The simulations show, that the ideal initial ion energies used for this irradiation are 17 MeV and 24 MeV, respectively. Irradiation with the carbon ions resulted in the expected radiation damage. However, irradiation with the oxygen ions showed no observable radiation damage.

After that, a maximum ion energy was used in order for the ions to pass through the whole active area of the detector. These data were complemented by the data taken at JINR at the U400M cyclotron. This lead to extraction of the dependence of the bit-flip cross-section on the LET of the particle.

Depth analysis of nanostructured surfaces

Laboratory of Tandetron

Petr Slepika

Proposal ID

235

Report regarding proposal: „Depth analysis of nanostructured surfaces“

P. Šlepická, V. Švorčík, Department of Solid State Engineering, The University of Chemistry and Technology, Prague, Czech Republic

High power plasma was successfully used as an efficient and inexpensive tool for polymethylpentene cytocompatibility enhancement. Proper surface roughness and morphology as well as the surface chemistry of a material are essential factors for successful utilization of a substrate intended for tissue engineering applications.

We applied oxygen and argon plasma treatments to activate the polymethylpentene (PMP) surface. We focused on investigation of the changed properties. The AFM and FIB-SEM study demonstrated that plasma treatments of PMP induced structured surfaces depending on the applied plasma setting. Measurement of the goniometry, chemical changes (functional groups by FTIR, element concentration by XPS and RBS/ERDA) was included. RBS method revealed the depth concentration profile of oxygen concentration and by ERDA, the depth concentration profile of hydrogen was measured. Plasma treatment takes place in the polymer surface layer, which corresponds to the plots, where the oxygen decreases towards the bulk, up to the depth of 150 nm, where no oxygen was detected. The results from XPS, RBS and ERDA analysis show the trends (the increase in oxygen or the decrease of hydrogen after the treatment) remain resembling.

Experiments on treated substrates with mouse fibroblasts NIH 3T3 has shown a significant increase in cell adhesion and proliferation on treated PMP substrates when compared to untreated polymer. This study demonstrates how to easily improve cytocompatibility of a very inert and resistant polymer for tissue engineering applications.

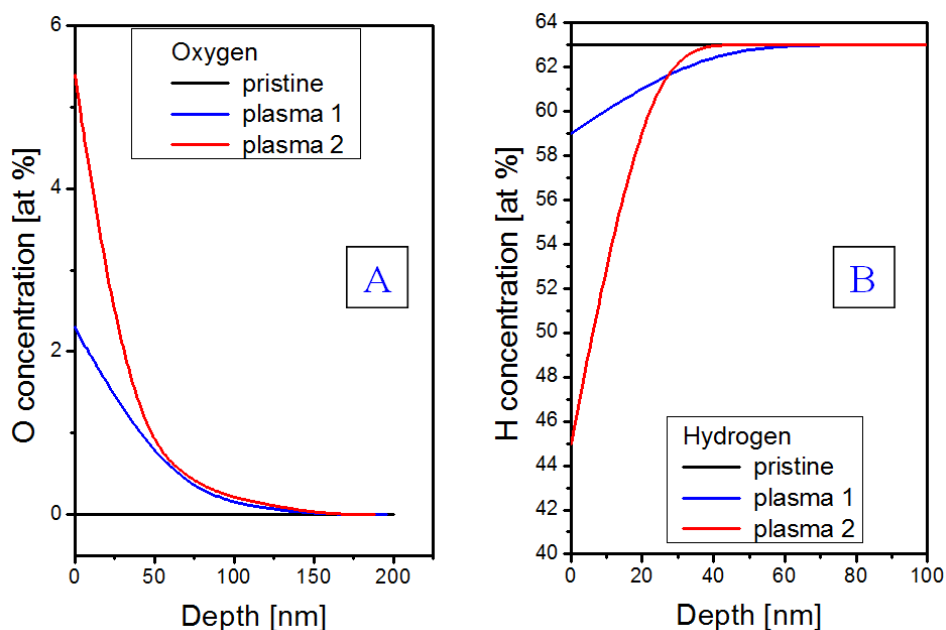


Figure. Depth concentration profile of (A) oxygen measured using RBS and (B) hydrogen measured using ERDA for pristine PMP and samples treated by plasma (200 W, 240 s): 1 – in O₂/Ar atmosphere and 2 – in Ar atmosphere.

Paper:

I. Michaljáničová, et al., *High power plasma as an efficient tool for polymethylpentene cytocompatibility enhancement*, RSC Adv. 6 (2016) 76000–76010.

Nanoscale investigation by USANS of Co-Cr alloy samples for the biomedical sector

Neutron Physics Laboratory - Neutron diffraction

Massimo Rogante

Proposal ID

364

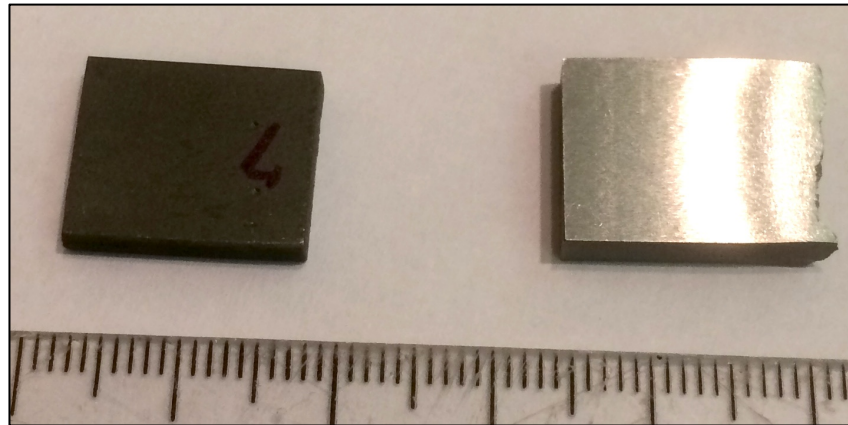


Fig. 1. Co–Cr alloy samples produced by DMLS: as-sintered state (right), after post-production thermal stress relieving treatment (left).

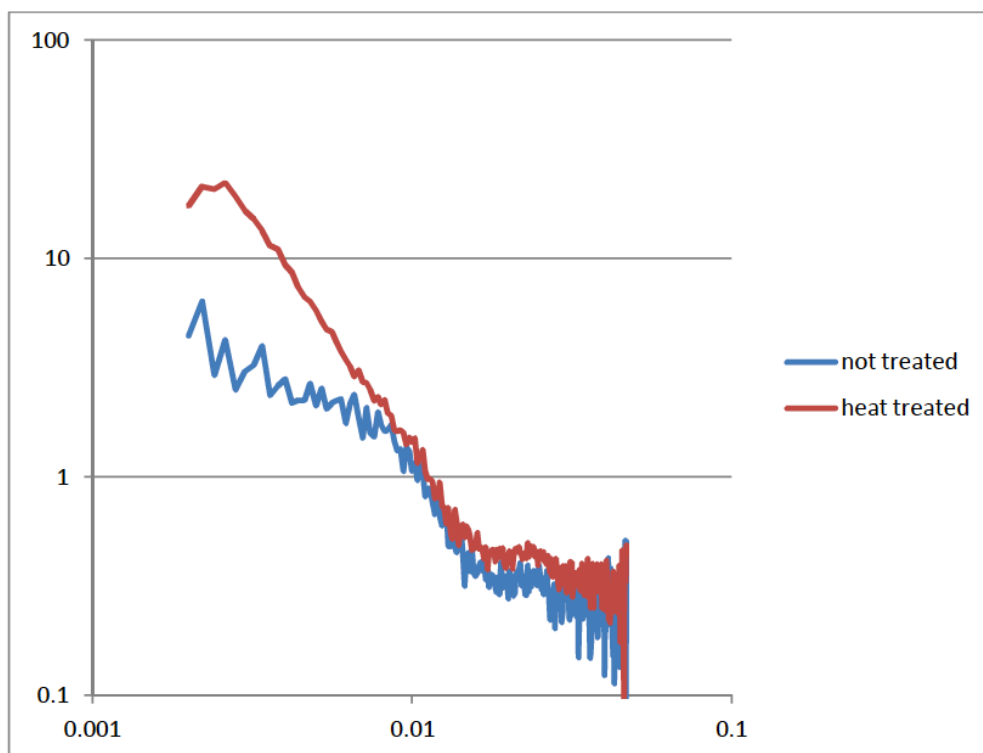


Fig. 2. Sigma (Q) curves related to a preliminary feasibility SANS analysis of the samples of Fig. 1.

References

- [1] G. Barucca, E. Santecchia, G. Majni, E. Girardin, E. Bassoli, L. Denti, A. Gatto, L. Iuliano, T. Moskalewicz, P. Mengucci, Structural characterization of biomedical Co–Cr–Mo components produced by direct metal laser sintering, *Materials Science and Engineering C* 48 (2015), pp. 263–269.
- [2] P. Mengucci, G. Barucca, A. Gatto, E. Bassoli, L. Denti, F. Fiori, E. Girardin, P. Bastianoni, B. Rutkowski, A. Czyrska-Filemonowicz, Effects of thermal treatments on microstructure and mechanical properties of a Co–Cr–Mo–W biomedical alloy produced by laser sintering, *Journal of the Mechanical Behavior of Biomedical Materials*, Vol. 60 (2016), pp. 106–117.
- [3] E. Girardin, G. Barucca, P. Mengucci, F. Fiori, E. Bassoli, A. Gatto, L. Iuliano, B. Rutkowski, Biomedical Co–Cr–Mo components produced by Direct Metal Laser Sintering, *Materials Today: Proceedings* 3 (2016), pp. 889–897.

Detection and determination of micron uranium particles in a dust - Fission track analysis technique

Neutron Physics Laboratory - Nuclear analytical methods with neutrons

Jan Lorincik

Proposal ID

241

Report regarding the proposal „Detection and determination of micron uranium particles in a dust - Fission track analysis technique“

J. Lorinčík, F. Sus, K. Sihelská, K. Řezanková, Research Center Rez, Czech Republic

Fission track analysis in nuclear forensics can be divided into several individual steps: 1. Deposition of dust particles on a substrate, 2. Sample assembly preparation, 3. Assembly irradiation in a nuclear reactor, 4. Making fiducial marks for coordinate synchronization, 5. Lexan detector etching, 6. Analysis of Fission Tracks in Lexan with optical microscope, 7. Identification of particles corresponding to the fission tracks using SEM-EDX (Fig. 1). Once the particles are identified and their coordinates recorded they can be transferred to a mass spectrometer (SIMS or LA ICPMS) and uranium isotopic composition of individual particles measured (Fig. 2).

In the course of works on this project all the above mentioned steps were tested to develop the complete analytical procedure.

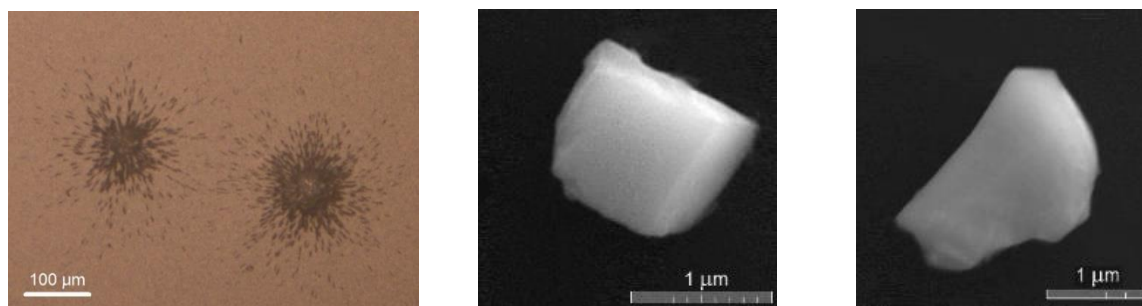


Fig. 1. Optical image of two fission-track clusters in Lexan (left) and the SEM images of the corresponding uranium-oxide particles.

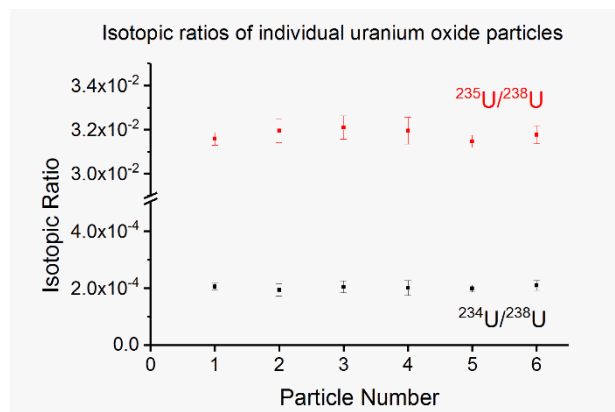


Fig. 2. Isotopic ratios of individual uranium oxide particles measured with a magnetic sector SIMS instrument.

Two parameters were used for the performance evaluation of the procedure: the success ratio (identified particles of interest using SEM-EDX over the total number of the fission track clusters) and the particle location accuracy (the geometrical error between the true position of the particle on the substrate determined with the SEM and the location predicted from the optical image of the fission tracks). The success ratio in the proposed procedure was typically ~80%, in several experiments it was 100%. The location accuracy was between 20 μm and 100 μm.

In summary, a Fission Track Analysis (FTA) procedure has been tested and developed. The main features, which differentiate our procedure from other FTA procedures, are the use of Si substrate as a particle carrier, the sample assembly design, and the use of FIB for making fiducial marks.

A structural study and ion irradiation of the silicon crystal layer

Laboratory of Tandetron

Romana Mikšová

Proposal ID

306

Report regarding proposal “A structural study and ion irradiation of the silicon crystal layer”

R. Mikšová, A. Macková, A. Jagerová, P. Malinský, Nucl. Physics Inst., Rez, Czech Republic

P. Slepíčka, V. Švorčík, Inst. Chem. Tech., Prague, Czech Republic

Our results from irradiation of Si-crystal layer on SiO₂/Si using 0.4 MeV Kr⁺, Ag⁺, Au⁺ and 5.0 MeV Ag²⁺, Au²⁺ at ion fluences of 0.5×10^{15} – 5.0×10^{15} cm⁻² show that the nuclear-energy loss is dominant for all ion species used in our experiment at the energy of 0.4 MeV and the highest is for Au⁺ ions. This is clearly proved by RBS-C, where the completely disordered structure in the implanted layer is observed even at the lowest ion-implantation fluence used. The nuclear stopping leads to atomic displacement and the production of vacancies or large-scale defects and the subsequent amorphisation of the implanted layer as was observed in RBS-C measurement, where Si layers were completely amorphised under 0.4 MeV ion implantation performed at the ion fluence of 0.5×10^{15} cm⁻² (see Figure 1a). Since amorphisation occurs near the end of range damage. For 0.4 MeV ions the end is near Si/SiO₂ interface. It is shown in ref. [1] that the critical fluence for amorphisation is lower than 1.0×10^{14} cm⁻² (at the room temperature), therefore lower as in our experiment.

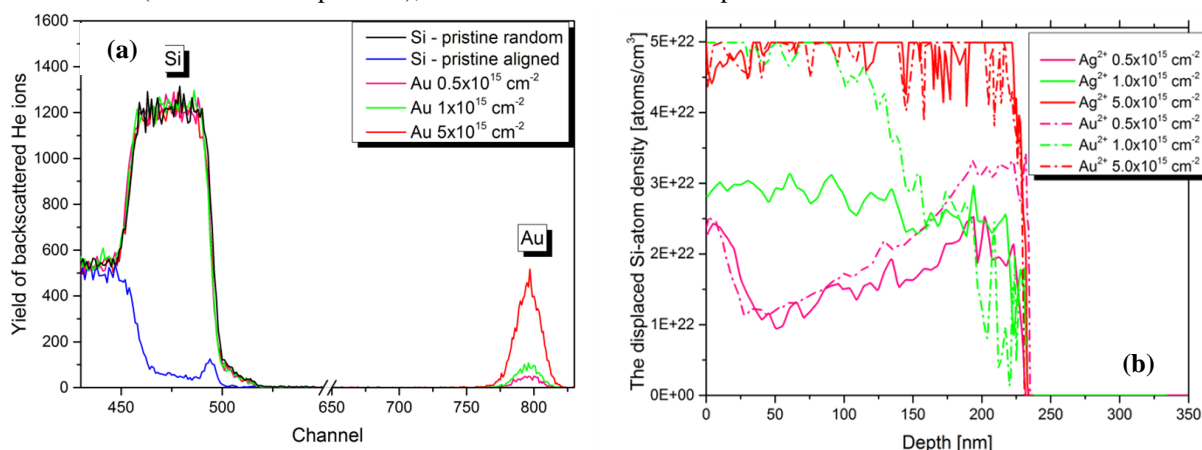


Figure 1. The RBS-C of random and aligned spectra of SOI irradiated by 0.4 MeV (a) and 5.0 MeV (b) Au⁺ at ion fluences of 0.5×10^{15} – 5.0×10^{15} cm⁻² compared to the aligned spectrum of the virgin SOI sample. The depth profile of the displaced Si-atom density in the Si layer implanted by 5.0 MeV Ag⁺ and Au⁺ ions at ion fluences of 0.5×10^{15} – 5.0×10^{15} cm⁻² (b).

In the case of the implantation of 5.0 MeV ions, the SRIM [2] code predicted more vacancies produced by Au⁺ ions than by Ag⁺ ions, which is in agreement with RBS-C results, exhibiting more progressive enhancement of Si-atom displacement density with increasing ion fluence for Au⁺ ions (see Figure 1b). In the case of 5.0 MeV Ag⁺ and Au⁺ ions, the ratios S_d/S_n were 3.23 and 1.44 and the projected range of ions is behind SiO₂/Si interface, in the Si bulk respectively. All these effects were also observed in RBS-C for the ion fluences above 1×10^{15} cm⁻². For the lowest ion fluence used, the dynamic annealing is decreasing number of vacancies, which is not included in SRIM simulation as well as the surface damage accumulation is not predicted by SRIM. It can be concluded that 5.0-MeV ions modify the structure causing the changing of axial channels during He⁺ ion channelling. RBS-C identified the relative number of disordered Si atoms, which was successfully used for the angular-scan simulation in FLUX code [3] for various ion-irradiation fluencies.

AFM found out that 5.0 MeV-ion implantation caused mainly surface smoothening and the average roughness is a descending function of the ion-implantation fluence. This effect can be connected to the progressive surface modification confirmed by RBS analysis, where the silicon-structure degradation may be reflected in smoothening caused by the predominant diffusion mechanism induced by ion implantation. The FTIR analysis confirmed Si crystalline layer modification mainly done by Si-Si bond rupture or modification depending on the prevailing nuclear or electronic stopping, respectively.

The results have been send for publication in Applied Surface Science and Surface Interface Analysis.

[1] L. Pelaz, L.A. Marqués, J. Barbolla, Appl. Phys. Rev. **96** (2004) 5947–5977.

[2] J. F. Ziegler et al., *SRIM: The stopping and range of ions in matter*, Version SRIM-2013. Available at: <http://www.srim.org/>.

[3] P.J.M. Smulders, D.O. Boerma, Nucl. Instrum. Methods Phys. Res. B **29** (1987) 471–489.

Investigation of novel composite CoNiAl-Ti by neutron diffraction and small-angle neutron scattering

Neutron Physics Laboratory - Neutron diffraction

Pavel Strunz

Proposal ID

245

Report regarding proposal “Investigation of novel composite CoNiAl-Ti by neutron diffraction”

Pavel Strunz (email: strunz@ujf.cas.cz, affiliation: Ústav jaderné fyziky AV ČR, v. v. i.),

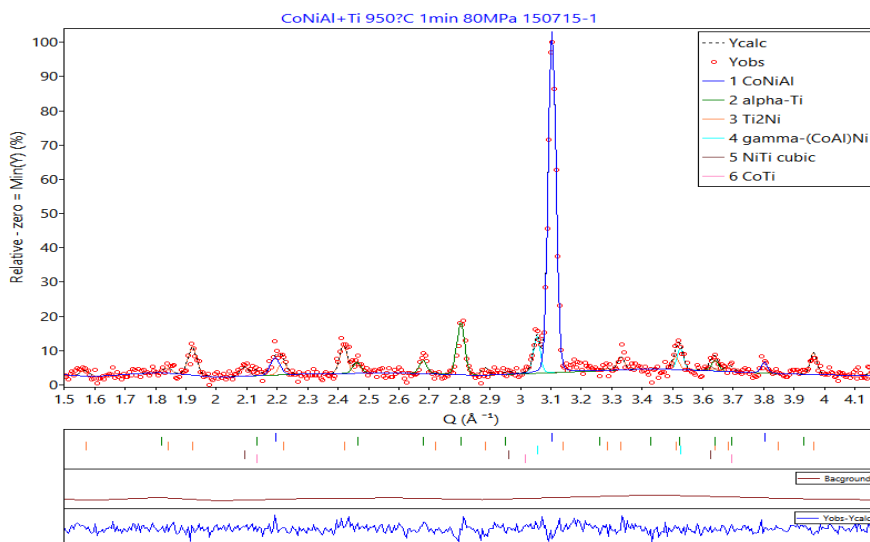
P. Beran, NPI, Oleg Heczko, IP Prague, CZ, Jaromír Kopeček, IP Prague, CZ, Tomáš Chráska, Institute of Plasma Physics, CZ, Radek Mušálek, Institute of Plasma Physics, CZ, Zdenek Pala, Institute of Plasma Physics, CZ, Josef Stráský, MFF UK Prague, CZ,

Investigation of phase composition and microstructure of composite material CoNiAl-Ti produced by Spark Plasma Sintering was proposed. The properties of the composite are expected to depend strongly on minority phase content and thus on the parameters of preparation of the material. The results complement characterization by other techniques, predominantly electron microscopy and XRD.

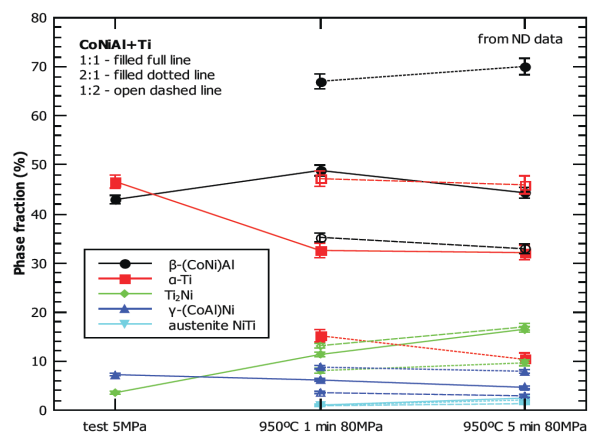
Measured samples of CoNiAl plus Ti prepared by SPS:

Sample	T, C	P, Mpa	time,min	CoNiAl:Ti	Ti, %
150713_2	911	5	0	1:1	50
150715_1	950	80	1	1:1	50
150714_1	950	80	5	1:1	50
150909_1	950	80	5	2:1	33.3
150915_1	950	80	1	2:1	33.3
150916_1	950	80	1	1:2	66.7
150916_2	950	80	5	1:2	66.7

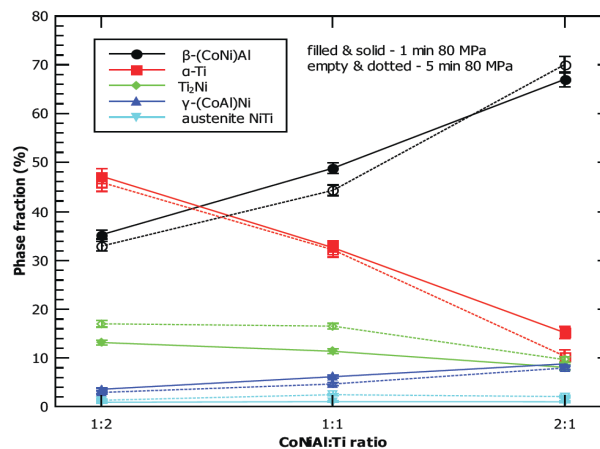
An example of measured and evaluated neutron diffraction profile:



Dependence of phase content
on the mode of sample preparation



... and on the amount of Ti in the sample:



Investigation of novel composite CoNiAl-Ti by small-angle neutron scattering and neutron diffraction

Neutron Physics Laboratory - Neutron diffraction

Pavel Strunz

Proposal ID

246

Report regarding proposal “Investigation of novel composite CoNiAl-Ti by small-angle neutron scattering and neutron diffraction”

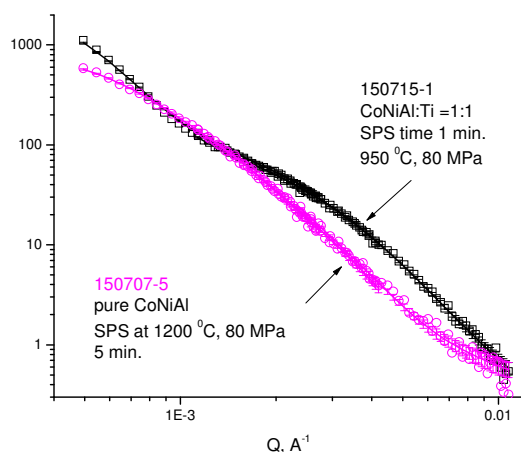
Pavel Strunz (email: strunz@ujf.cas.cz, affiliation: Ústav jaderné fyziky AV ČR, v. v. i.),
V. Ryukhtin, Oleg Heczko, IP Prague, CZ, Jaromír Kopeček, IP Prague, CZ, Tomáš Chráska, Institute of Plasma Physics, CZ, Radek Mušálek, Institute of Plasma Physics, CZ, Zdenek Pala, Institute of Plasma Physics, CZ, Josef Stráský, MFF UK Prague, CZ,

Investigation of phase composition and microstructure of composite material CoNiAl-Ti produced by Spark Plasma Sintering was proposed. The properties of the composite are expected to depend strongly on minority phase content and thus on the parameters of preparation of the material. The results complement characterization by other techniques, predominantly electron microscopy and XRD.

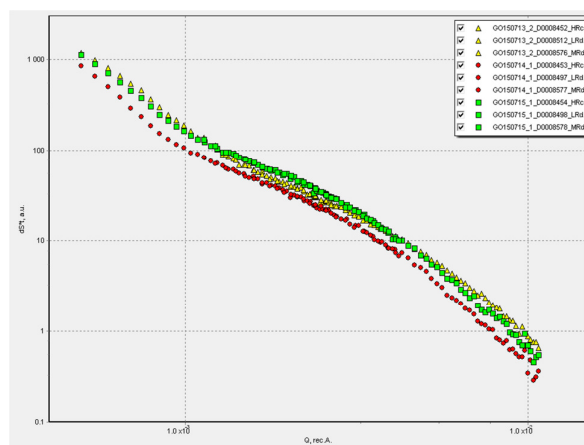
Measured samples

Sample	T, C	P, Mpa	time,min	CoNiAl:Ti	Ti, %	<R>, nm	dR
150713_2	911	5	0	1:1	50	55.25	0.69
150715_1	950	80	1	1:1	50	70.39	1.2
150714_1	950	80	5	1:1	50	75.73	2.1
150909_1	950	80	5	2:1	33.3	103.9	3
150915_1	950	80	1	2:1	33.3	86.1	1.2
150916_1	950	80	1	1:2	66.7	82.17	1.1
150916_2	950	80	5	1:2	66.7	69.26	1.5

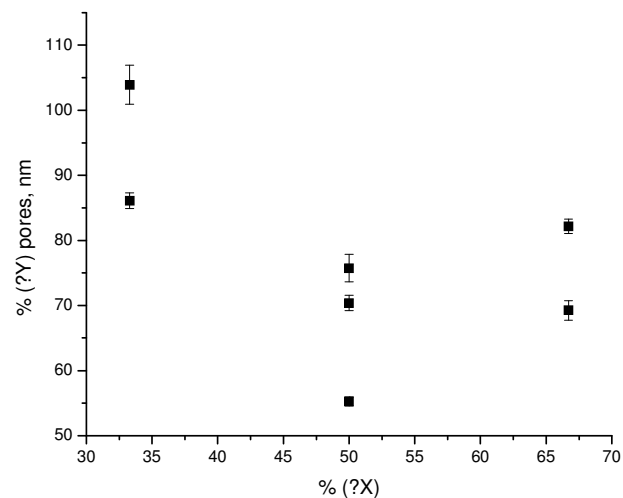
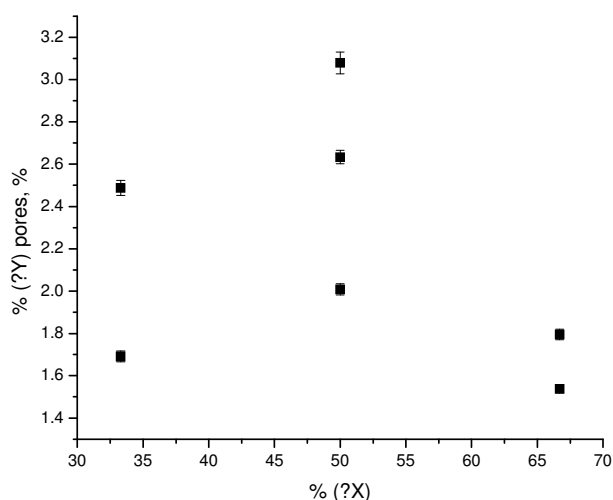
Comparison of SANS between pure CoNiAl and with Ti



Exemple of SANS from CoNiAl+Ti samples:



Probable cause of scattering: nanopores. Then, their volume fraction and mean size change according to the following figures:



Carbon 12C Test Beam

Laboratory of Cyclotron and Fast Neutron Generators

Tomáš Matlocha

Proposal ID

310

U-120M carbon $^{12}\text{C}^{6+}$ beam test - Final report

Tomas Matlocha

Proposal's realization:

The CANAM proposal id 310 was realized during 5.-7. 4. 2017 as an appendix to a Deflection system test. The U-120M cyclotron was tuned in positive regimes for Deuterium 14.1 MeV and for Deuterium 17.3 MeV. Positive ion beams for various gases were extracted using deflection system to the beamline A diagnostic unit.

Cyclotron parameters:

DT 14,1 MeV:

EMC = D – 318.6 A , C – 313.2 A

f=11.62 MHz, U_{dee}=30 kV

Udef1=42.9 kV, Udef2=21.6 kV, Udef3=37.8 kV

DT 17,3 MeV:

f=12.86 MHz, U_{dee}=34 kV,

EMC = D – 438.8 A , C – 430.85 A

Udef1=53.6 kV, Udef2=21.7 kV, Udef3=23.8 kV

For DT 14.1 MeV deuterium, helium and methane was filled. For DT 17.3 MeV deuterium, methane and CO₂ was filled.

Ion source in high impedance mode:

Arc current = 0.13 A

Arc voltage = 1700 V

Measurement:

Direct beam current over 1nA was measured with cyclotron internal current meters. For currents below 1 nA, the electrometer Keithley 614 was used. The beam diagnostics and the ion energy measurement was done using the silicon pixel detector TimePIX.

The various accelerated ion types were separated by a proper tuning of the resonance by the cyclotron main coil for ion mass to charge ratio m/Q as shown in the table below.

m/Q [u/e]	EMC (14.1 MeV)	EMC (17.3 MeV)
2.014	318.6 A	438.8 A
2.000	313.2 A	430.85 A

At the resonance for m/Q = 2.014 (deuterium) with ionization of methane a massive fraction of single ionized molecular hydrogen H₂⁺ was measured. Maximal current was 30 uAe. At the resonance for m/Q = 2.000, a maximal measured current was 1pAe. By ionization of CO₂, maximal current for m/Q was 100 pAe. The ions clusters detected by the TimePIX detector are in figures below and have area about. 50 x 50 pixels.

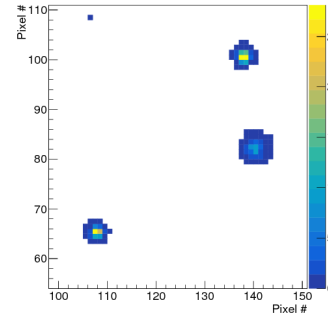


Fig. 1: Molecular hydrogen H₂⁺

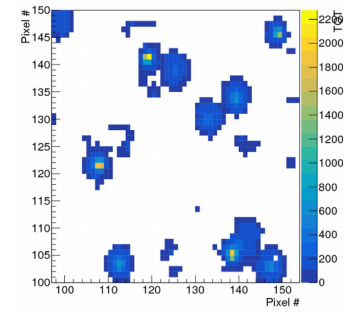


Fig. 2: Helium 4He 2⁺

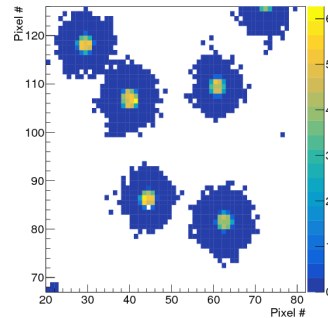


Fig. 3: Carbon 12C candidate

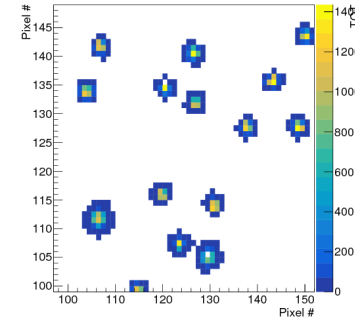


Fig. 4: Deuterium 2H

Maximum energy measured for ions accelerated from ionized methane was 25 MeV at 14.1 MeV. Helium $^4\text{He}^{2+}$ with 28 MeV should left 16 MeV in 300 um TimePIX silicon chip. Energy deposit in the chip left by deuterium 14 MeV is 3.6 MeV. Carbon $^{12}\text{C}^{6+}$ at 85 MeV should left its complete energy in the detector. Molecular hydrogen 14 MeV deposit is approx. 8 MeV.

Ion energies obtained by analysis of the TimePIX data are in Fig. 5. The results are strongly affected by changing the TimePIX THL level. The change was necessary because of a high radiation background. Also TimePIX non-linear response and non-ionization losses affected the energy scale in the measured energy distribution. From the comparison of H₂⁺ and ^4He plot can be seen that for ^4He the real measured ions were probably the molecular hydrogen H₂⁺, so direct comparison between ^4He and ^{12}C is not available.

Results:

Heavy ions with m/Q ratio in range 1.998 – 2.002 were observed at intensities up to 100 pAe with energy deposit in TimePIX detector approx. 25 MeV. Resolution of carbon and helium ions is not clear. For a clear distinction between these ions with almost identical m/Q, a further measurement with another detector type is necessary.

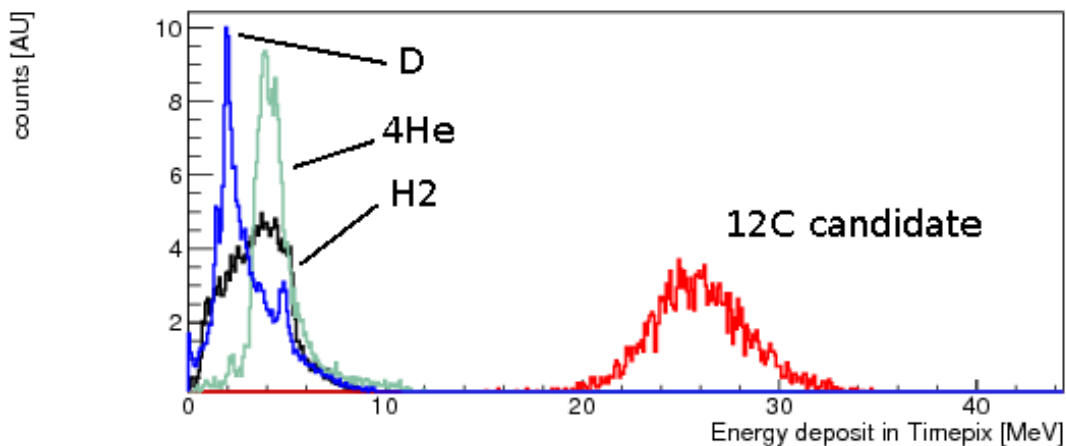


Fig. 5: Energy plots

Residual stress measurement

Neutron Physics Laboratory - Neutron diffraction

Josef Hodek

Proposal ID

311

Final report 'Residual stress measurement'

J. Hodek, A. Prantl, COMTES FHT a.s., Dobruany, Czech Republic

Residual stress is hard to obtain for bulk objects. The contour method can determine residual stress distribution for bulk objects. The neutron diffraction measurement was done to obtain measurement that can be comparable to the contour method computation and the finite element method computation of the heat treatment. The sample was a stainless cylinder with sizes D58/60mm. There were measured only strains in two directions due to sizes of the sample. The computation both the contour method and the finite element method were done in MSC MARC computation software.

Comparison was done on the lines 01-04 see Figure 1

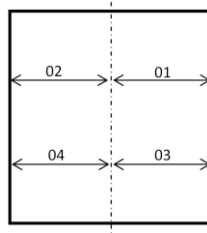


Figure 1 Identification of the comparison lines

The strain distributions are on the Figure 2 - Figure 4.

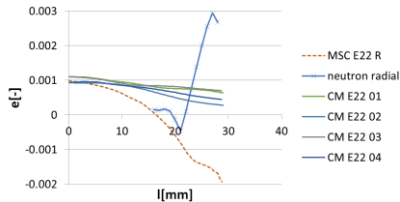


Figure 2 Strain - radial

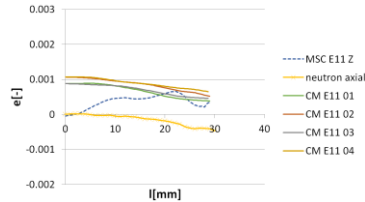


Figure 3 Strain - axial

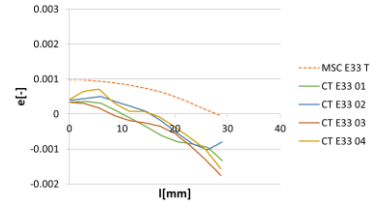


Figure 4 Strain - tangential

where: MSC – the finite element computation

CM – the contour method computation

neutron – the neutron diffraction measurement

Microstructural investigations of BaTiO₃-based ceramics prepared by Sparc Plasma Sintering (AdMat)

Neutron Physics Laboratory - Neutron diffraction

Vasyl Ryukhtin

Proposal ID

249

Microstructural investigations of BaTiO₃-based ceramics prepared by Sparc Plasma Sintering (SPS)

Vasyl Ryukhtin, Nuclear Physics Institute NPI (ASCR), Neutron Physics Department

Pavel Ctibor, Institute of Plasma Physics, Prague Czech Republic

A set of BaTiO₃-based samples were sintered by SPS at Institute of Plasma Physics (IPP) of ASCR. Spark plasma sintering enables very rapid fabrication of bulk ceramic materials. It is an emerging consolidation technique, which combines pulsed electric currents and uniaxial pressure induced compaction. Heating rates, applied pressures and pulsed current patterns are the main factors responsible for the enhancement of densification kinetics and conservation of the submicron-scale structure of the materials [1]. This material was widely studied at material engineering (ME) department of IPP ASCR as excellent material for plasma spraying (PS).

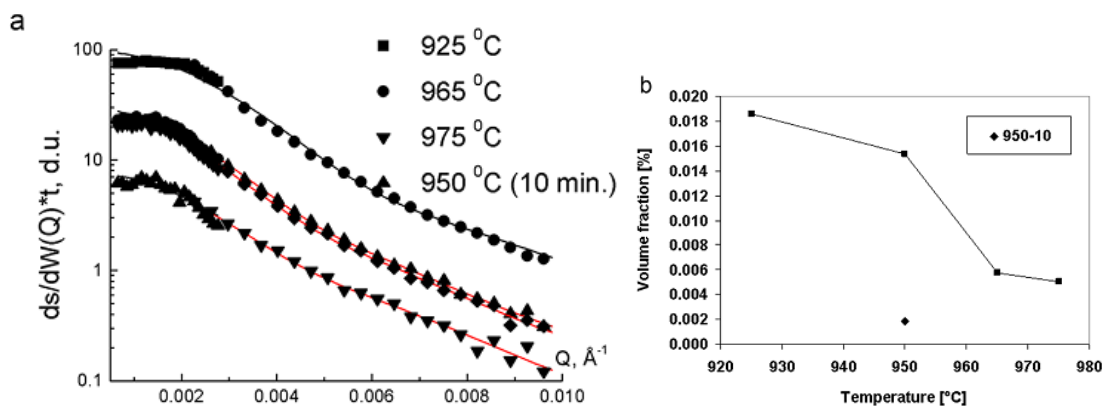


Fig. 1. SANS scattering spectra (a) and fitted volume fractions of pores (b).

The SANS curves were fitted using simple structural model of spherical particles (Fig. 1a) with help of SASprof software. Although, for some samples scattering data in low angle region were distorted by multiple scattering a part of spectra with high angles were fitted reasonably good. However, because of the multiple scattering, a pore size distribution cannot be specified and only the volume fraction V is representative (Fig. 1b). The results include all pores between 20 nm and 3 mm. Certain trend could be seen (Fig. 1b) – the higher is the sintering temperature, the lower is the porosity. Increasing the dwell time at 950 °C led to further decrease in the porosity volume fraction. For the sample 950-10 the volume fraction is nearly 10 times smaller compare to the most porous sample 925.

Reference

[1] P. Ctibor et al, *Barium titanate nanometric polycrystalline ceramics fired by spark plasma sintering* Ceramics International 42 (2016) 15989–15993.

Radiation Hardness of Si Pixel Chips and Components for ALICE Inner Tracker System Upgrade Project

Laboratory of Cyclotron and Fast Neutron Generators

Filip Krizek

Proposal ID

313

Report regarding the proposal: Radiation Hardness of Silicon Pixel Chips and Components for the ALICE Inner Tracking System Upgrade Project

Filip Křížek, Nuclear Physics Institute of CAS

The ALPIDE chips are monolithic active pixel sensors which are going to be used in the upgraded Inner Tracking System (ITS) detector of the ALICE experiment at CERN. In 2017, we continued with the tests of their radiation hardness and we studied the chip performance as a function of the accumulated total ionization dose (TID) and reverse substrate bias. The corresponding measurements were carried out on 19.1., 1.3., 2.3., 10.4., 3.5., 4.5., 15.6., 24.7., 28.8., 18.9., 11.10., and 6.11. Figure 1 shows an example of the obtained dependence of the chip sensitivity threshold as a function of the accumulated TID. At present the sensor accumulated a TID of 1.6 Mrad and is still fully operational. The chips irradiated at Rez were then further characterized at the test beams at the CERN PS. Results from this activity were published in the diploma thesis of Artem Isakov [1] and were presented on regular meetings of the ITS upgrade characterization group (10.5., 4.10., 25.10.). In the test performed on 14.6., we irradiated chips on the inner barrel stave and found that they follow the expected behavior. Further tests of radiation hardness were performed also with a field programmable gate array (FPGA) and the corresponding firmware design which are going to be used in the ITS readout unit (RU). On 22.–24.5. and 19.–20.6. we irradiated a RU prototype based on the Xilinx Kintex-7 325T FPGA. The goal of the test was to investigate various soft error mitigation firmware designs. Results from this activity were presented by Krysztof Sielkiewicz at the NSREC-2017 conference [2]. The final version of the RU based on Xilinx XCKU060 FPGA was tested during 4.–6.12. These measurements provide an important data for the Production Readiness Review of the ITS RU project which will take place in spring 2018.

References

- [1] A. Isakov, *Investigation of silicon pixel sensors for the ALICE Inner Tracking System upgrade project*, diploma thesis, Tomsk Polytechnic University, 2017.
- [2] K. Sielkiewicz et al., *Experimental Methods and Results for the Evaluation of Triple Modulator Redundancy SEU Mitigation Techniques with the Kintex-7 FPGA*, IEEE NSREC-2017 conference.

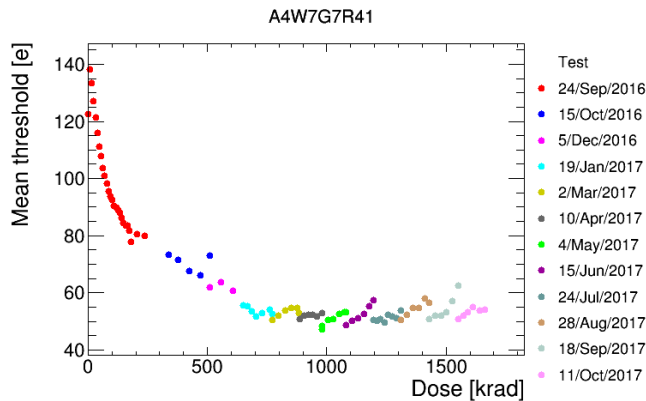


Figure 1: ALPIDE sensor sensitivity threshold as a function of the accumulated total ionization dose. The threshold is measured in electron charges. The sensor was irradiated with a beam of 30 MeV protons. The legend quotes the dates of irradiation campaigns.

Study of CR-39 response to short range nuclei with the purpose of space radiation track analysis

Laboratory of Tandetron

Konstantin Inozemtsev

Proposal ID

314

Report on CANAM Research Project

“Study of CR-39 response to short range nuclei with the purpose of space radiation track analysis” (Proposal ID 314; April, 23-28 2017)

K.O. Inozemtsev^{1,2,*}, V.V. Kushin^{1,2}, V. Havránek³, O. Ploc³, I. Ambrožová³ and V.A. Shurshakov²

¹National Research Nuclear University MEPhI (Moscow Engineering Physics Institute), Moscow, Russian Federation

²Russian Academy of Sciences, Institute of Biomedical Problems (IBMP), Moscow, Russian Federation

³Czech Academy of Sciences, Nuclear Physics Institute, Řež, Czech Republic

Scope

The purpose of this Project is to study the solid state nuclear track detector (SSNTD) CR-39 “Tastrak” response to particles with variable energy losses dE/dx in the Bragg peak vicinity. Low energy H and C nuclei are appropriate to simulate tracks of secondary nuclear fragments in the composition of cosmic rays onboard a spacecraft [1]. Since the key track parameter – etch rate ratio (sensitivity) V is associated with dE/dx value, it is sufficient to use original scanning techniques and track analysis [2].

Results of this study are necessary for the reliable measurement of secondary space radiation [1] in the forthcoming joint “CZENDA” experiment onboard BION-M2 spacecraft, “MATRYOSHKA-R” and “PHOENIX” projects onboard the International Space Station.

Experiment

The series of CR-39 SSNTDs were irradiated at the LT laboratory of NPI CAS with H and C ions in the Bragg peak vicinity. The irradiation conditions are specified in Table 1.

Table 1

The specification of ion species, energies and incident angles

Ion	Initial Energy [MeV]	LET (H ₂ O) on detector surface [keV/μm]	Incident angles, °
H	5.8	7.5	85, 90
	4	9.7	75, 90
	2	16.4	60, 75
	1.5	20.0	
	1	24.0	45, 60, 75
C	18	614	45, 60
	15	674	
	10	803	30, 45, 60, 75, 90

Methods

After irradiation, the SSNTD species were etched in 6 N NaOH solution under 70° C. The corresponding bulk etch ratio was $1.3 \mu\text{m}^{-1}\cdot\text{hr}$. The etching duration was selected for each sample individually, taking into account the etch rate ratio and incident angle.

After chemical etching, the sets of track geometrical parameters are measured: the (D,d,H) set was measured for all tracks and (D,d,l) set was measured if possible. The abovementioned track parameters are: H – the removed layer thickness, d – the minor track opening ellipse diameter, D – the major track opening ellipse diameter, l – the track full projected length. These parameters were used to evaluate the values of mean etch rate ratio V , incident angle, amount of bulk etch and etched track length (residual range).

The track scanning was performed on Carl Zeiss® AxioScope.A1 optical microscope manually.

Track data were processed with the use of two alternative approaches described in detail in Ref. [2].

Results

The evolution of etch rate ratio V for protons versus initial energy, etching time T and incident angle is presented in Fig. 1 in comparison with *Hermesdorf*, 2009 data [3].

The track data, obtained for the 1 MeV protons after 11 and 12 hr etching and Carbons after 1 hr etching allowed estimating the particle’s residual range. The experimental

values of residual range are compared with *SRIM-code* data [4] in Table 2.

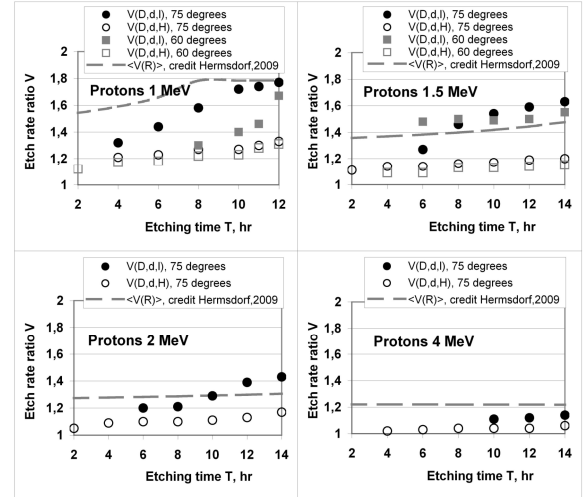


Fig.1. Evolution of etch rate ratio V measured with the use of different sets of track geometrical parameters [1] versus etching time and incident angle in comparison with *Hermesdorf* data [3]. Experimental errors are $< 5\%$ for $V(D,d,H)$ data, and $10-15\%$ for $V(D,d,l)$ data.

Table 2

The comparison of experimental and theoretical values of ion’s residual ranges

Ion	Initial Energy [MeV]	Mean residual range in CR-39 [keV/μm]	Theoretical residual range in CR-39, [keV/μm]
H	1	15.84 ± 1.21	19.81
C	18	16.41 ± 1.26	20.41
	15	12.97 ± 0.62	16.59
	10	9.31 ± 0.49	10.96

The data obtained for 5.8 MeV protons allowed to estimate the SSNTD “Tastrak” lower LET threshold in $\sim 9 \text{ keV}/\mu\text{m}$ (in CR-39 material).

Summary

In this experiment, the data concerned the response of the CR-39 detector to the short-range protons and carbon nuclei are obtained. Two alternative approaches [2] are applied to estimate the key track parameter – etch rate ratio V . The results of the experiment are planned to be submitted to one of the international journals.

References

- [1] Inozemtsev, K.O., Kushin, V.V., Kodaira, S., Shurshakov, V.A. *Observation of fragmentation events caused by space radiation: contribution to the LET spectrum as measured with CR-39 track detectors*, Radiation Measurements, 95, pp. 37-43, 2016
- [2] Inozemtsev, K.O., Kushin, V.V. *Comparative analysis of CR-39 sensitivity for different sets of measurable track parameters*, Radiation Measurements, 91, pp. 44-49, 2016
- [3] Hermesdorf, D. *Measurement and comparative evaluation of the sensitivity V for protons and hydrogen isotopes registration in PADC detectors of type CR-39*, Radiation Measurements, 44, (9–10), pp. 806-812, 2009
- [4] Ziegler, J.F., Ziegler, M.D., Biersack, J.P. *SRIM – The stopping and range of ions in matter (2010)*, Nuclear Instruments and Methods in Physics Research Section B: Beam Interactions with Materials and Atoms, 268, (11–12), pp. 1818-1823, 2010

Acknowledgments

Authors would like to thank the staff of the LT Laboratory for the perfect experiment, Mrs. Markéta Sommerová for the visit arrangement, and Dr. Anna Macková for the experiment organization.

* Project proposer, mailto: dio2014@yandex.com

Phase analysis of HSSs

Neutron Physics Laboratory - Neutron diffraction

Darya Novikova

Proposal ID

315

Report regarding proposal “Phase analysis of HSSs”

D. Novikova, Technopark Kralupy, UCT Prague, Czech Republic

P. Beran, Nucl. Physics Inst., Rez, Czech Republic

Neutron diffraction experiments were performed on two CP1000 and DP1000 specimens using MEREDIT instrument. The motivation of experiment was to study phase fractions content of CP1000 and DP1000 steels.

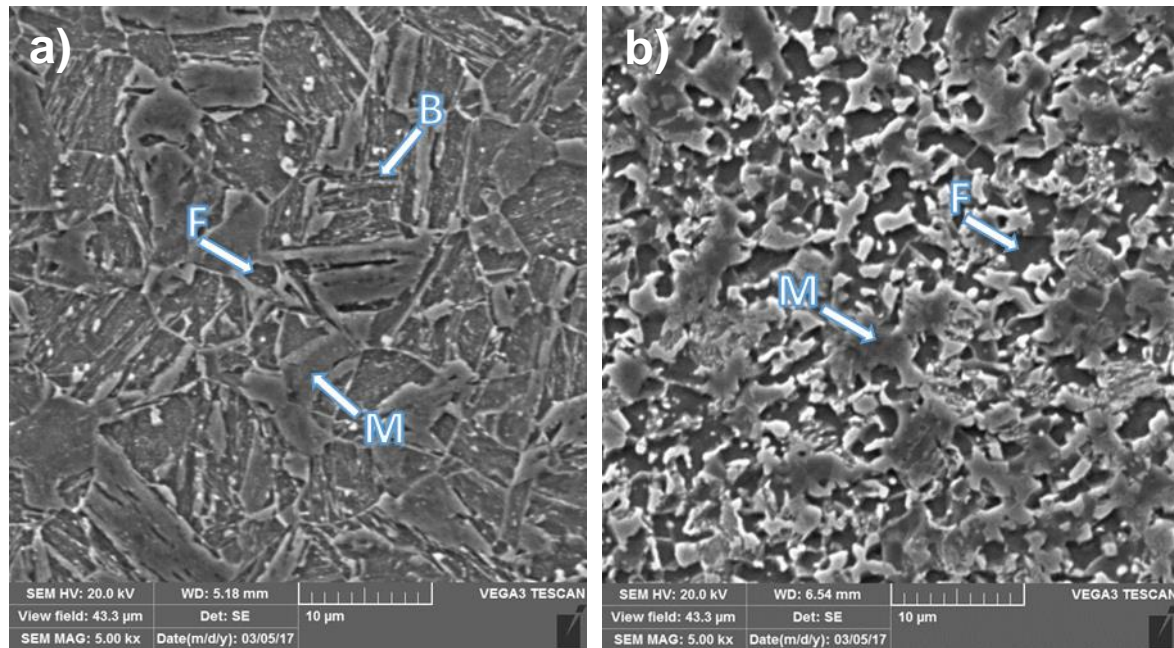


Fig. 1: SEM images of a) CP1000 and b) DP1000

Results obtained from neutron diffraction are shown in Table 1 and Table 2.

	Phase N.1 martensite-alpha	Phase N. 2 ferrite	Phase N. 3 austenite
CP1000	2.87631(94) Å	2.86551(91) Å	3.6051(54) Å
DP1000	2.8738(13) Å	2.8655(17) Å	3.6022(24) Å

Table 1: Unit cell parameters

	Phase N.1 martensite-alpha	Phase N. 2 ferrite	Phase N. 3 austenite
CP1000	47.2 ± 1.22 %	51.86 ± 1.26 %	0.94 ± 0.05 %
DP1000	62.15 ± 3.1 %	35.88 ± 2.6 %	1.96 ± 0.08 %

Table 2: Phase fractions

Martensite, ferrite and austenite volume content was evaluated. Martensite and ferrite phases were distinguished based on small differences in lattice parameters. Content of ferrite and martensite were in agreement with results from SEM and colour metallography analysis. CP1000 steel might also contain bainite fraction, but it was not possible to distinguish bainite from martensite using neutron diffraction results.

These results were used for conference paper [1]. It is also will be used for a paper about microstructure characterization of CP1000 and DP1000 steels.

[1] D. Rudomilova, T. Prosek, A. Muhr, H. Duchaczek, G. Luckeneder, P. Novak, P. Salvetr, P. Beran, Hydrogen permeability of high strength steels and model structures, SteelHydrogen2018 Proceedings (2018).

Ion modification of GaN crystalline structures

Laboratory of Tandetron

Romana Mikšová

Proposal ID

317

Report regarding proposal “Ion modification of GaN crystalline structures.”

A. Macková, A. Jagerová, P. Malinský, Nuclear Physics Institute of the Czech Academy of Sciences, v. v. i.,
Rez, Czech Republic

Z. Sofer, D. Sedmidubský, K. Klímová, Department of Inorganic Chemistry, Institute of Chemical Technology,
Prague, Czech Republic

R. Böttger, S. Akhmadaliev, Institute of Ion Beam Physics and Materials Research, Helmholtz Zentrum
Dresden-Rossendorf, Dresden, Germany

In our results, we have carried out a study of a GaN epitaxial layer (of c-plane and a-plane) implanted with Gd, Kr and Au ions at energy of 400 keV and 5 MeV Au ions using implantation fluences ranging from $5 \times 10^{14} \text{ cm}^{-2}$ to $5 \times 10^{15} \text{ cm}^{-2}$. The damage accumulation in the buried layer is much more pronounced in c-plane (0001) GaN than in a-plane (11–20) GaN for both ion species used. More pronounced differences in damage accumulation between a-plane and c-plane GaN are observed in the fluence range 0.5×10^{14} – $1 \times 10^{15} \text{ cm}^{-2}$ for Gd implanted GaN and 1×10^{15} – $5 \times 10^{15} \text{ cm}^{-2}$ in the Kr implanted GaN.

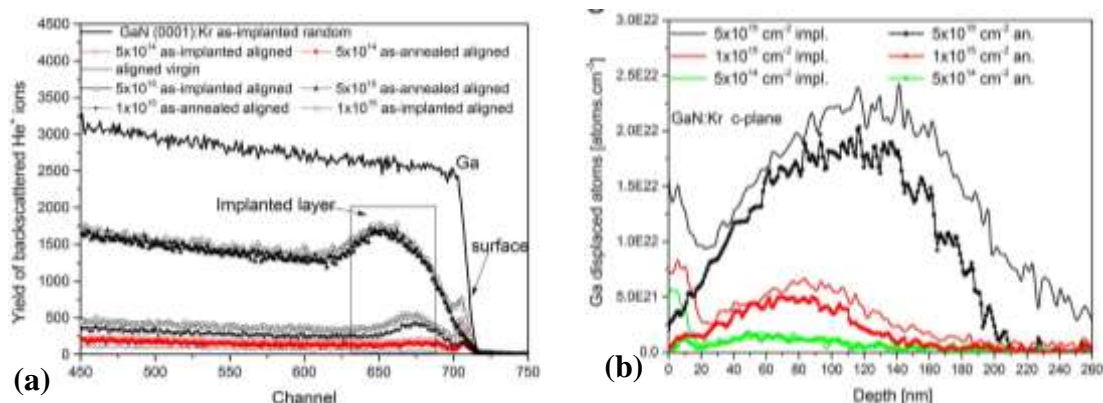


Figure 1. The RBS-channelling aligned spectra for as-implanted and as-annealed samples implanted with Kr ion in c-plane GaN (a). The density–depth profile of displacement Ga atoms in GaN as-implanted with Kr ions: as-implanted and as-annealed c-plane GaN b).

Lower surface disorder is evident in Kr-implanted GaN than in Gd-implanted GaN for the same implantation fluence. Annealing has caused a progressive decline in the disorder preferably in the surface layer and also in the bulk implanted the latter one mainly for c-plane GaN for both ion species.

Gallium nitride implanted with 400-keV Au ions shows the bimodal depth profiles at a fluence of $5 \times 10^{15} \text{ cm}^{-2}$ in as-implanted samples. More damage accumulation was observed in the buried layer in the case of c-plane GaN than in a-plane for 400-keV ion implantation energy, in case the nuclear stopping prevails (Figure 2). In case of 5-MeV Au ions modified surface GaN, where electronic stopping prevails the surface damage is significantly lower comparing to 400-keV Au implantation and the long range defect.

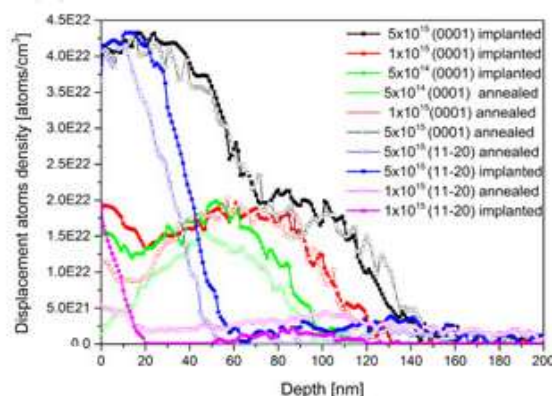


Figure 2. The density–depth profile of displacement atoms in gallium nitride as-implanted with Au at ion-implantation energy of 400 keV in as-implanted and as-annealed c-plane and a-plane GaN.

The results were published in Surface and Coatings Technology, Surface and Interface Analysis, Thin Solids Films and Nuclear Instruments and Methods in Physics Research B.

Excitation functions of the of proton- and deuteron-induced reactions on Zn-64, As-75, Y-89, Mo-100

Laboratory of Cyclotron and Fast Neutron Generators

Ondrej Lebeda

Proposal ID

64

Excitation functions of the of proton- and deuteron-induced reactions on ^{64}Zn , ^{75}As , ^{89}Y , ^{100}Mo

Ondřej Lebeda, Vlasta Zdychová, Jaroslav Červenák and Jan Štursa

*Nuclear Physics Institute, Řež, Czech Republic
Czech Technical University, Prague*

Detailed measurement of the deuteron-induced excitation functions on ^{89}Y in the energy range of 3.9–19.5 MeV was performed resulting in new excitation function for formation of ^{88}Zr , ^{89m}Zr , ^{89}Zr , ^{88}Y , ^{90m}Y and ^{87m}Sr (Fig. 1). The data were compared with previously published results and prediction of the TALYS code. Parallel use of titanium and aluminium beam monitors revealed systematic difference between the recommended cross-sections of both monitoring reactions and provided new cross-section data for formation of ^{24}Na , ^{27}Mg , ^{43}Sc , ^{44m}Sc , ^{44}Sc , ^{46}Sc , ^{47}Sc and ^{48}Sc (Fig. 1). Results were published in a peer-reviewed journal [1] and included in the EXFOR data base.

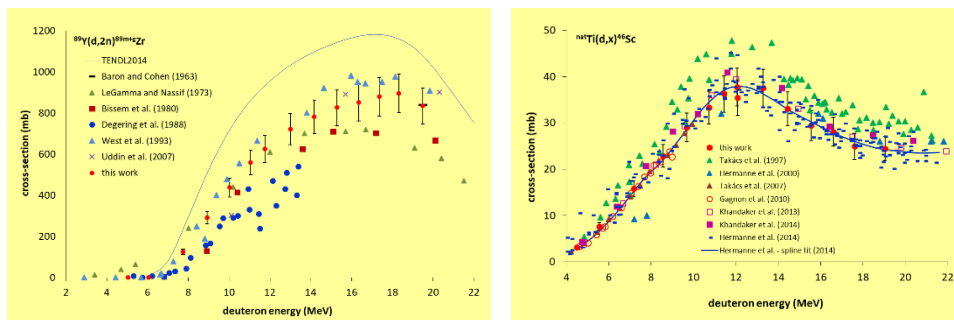


Fig. 1 Excitation function of the $^{89}\text{Y}(\text{d},\text{n})^{89\text{m}+\text{g}}\text{Zr}$ for the formation of medically relevant ^{89}Zr and excitation function of the $^{\text{nat}}\text{Ti}(\text{d},\text{x})^{46}\text{Sc}$ suitable for the beam monitoring

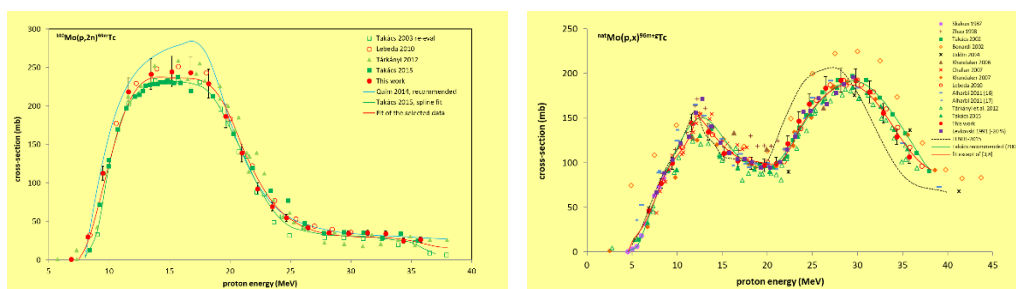


Fig. 2 Selected cross-sections for the $^{100}\text{Mo}(p,2n)$ nuclear reaction and fit of the recommended values; cross-sections for the beam monitoring reaction $^{\text{nat}}\text{Mo}(p,x)^{96\text{m}+g}\text{Tc}$ and their fitting resulting in the recommended data

Due to the lack of thin foils of precise thickness made out of highly enriched metals, we decided to re-measure excitation functions of protons on natural molybdenum, as the elemental cross-sections may be in the case of the nuclear reactions on ^{100}Mo converted into isotopic cross-sections. The extensive experiment allowed us then to provide another set of data important not only for the production of medically relevant $^{99\text{m}}\text{Tc}$ and ^{99}Mo , but also for the $^{\text{nat}}\text{Mo}(\text{p},\text{x})^{96\text{m}+\text{g}}\text{Tc}$ reaction relevant for both beam monitoring and TLA, as well as data for production of $^{95\text{m}}\text{Tc}$, a suitable long-lived technetium tracer. Altogether, almost 30 excitation functions were obtained covering the proton beam energy range of 7–36 MeV, some of them were provided for the first time ($^{97\text{m}}\text{Tc}$, $^{88\text{g}}\text{Nb}$, $^{88\text{m}}\text{Nb}$ and $^{89\text{m}}\text{Nb}$) [2]. Results are included in the EXFOR data base.

Due to the problems with the target preparation, we have resigned on the measurement of the proton-induced excitation functions on ^{64}Zn . The sputtered targets made out of ^{75}As were not suitable for the proton beam activation, the bombardment resulted in their significant damage that didn't allow for obtaining reliable data.

The rich experimental material collected during the experiments was then included in an extensive works performed within the IAEA CRP project.

- [1] Lebeda, O. – Štursa, J. – Ráliš, J. Experimental cross-sections of deuteron-induced reaction on ^{89}Y up to 20 MeV; comparison of $^{\text{nat}}\text{Ti}(\text{d},\text{x})^{48}\text{V}$ and $^{27}\text{Al}(\text{d},\text{x})^{24}\text{Na}$ monitor reactions. *Nuclear Instruments and Methods in Physics Research B*, 2015, vol. 360, pp. 118–128.
doi: 10.1016/j.nimb.2015.08.036
- [2] Červenák, J. – Lebeda, O. Experimental cross-sections for proton-induced reaction on $^{\text{nat}}\text{Mo}$. *Nuclear Instruments and Methods in Physics Research B*, 2016, vol. 380, pp. 32–49.
doi: 10.1016/j.nimb.2016.05.006

Carrier Lifetime Control in Bipolar 4H-SiC High Voltage Devices

Laboratory of Tandetron

Pavel Hazdra

Proposal ID

320

Carrier Lifetime Control in Bipolar 4H-SiC High Voltage Devices

P. Hazdra¹, S. Popelka¹ and A. Schöner²

¹ Czech Technical University in Prague, Czech Republic

² Ascatron AB, Kista, Sweden

The effect of local lifetime control by proton irradiation on the static and dynamic parameters of 4H-SiC high voltage bipolar power devices was investigated. Recombination centers acting as lifetime killers were introduced locally by proton irradiation into 10 kV SiC PiN diode chips fabricated on lightly doped ($< 10^{15} \text{ cm}^{-3}$) *n*-type 4H-SiC epilayers. Devices were irradiated from the anode side with 800 keV or 1000 keV protons to fluences from 5×10^9 to $1 \times 10^{11} \text{ cm}^{-2}$ using the 3 MeV tandetron facility in NPI CAS Rez. The irradiation energy was chosen in order to place the damage peak beyond the anode junction. Diode static and dynamic parameters were characterized prior to and after proton irradiation. Radiation defects were characterized by capacitance deep level transient spectroscopy (DLTS) and C-V profiling. The excess carrier dynamics were measured by the OCVD and analyzed using the calibrated device simulator ATLAS from Silvaco, Inc.. Recombination models accounting for the effect of introduced deep levels were set according to experimental results obtained by C-V and DLTS.

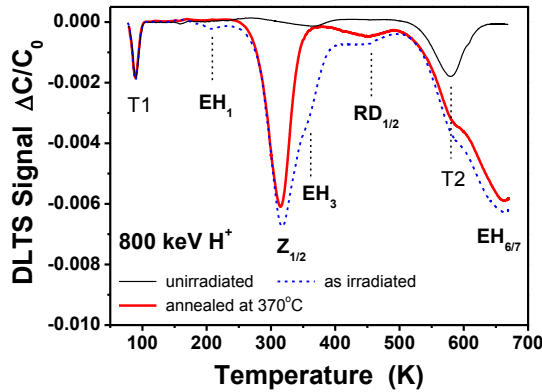


Fig. 1. DLTS spectra of *n*-base of the 4H-SiC PiN diode measured before (black thin) and after (short-dashed) irradiation with 800 keV protons to a fluence of $5 \times 10^9 \text{ cm}^{-2}$ and after annealing at 370°C (red thick).

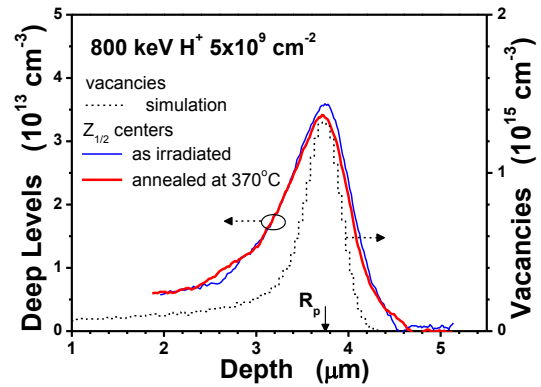


Fig. 2. Profile of the $Z_{1/2}$ centre in the *n*-base of the 4H-SiC PiN diode irradiated with 800 keV protons together with the simulated profile of primary vacancies (short-dashed).

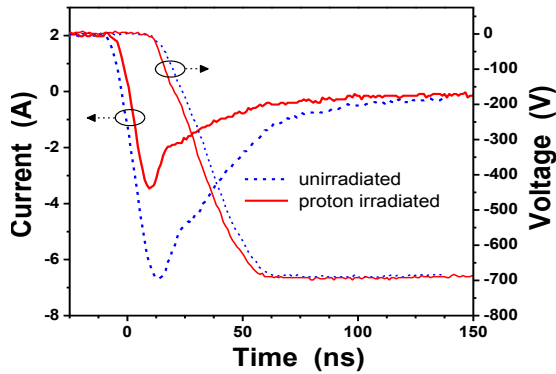


Fig. 3. Measured reverse recovery of an unirradiated SiC PiN diode and a diode irradiated with 800 keV protons to a fluence of $1 \times 10^{11} \text{ cm}^{-2}$ (room temperature).

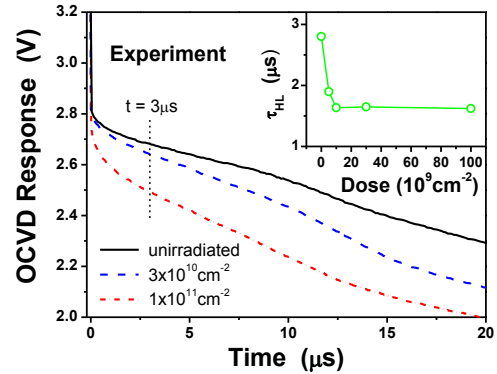


Fig. 4. Measured OCVD responses of 4H-SiC PiN diodes irradiated with different fluences of 800 keV protons. The values of high-level lifetime τ_{HL} (extracted at $t = 3 \mu\text{s}$) for different irradiation fluences are shown in the inset.

Results show that proton implantation followed by low temperature annealing can be used for controllable local lifetime reduction in SiC devices. The dominant recombination centre is the $Z_{1/2}$ defect (Fig.1), whose distribution can be set by irradiation energy and fluence (Fig.2). The local lifetime reduction, which improves diode recovery (Fig.3), can be monitored by OCVD response (Fig.4) and simulated using the SRH model accounting for the $Z_{1/2}$ defect. Preliminary results were presented at the International Conference on Silicon Carbide and Related Materials 2017, Washington, USA, 17-22 September 2017 [1].

Reference

- [1] P. Hazdra, S. Popelka, A. Schöner, Local Lifetime Control in 4H-SiC by Proton Irradiation, Mater. Sci. Forum 2018 (Proc. of ICSCRM 2018, Washington, 2017) to be published.

Reactions of organometallic complexes relevant for the ion beam cancer therapy

Laboratory of Cyclotron and Fast Neutron Generators

Marie Davidkova

Proposal ID

321

Reactions of organometallic complexes relevant for the ion beam cancer therapy

Dan Reimitz, Dept. of Nuclear Chemistry, Faculty of Nuclear Sciences and Physical Engineering, Czech Technical University in Prague

Marie Davidková, Dept. of Radiation Dosimetry, Nuclear Physics Institute of the CAS

Oto Mestek, Dept. of Analytical Chemistry, University of Chemical Technology, Prague

Jiří Pinkas, Jaroslav Kočíšek, J. Heyrovský Institute of Physical Chemistry of the CAS

Experimental study explored combined effect of RAPTA C ($\text{Ru}(\eta^6\text{-p-cymene})\text{Cl}_2(1,3,5\text{-triaz-7-phosphatricyclo-[3.3.1.1]decanephosphine})$) or CDDP (cis-diamminedichloridoplatinum(II)) and radiation on the DNA damage formation. DNA plasmids pBR322 have been irradiated by Co-60 gamma rays in presence of free and bound studied ligands. Changes of DNA plasmid conformation have been evaluated using agarose gel electrophoresis.

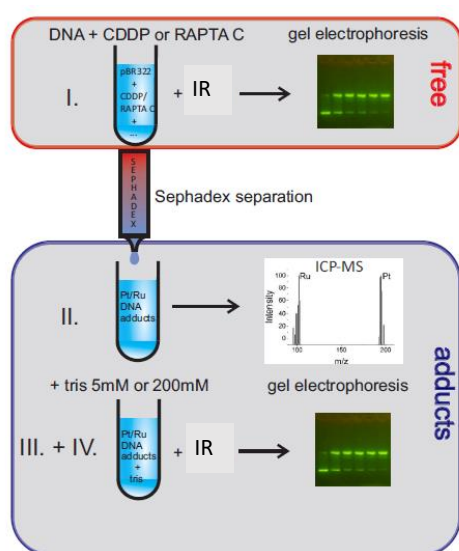


Figure 1: Scheme of the experiments performed in this study.

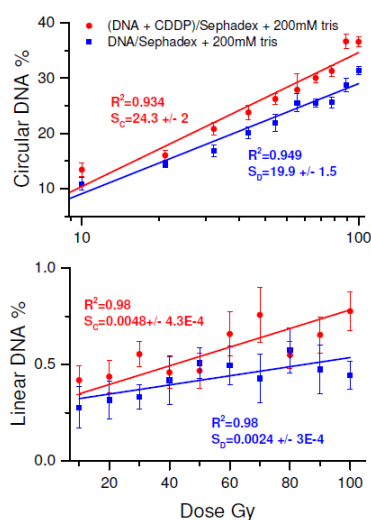


Figure 2: Radiation induced damage to DNA modified by CDDP at the level of ~6 Pt/plasmid in the presence of 200mM tris buffer.

When irradiating plasmid DNA in solution with free molecules by gamma rays, no combined effect was observed, indicating that the contribution to DNA damage caused by products of radiolysis of RAPTA C or CDDP is negligible in comparison to the damage caused by products of radiolysis of water. After binding to DNA, CDDP adducts with DNA strongly enhanced the damage in a good agreement with the results of other studies. RAPTA C adducts acted radio-protective at low doses of OH radical scavenger - tris(hydroxymethyl)aminomethane (tris) and showed no combined effects at higher tris levels. Radioprotectivity of RAPTA C is therefore primarily caused by enhanced resistance of RAPTA C modified DNA against the damage induced by radicals.

The same experiments have been performed also using 30 MeV proton beam at the U120M cyclotron. The goal of the study is to understand the effect of radiation quality on primary radiation damage to DNA and possible changes of radiomodifying properties of studied organometallic compounds. The results are currently under evaluation. Future studies using other types of organometallics, namely titanocenes, are planned in close future.

SINE2020 feasibility study - Upgrading UHSS by improving cast microstructure

Neutron Physics Laboratory - Neutron diffraction

Pavel Strunz

Proposal ID

258

1.1. Experimental set-up and data analysis

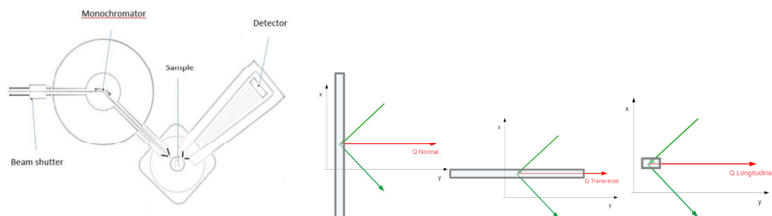
The neutron diffraction measurements were carried out on the dedicated strain diffractometer SPN-100 installed at the research reactor LVR-15 in Řež. The instrument is equipped with a focusing Si(111) monochromator and a 2D position sensitive detector.

The measurements were done at a fixed position of the 2D detector with the centre of the detector positioned at an angle of $2\theta = 65^\circ$ and an angular range of 12 degrees, the constant neutron wavelength was 0.235 nm, providing a good resolution after diffraction on the α -Fe(110) and / or γ -Fe(111) lattices planes.

A sample gauge volume of $3\text{mm} \times 3\text{mm} \times 3\text{mm}$ was defined using fixed cadmium slits in the incident and diffracted neutron beam.

Instrument setup:

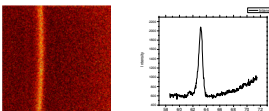
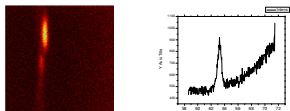
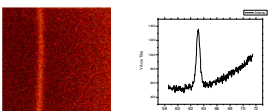
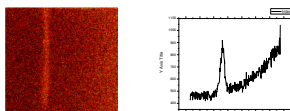
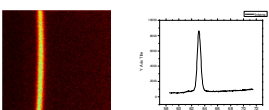
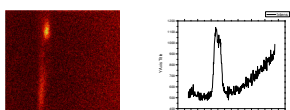
Sample orientations for measurements:



1.1. Data analysis and discussion

Measurements have been performed in the middle of the samples thickness, on a line passing across the marked dendrites line.

Examples of obtained diffraction cones and resulting diffractograms.

Forged sample	As-cast sample
<p>Normal</p> 	<p>Normal</p> 
<p>Transverse</p> 	<p>Transverse</p> 
<p>Longitudinal</p> 	<p>Longitudinal</p> 

Forged sample:

Data are of good quality and could be analysed.

Since no reference sample for strain free ("d0") value were available (see below comments on the as-cast sample), only relative values based on peak position change can be calculated. With this material, no significant change in peak position, and hence residual strain is observed across the sample.

As-cast sample:

Examples of obtained diffraction cones and resulting diffractograms.

With the as-cast sample, uneven diffraction cone intensity were observed on the 2D positional sensitive detector, complicating the calculation of diffraction pattern (intensity as a function of 2θ angle) and reliable fitting to the Bragg reflections to extract peak positions.

2. Conclusion & Prospective actions

In conclusion, for the forged sample, no variation in the bragg peak position, and hence residual strain is observed across the sample. For the as-cast sample, unfortunately, no reliable residual strain / stress values could be extracted from the measured data. This is likely due to the large grains and segregation present in the specimens. Alternative analysis methods should be explored.

Study of energy loss and energy straggling of heavy ions in polymers, silicon nitride and SOI.

Laboratory of Tandetron

Romana Mikšová

Proposal ID

199

Report regarding proposal “Study of energy loss and energy straggling of heavy ions in polymers, silicon nitride and SOI.”

R. Mikšová, V. Hnatowicz, A. Macková, P. Malinský, Nucl. Physics Inst., Rez, Czech Republic
P. Slepíčka, Inst. Chem. Tech., Prague, Czech Republic

Our results of C^{n+} and O^{n+} ions the stopping powers in PP and Si_3N_4 show systematic differences between the experimental and semi-empirical predicted data. More significant discrepancies between the experimental and predicted stopping power of heavier O ions in SRIM and MSTAR code can be a result of a more significant radiation damage of the irradiated PP accompanied by the escape of volatile fragments. In the case of experimental straggling better comparison provides Yang's theory for both ion species than the Bohr and Bethe–Livingston theories. The Yang formula systematically underestimates the measured values with an average deviation of about 3–24% for silicon nitride and 4–25% for PP.

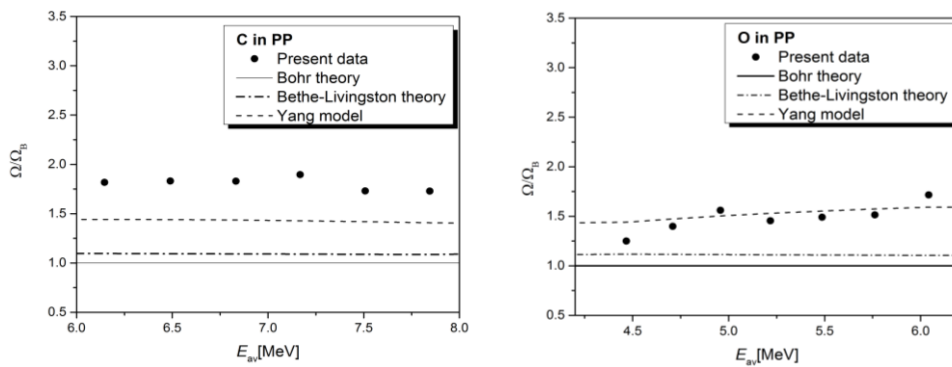


Figure 1. Experimental reduced (Ω/Ω_B) for (a) C and (b) O in PP (points) versus reference energy, compared to straggling predicted values by Bohr, Bethe–Livingston theories and Yang's empirical formula (lines).

The channelling stopping power decreases with increasing energy, which is a general trend for both ion species. At higher ion energy, the differences between the channelling and random stopping powers of helium ions are quite similar to those obtained for lithium ions, so that for both ion species at higher energy the channelling stopping powers are close to 50 % of the random stopping powers (see Figure 2). This confirms the basic theory that the best channelling ions have a stopping power in the order of one-half of the stopping power in the corresponding random direction.

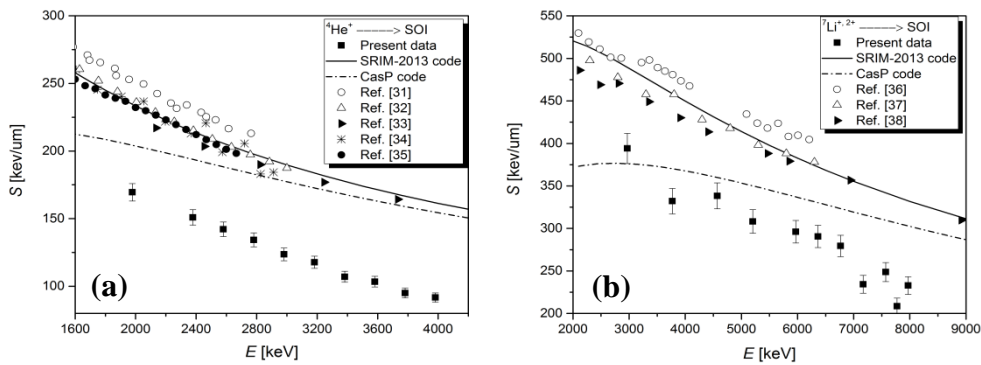


Figure 2. The experimental stopping powers for helium (a) and lithium (b) ions along the $\langle 100 \rangle$ direction in Si (points) and the calculated random stopping powers using SRIM-2013 (solid line), the UCA model from the CasP code (dash-dot line) and the experimental random stopping powers from literature for comparison (points).

The results have been accepted for publication in NIMB Proceedings

Quantification of elements in nanocarbons by Neutron Activation Analysis (NAA).

Neutron Physics Laboratory - Nuclear analytical methods with neutrons

Filipa Fernandes

Proposal ID

328

3050 Spruce Street, Saint Louis, MO 63103, USA

Website: www.sigmaaldrich.comEmail USA: techserv@sial.comOutside USA: eurtechserv@sial.com

Certificate of Analysis

Product Name:

Carbon nanotube, single-walled - (7,6) chirality, carbon >90 %, ≥77% (carbon as SWNT), 0.7-1.1 nm diameter

Product Number: 704121
Batch Number: MKBT4053V
Brand: ALDRICH
CAS Number: 308068-56-6
Quality Release Date: 05 DEC 2014



Test	Specification	Result
Purity	≥ 77.0 %	91.5 %
T1% (Estimate of SWNT Content by Weight (TGA))		
Residual Mass (TGA)	≤ 10.0 %	3.4 %
Carbon (TGA)	≥ 90.0 %	95.5 %
Chirality Distribution		1.25
P2B (QC Parameter for control of chirality distribution at 1130-1140 nm (UV-vis-NIR Spectroscopy))		
Quality Factor	≥ 0.940	0.960
Q (D:G Ratio) Raman Spectroscopy		
Note	Complete	Conforms
Please see Technical Bulletin AL-252 for explanation of quality parameters. Spectra available upon request.		

Ali Ataei, Manager
Quality Control
Milwaukee, WI US

Sigma-Aldrich warrants, that at the time of the quality release or subsequent retest date this product conformed to the information contained in this publication. The current Specification sheet may be available at Sigma-Aldrich.com. For further inquiries, please contact Technical Service. Purchaser must determine the suitability of the product for its particular use. See reverse side of invoice or packing slip for additional terms and conditions of sale.